

**CFD MODELLING FOR THE STUDY OF STRUCTURAL STABILITY OF DAMS
AND SPILLWAYS SUBJECT TO OVERTOPPING**

*MODELAGEM EM CFD PARA O ESTUDO DA ESTABILIDADE ESTRUTURAL DE
BARRAGENS E VERTEDOUROS SUJEITOS AO GALGAMENTO*

MARIO RAUL FREITAS

**MASTER'S DISSERTATION IN STRUCTURAL ENGINEERING AND
CONSTRUCTION**

DISSERTAÇÃO DE MESTRADO EM ESTRUTURAS E CONSTRUÇÃO CIVIL

FACULDADE DE TECNOLOGIA

UNIVERSIDADE DE BRASÍLIA

**UNIVERSIDADE DE BRASÍLIA
FACULDADE DE TECNOLOGIA
DEPARTAMENTO DE ENGENHARIA CIVIL E AMBIENTAL**

**MODELAGEM EM CFD PARA O ESTUDO DA ESTABILIDADE
ESTRUTURAL DE BARRAGENS E VERTEDOUROS
SUJEITOS AO GALGAMENTO**

MARIO RAUL FREITAS

**ORIENTADOR: LINEU JOSÉ PEDROSO
CO-ORIENTADOR: PIERRE LÉGER**

**DISSERTAÇÃO DE MESTRADO EM ESTRUTURAS E CONSTRUÇÃO
CIVIL**

**PUBLICAÇÃO: E.DM – 10A/19
BRASÍLIA / DF: JULHO/2019**

**UNIVERSIDADE DE BRASÍLIA
FACULDADE DE TECNOLOGIA
DEPARTAMENTO DE ENGENHARIA CIVIL E AMBIENTAL**

**MODELAGEM EM CFD PARA O ESTUDO DA ESTABILIDADE
ESTRUTURAL DE BARRAGENS E VERTEDOUROS
SUJEITOS AO GALGAMENTO**

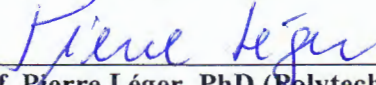
MARIO RAUL FREITAS

DISSERTAÇÃO DE MESTRADO SUBMETIDA AO DEPARTAMENTO DE ENGENHARIA CIVIL E AMBIENTAL DA FACULDADE DE TECNOLOGIA DA UNIVERSIDADE DE BRASÍLIA COMO PARTE DOS REQUISITOS NECESSÁRIOS PARA A OBTENÇÃO DO GRAU DE MESTRE EM ESTRUTURAS E CONSTRUÇÃO CIVIL.

APROVADA POR:



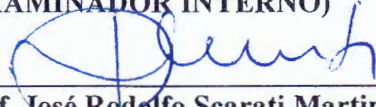
Prof. Lineu José Pedroso, Dr. Ing. (ENC/UnB)
(ORIENTADOR)



Prof. Pierre Léger, PhD (Polytechnique Montreal/Canadá)
(CO-ORIENTADOR)



Prof. Francisco Evangelista Júnior, PhD (ENC/UnB)
(EXAMINADOR INTERNO)



Prof. José Rodolfo Scarati Martins, PhD (Escola Politécnica/USP)
(EXAMINADOR EXTERNO)

DATA: BRASÍLIA/DF, JULHO DE 2019.

FICHA CATALOGRÁFICA

FF866c Freitas, Mario Raul
CFD Modelling for the Study of Structural Stability of
Dams and Spillways Subject to Overtopping / Mario Raul
Freitas; orientador Lineu José Pedroso; co-orientador
Pierre Léger. -- Brasília, 2019.
134 p.

Dissertação (Mestrado - Mestrado em Estruturas e
Construção Civil) -- Universidade de Brasília, 2019.

1. CFD. 2. Overtopping. 3. Dams. 4. Spillways. 5.
Stability. I. Pedroso, Lineu José, orient. II. Léger,
Pierre, co-orient. III. Título.

REFERÊNCIA BIBLIOGRÁFICA

FREITAS, M.R. (2019). CFD Modelling for the Study of Structural Stability of Dams and Spillways Subject to Overtopping. Dissertação de Mestrado em Estruturas e Construção Civil, Publicação E.DM – 10A/19, Departamento de Engenharia Civil e Ambiental, Universidade de Brasília, Brasília, DF, 134 p.

CESSÃO DE DIREITOS

AUTOR: Mario Raul Freitas

TÍTULO: CFD Modelling for the Study of Structural Stability of Dams and Spillways Subject to Overtopping

GRAU: Mestre

Ano: 2019

É concedida à Universidade de Brasília a permissão para reproduzir cópias desta dissertação de mestrado e para emprestar ou vender tais cópias somente para propósitos acadêmicos e científicos. O autor reserva outros direitos de publicação e nenhuma parte desta dissertação de mestrado pode ser reproduzida sem a autorização por escrito do autor.

Mario Raul Freitas
Rua das Paineiras Lote 05 Apt. 604
71929-180 – Águas Claras/DF - Brasil

ACKNOWLEDGMENTS

First, I would like to thank professor Pierre Léger from Polytechnique Montreal for giving me the opportunity to work with him in this research. I am immensely grateful for all the support professor Léger gave me from the moment I contacted him asking for a chance to do a research internship with him at Polytechnique Montreal until the last day I was there and even after I returned. This research would not have been possible without all his support and dedication.

I also acknowledge my deepest gratitude for my academic advisor, professor Lineu Pedroso, who has supported me since my first semester as an undergraduate student at University of Brasilia and continued to support me as my advisor since 2016. I would also like to thank my family and friends who always believed in my ambitious hopes and dreams.

I would like to thank CAPES for financing the entirety of my master's program. I would also like to thank Global Affairs Canada and the NSERC (National Science and Engineering Research Council of Canada) for the financial support that made my research internship possible through the Emerging Leaders in Americas Program (ELAP).

ABSTRACT

CFD MODELLING FOR THE STUDY OF STRUCTURAL STABILITY OF DAMS AND SPILLWAYS SUBJECT TO OVERTOPPING

Author: Mario Raul Freitas

Advisor: Lineu José Pedroso

Co-Advisor: Pierre Léger

Postgraduate Program in Structural Engineering and Construction

Brasília, July 2019

A particularly challenging aspect in gravity dam stability assessment is the estimation of the induced hydrodynamic water pressure when water with significant velocity is overtopping gravity dams and flowing in or over spillway components. The water flow conditions, including the related pressure fields and resultant forces, are difficult to quantify accurately. Computational fluid dynamics (CFD) is an attractive alternative to physical models to quantify the hydrodynamic forces acting on overtopped gravity structures and spillways to assess their structural stability. Herein, existing dam safety guidelines to estimate the weight of the overflowing water nappe on gravity dams with rectangular crests are first reviewed. Then, validation and verification models are run to ensure that the computational models are suitable for the case studies that are analyzed later. After that, CFD is used to develop an improvement to the simplified estimation of hydrodynamic pressure fields acting on the rectangular crests of submerged gravity dams. The CFD pressures are used as input data to classical structural stability analyses based on the gravity method to more adequately quantify the dam sliding stability during overtopping. Applications are then presented on an existing 7.6 m high gravity dam comparing existing dam safety guidelines with proposed improvements based on CFD. A back analysis is also performed on the stability of an existing gated spillway with a bridge that was overtopped during the 1996 Saguenay flood in Québec. The complex flow conditions across the spillway are investigated, including the incidence of accumulated floating debris producing additional thrusts on the structure.

RESUMO EXPANDIDO

MODELAGEM EM CFD PARA O ESTUDO DA ESTABILIDADE ESTRUTURAL DE BARRAGENS E VERTEDOUROS SUJEITOS AO GALGAMENTO

Autor: Mario Raul Freitas

Orientador: Lineu José Pedroso

Co-Orientador: Pierre Léger

Programa de Pós-Graduação em Estruturas e Construção Civil

Brasília, Julho de 2019

Um aspecto particularmente desafiador no cálculo de estabilidade de barragens de gravidade e vertedouros é a estimativa das pressões hidrodinâmicas quando água com uma velocidade significativa passa por cima da estrutura. As características do fluxo, incluindo os campos de pressões e forças resultantes são difíceis de quantificar com precisão. A Dinâmica dos Fluidos Computacional (em inglês, Computational Fluid Dynamics – CFD) é uma alternativa atrativa a modelos experimentais para quantificar as forças hidrodinâmicas atuando em barragens e vertedouros a fim de se calcular a estabilidade estrutural dessas estruturas.

Nessa dissertação, primeiramente são revisadas as normas técnicas para o cálculo estimado das forças hidrodinâmicas, incluindo a força vertical que lâmina de água transbordante exerce sobre a crista da estrutura. Em seguida, modelos de validação e verificação da técnica do CFD são simulados para garantir que o modelo computacional é adequado às análises que são feitas em seguida. Então, o CFD é utilizado para se obter uma melhora na técnica de estimativa dos campos de pressões hidrodinâmicas atuando sobre a crista retangular de barragens submersas. Os campos de pressão obtidos com CFD são usados como entrada para o cálculo de estabilidade feito com o método de gravidade para se obter uma melhor estimativa dos coeficientes de segurança e campos de tensão da estrutura. São apresentadas aplicações em uma barragem típica de 7,6 m de altura em que os coeficientes de segurança obtidos com CFD são comparados com aqueles obtidos com as estimativas de norma. Ao final, faz-se uma retroanálise de um vertedouro controlado por comporta que foi afetado pela enchente de Saguenay em 1996 em Québec, Canadá. As condições de fluxo

complexas são analisadas sob diferentes condições: com comportas abertas, comportas fechadas, comportas parcialmente fechadas e com a presença de detritos flutuantes.

As simulações em CFD são feitas com o programa ANSYS Fluent. A validação do programa e dos modelos computacionais é feita em várias etapas. Primeiramente, um modelo bidimensional de escoamento em torno de um quadrado é simulado pois esse é um caso bem estudado e que se pode encontrar muitos resultados na literatura. O escoamento em torno de um cilindro também poderia ser estudado, pois esse também é um caso bem estudado e que possui solução analítica. No entanto a geração da malha em torno de um círculo é significativamente mais complicada e seria uma fonte de erros numéricos. O estudo escoamento em torno do quadrado é dividido em três partes: (i) escoamento laminar permanente, (ii) escoamento laminar transiente, (iii) escoamento turbulento transiente. O escoamento laminar permanente é estudado com um número de Reynolds até 60. Nesse caso, verifica-se os primeiros passos básicos da modelagem, como a forma correta de modelar a geometria, gerar malha, entrar com as condições de contorno, propriedades do material e fazer o pós-processamento e estuda-se a influência do tamanho do domínio e refinamento de malha na resposta. Os coeficientes de arrasto encontrados para esse caso foram praticamente idênticos aos encontrados na literatura. No caso laminar transiente, com Reynolds entre 40 e 200, estuda-se a além do efeito do domínio e da geometria, o efeito do tamanho do passo de tempo na resposta. Novamente, os resultados obtidos ficaram em boa concordância com o que se encontrou na literatura. Por fim, no caso turbulento transiente, com Reynolds igual a 22000, introduz-se o modelo de turbulência adotado para toda a pesquisa, que foi o $k-\omega$ SST. Verificou-se novamente que os resultados condizem com os registrados na literatura e foi possível obter a formação do corredor de vórtices alternados como esperado.

A segunda etapa de validação foi a modelagem do escoamento vertical em queda livre de um filete de água, como a água que sai de uma torneira. O objetivo desse estudo foi introduzir o modelo multifásico escolhido para esse projeto, que foi o modelo de Volume de Fluido, e estudar a influência do refinamento da malha no cálculo de localização da interface água-ar. Inicialmente, o problema foi modelado com uma malha grossa, uma média e uma bem refinada. Percebeu-se que com a malha grossa não foi possível obter o perfil de água esperado e que após a água viajar apenas uma pequena fração do domínio o erro no cálculo da posição da interface já era tão grande que,

essencialmente, a porção inferior do domínio não possuía água de acordo com a simulação. Já com a malha mais refinada, o perfil é bem calculado e o filete de água se forma como esperado. Em seguida, testou-se uma técnica de adaptação de malha em que, baseado no resultado de uma simulação concluída, identifica-se as células da malha que contém a interface e faz-se o refinamento dessas. Então, uma nova rodada de simulação é feita com a malha adaptada e repete-se esse processo iterativamente. Ao fazer essas simulações, descobriu-se que a região da malha que contém a interface é crítica para a determinação da posição da interface e que as demais regiões do domínio podem ser menos refinadas. Portanto, a técnica de adaptação de malha permite obter resultados mais acurados com menor esforço computacional.

A terceira etapa de validação foi a modelagem do fluxo de água passando sobre um vertedouro padrão do tipo WES. Esse tipo de vertedouro é adotado e descrito por diversas normas. Faz-se um estudo de convergência do domínio e de malha. Após obter a convergência do domínio e da malha, o perfil da lâmina vertente e o campo de pressões sobre o vertedouro é comparado com as normas. Nessa etapa, verificou-se o tamanho de malha adequado para os problemas estudados em seguida e a forma correta de modelar o escoamento livre bifásico.

A última etapa de validação foi a modelagem do escoamento de água sobre um vertedouro de soleira espessa. Nessa etapa, verificou-se duas possibilidades de aeração da lâmina vertente: (i) a introdução de uma condição de contorno na parede a jusante do vertedouro e (ii) o alargamento do domínio a jusante. Os resultados numéricos foram comparados com os resultados de um modelo experimental encontrado na literatura. Conclui-se que a estratégia de alargamento do domínio a jusante é mais precisa e versátil apesar de exigir a modelagem tridimensional, enquanto a outra estratégia pode ser aplicada em um modelo bidimensional. Portanto, para todos os estudos seguintes utiliza-se a estratégia de alargamento do domínio.

Com a validação concluída, realizou-se três estudos: (i) estudou-se a força vertical sobre uma crista retangular devido às forças hidrodinâmicas, (ii) estudou-se a estabilidade de uma barragem real de perfil típico, (iii) fez-se uma retroanálise de um vertedouro atingido por uma enchente. O estudo da força vertical sobre uma crista retangular foi feito em um modelo semelhante ao modelo estudado na última etapa de validação, porém com dimensões diferentes. A partir das simulações em CFD, obteve-se os campos de pressão sobre a crista da barragem. Esses campos de pressão

foram simplificados como sendo um campo trapezoidal que gere força e momentos equivalentes na estrutura. As normas de barragem sugerem que esse campo trapezoidal pode ser estimado como tendo uma pressão equivalente de uma lâmina de água com profundidade igual a lâmina vertente (a distância) a montante e metade desse valor a jusante. Com as simulações em CFD foi possível mostrar que usando dois terços da pressão equivalente de uma lâmina de água com profundidade igual a lâmina vertente a montante e um terço a jusante obtém-se uma estimativa muito mais precisa.

Em seguida, fez-se o estudo de estabilidade de uma barragem utilizando o campo de pressões obtidos com CFD, a estimativa da norma e a estimativa melhorada. Utilizando o método da gravidade, calculou-se os coeficientes de segurança e tensões na barragem a partir dessas cargas. Comparando-se as três metodologias para estimar os campos de pressão, mostrou-se que as estimativas de norma superestimam a carga vertical na crista. Essa carga atua como uma carga estabilizante e, portanto, superestimá-la é contra a segurança. Esse efeito se torna mais evidente em barragens de pequeno porte com uma grande lâmina de água passando sobre ela. Em contrapartida, a estimativa melhorada sugerida aqui estima a carga vertical com precisão e, conseqüentemente, leva a um fator de segurança menor e mais próximo à realidade.

Por fim, fez-se a retroanálise do vertedouro de Chute Garneau, em Québec, Canadá, que transbordou durante a enchente de Saguenay de 1996. Fez-se uma análise similar ao que foi feito para a barragem sob diferentes condições de fluxo: com comportas abertas, comportas fechadas, comportas parcialmente fechadas e com a presença de detrito flutuante. Ao fazer o cálculo de estabilidade, percebeu-se que sob as condições normais de projeto, a estrutura provavelmente teria falhado. No entanto, sabe-se que a estrutura sobreviveu ao evento. Portanto, fez-se uma análise paramétrica variando a resistência à tração e a coesão na interface concreto-solo. Com a análise paramétrica verificou-se que com pequenos incrementos de resistência à tração e coesão os coeficientes de segurança subiam a ponto de atender as exigências de norma para segurança. Esses valores de resistência à tração e coesão adicionados estavam consideravelmente abaixo da média averiguada experimentalmente em outras estruturas da região. Isso indica que é provável que essa resistência à tração e coesão estavam presentes e foram responsáveis por garantir que a estrutura resistisse à enchente.

TABLE OF CONTENTS

1. INTRODUCTION	1
1.1. Problem Statement	4
1.2. Objectives	6
1.3. Methodology	6
1.4. Scope and Limitations	10
1.5. Contributions	10
1.6. Organization	11
2. LITERATURE REVIEW	13
3. THEORETICAL FOUNDATION	18
3.1. Computational Fluid Dynamics	18
3.1.1. Basic Governing Equations	20
3.1.2. Multiphasic System Modeling	22
3.1.3. Turbulence Model	24
3.1.4. Solution Methodology	27
3.1.5. Numerical Methods	29
3.2. Expected Loads on Spillways and Gravity Dams	31
4. CFD PRELIMINARY RESULTS - VALIDATIONS AND VERIFICATION	36
4.1. Flow Around a Square Cylinder	36
4.1.1. Steady State Laminar Flow	39
4.1.2. Transient Laminar Flow	43
4.1.3. Transient Turbulent Flow	48
4.2. Water Tap Flow Model	49
4.3. Flow Over Ogee Spillway	57

4.4.	Flow Over Broad-Crested Weir	62
5.	OVERTOPPING OF RECTANGULAR CREST	67
5.1.	Rectangular Crest Analyzed	67
5.2.	CFD Comparison with Dam Safety Guidelines	68
6.	STABILITY OF OVERTOPPED GRAVITY DAMS	72
6.1.	Gravity Dam Analyzed	72
6.2.	Stability Analysis with Gravity Method	73
6.3.	Stability Criteria	76
6.4.	Hydrostatic and Hydrodynamic Pressures	78
6.5.	Safety Factors	81
7.	CASE STUDY: EXISTING GATED SPILLWAY	83
7.1.	Spillway Description	83
7.2.	CFD Structural Modeling and Simulation	84
7.3.	Parametric Analysis	86
7.4.	Floating Debris	90
8.	CONCLUSIONS AND RECOMMENDATIONS	92
	REFERENCES	95
	Appendix A - User Guide for Modeling Multiphasic Open Channel Flow on Fluent Using VOF Model	108
	Appendix B - Mesh Adaptation On Fluent	133
	Appendix C – Computer Specifications	134

LIST OF FIGURES

Figure 1 – Bell Falls overtopped (Quebec, Canada) (CBC, 2019)	4
Figure 2 – Chute Garneau spillway during the Saguenay flood (Nguyen, 2009).....	5
Figure 3 – Summary of CFD model boundary conditions, dimensions, mesh and flow properties	6
Figure 4 – Numerical simulations sequence	7
Figure 5 – Stability evaluation from hydrodynamic forces obtained with CFD methodology	9
Figure 6 – Fluid discretization with (a) fixed control volume, (b) moving control volume, (c) fixed infinitesimal volume, (d) moving infinitesimal volume (Wendt et al., 2009)	19
Figure 7 – Infinitesimally small, moving fluid element. Only the forces in the x direction are shown (Wendt et al., 2009)	21
Figure 8 – VOF interface location: (a) real interface and (b) linear interpolation.....	23
Figure 9 – Fluent solution workflow for pressure-based methods (ANSYS, 2018).....	28
Figure 10 – Expected loads on a gravity dam: (a) estimated loads provided by guidelines and (b) hydrodynamic loads obtained with CFD	32
Figure 11 – Uplift pressure distribution (Novak et al., 2007 - adapted).....	33
Figure 12 – Failure mechanisms of an overtopped dam (Léger, 2019).....	35
Figure 13 – Geometry model for flow over a square cylinder.....	37
Figure 14 – Flow over a square cylinder mesh: (a) Biasing detail and (b) complete mesh.....	38
Figure 15 – Drag coefficient (Cd) and lift coefficient (Cl) in a transient simulation	39
Figure 16 – Domain convergence for steady-state laminar flow over a square cylinder ($Re = 40$): (a) upstream length $L1$ (b) downstream length $L2$ and (c) domain height HT	40
Figure 17 – Mesh convergence for steady-state laminar flow over a square cylinder ($Re = 40$)	41
Figure 18 – Steady-state laminar flow over a square cylinder validation.....	42
Figure 19 – Domain convergence for transient laminar flow over a square cylinder ($Re = 200$): (a) upstream length $L1$ (b) downstream length $L2$ and (c) domain height HT	44
Figure 20 – Mesh convergence for transient laminar flow over a square cylinder ($Re = 200$) ..	45

Figure 21 – Time step convergence for transient laminar flow over a square cylinder ($Re = 200$)	47
Figure 22 – Transient laminar flow over square cylinder verification	48
Figure 23 – Transient turbulent flow over square cylinder streamlines	49
Figure 24 – Free fall water stream control volume.....	50
Figure 25 – Free fall water stream profile with three meshes (a) M0.25, (b) M 0.10, (c) M0.05	53
Figure 26 – Mesh adaptation - First iteration (a) volume fraction, (b) adapted cells, (c) resulting mesh. Second iteration (d) volume fraction, (e) adapted cells, (f) resulting mesh	54
Figure 27 – Mass residual obtained using different meshes	55
Figure 28 – Free fall water stream profile comparison between analytical and numerical solutions	56
Figure 29 – WES spillway geometry definition (Instituto da Água, 2001)	57
Figure 30 – Ogee spillway computational model	58
Figure 31 – Mesh convergence analysis for standard ogee spillway	59
Figure 32 – Domain convergence analysis for standard ogee spillway: (a) upstream length $L1$, (b) downstream length $L2$, (c) domain height HT	60
Figure 33 – Water nappe profile over ogee spillway with $H0 = 1.33Hd$	61
Figure 34 – Pressure field comparison between CFD and USACE (1970) for the flow over ogee spillway with $H0 = 0.50Hd$, $H0 = 1.00Hd$ and $H0 = 1.33Hd$	62
Figure 35 – Broad crested weir computer models: (a) 2D model with aeration outlet and (b) 3D model with domain broadening	63
Figure 36 – Dimensionless water profile over a broad-crested weir	64
Figure 37 – Dimensionless pressure field over a broad-crested weir	65
Figure 38 – Numerical streamlines compared to experimental boundary separation curve.....	65
Figure 39 – Numerical model used for evaluation of vertical forces on a rectangular crest	68
Figure 40 – Simplified pressure field on crest subject to overtopping	69
Figure 41 – Comparison between pressure field using CFD and simplified method with $\alpha=1.0$ and $\beta=0.5$, and with $\alpha=2/3$ and $\beta=1/3$	71

Figure 42 – Pressure fields and forces obtained from (a) safety guideline and (b) CFD	72
Figure 43 – Shear and tensile strength of concrete-rock joint	78
Figure 44 – Chute Garneau blueprints: (a) plan view and (b) elevation dimensions	84
Figure 45 – Chute Garneau geometric model used on CFD simulations	85
Figure 46 – Chute Garneau spillway CFD model for $H_0 = 2.16\text{ m}$: water volume fraction at (a) spillway section and (b) pier section, velocity contours at (c) spillway section and (d) pier section, pressure contours at (e) spillway section and (f) pier section.....	86
Figure 47 –Chute Garneau spillway CFD model with Partially closed gates for $H = 7.42\text{ m}$	90
Figure 48 –Chute Garneau spillway CFD model with floating debris for $H_0 = 2\text{ m}$	91
Figure 49 – Empty fluent analysis system	108
Figure 50 – Main design tools of SpaceClaim.....	109
Figure 51 – Geometry sketch.....	109
Figure 52 – Extrude 3D model.....	109
Figure 53 – Partitioned 3D model.....	110
Figure 54 –Selection tools	110
Figure 55 – Wireframe tool.....	110
Figure 56 – Meshing tools	111
Figure 57 – Edge sizing with bias.....	112
Figure 58 – Edge sizing for all edges.....	112
Figure 59 – Face meshing settings.....	113
Figure 60 – MultiZone method settings.....	113
Figure 61 – Named selection creation	114
Figure 62 – All named selections.....	114
Figure 63 – Broad weir model mesh.....	114
Figure 64 – Fluent launcher initialization.....	115

Figure 65 –General settings	116
Figure 66 –Models menu	117
Figure 67 –Multiphase model	117
Figure 68 –Viscous model	118
Figure 69 –Adding water to materials	119
Figure 70 –Materials menu	119
Figure 71 –Phases Definition.....	120
Figure 72 –Phase Interaction	120
Figure 73 –Boundary conditions menu and operating conditions window	121
Figure 74 –Changing inlet to mass-flow.....	122
Figure 75 –Mass-Flow Inlet – Multiphase tab.....	122
Figure 76 –Mass-Flow Inlet – Momentum tab	122
Figure 77 –Mass-Flow Inlet – Defining the mass flow rates.....	123
Figure 78 –Atmosphere outlet – Multiphase tab.....	124
Figure 79 –Atmosphere outlet – Momentum tab.....	124
Figure 80 –Outlet – Multiphase tab	125
Figure 81 –Outlet – Momentum tab.....	125
Figure 82 –Solution Methods.....	126
Figure 83 –Initialization menu.....	126
Figure 84 –Phase fraction contour plot.....	127
Figure 85 –Region adaptation option.....	127
Figure 86 –Region adaptation window	128
Figure 87 –Patch window	128
Figure 88 –Water volume fraction after patching.....	129
Figure 89 –Run calculation menu	129

Figure 90 –Calculation activities	130
Figure 91 –Residual monitors window	131
Figure 92 –Setting flow report.....	132
Figure 93 –Flux report definition window.....	132
Figure 94 –Iso-Value adaptation window.....	133
Figure 95 –Manage adaptation Registers window	134

LIST OF TABLES

Table 1 – Constants from the k- ε model.....	26
Table 2 – Comparison of streamlines for steady laminar flow around a square cylinder for multiple Reynolds numbers.....	43
Table 3 – Transient turbulent flow over square cylinder results with $Re = 22000$	49
Table 4 - Meshes used for the water tap problem.....	51
Table 5 - Crest pressure coefficients obtained from CFD	70
Table 6 - Dam stability without tailwater	80
Table 7 - Dam stability with tailwater	81
Table 8 - Chute Garneau stability with opened gates	87
Table 9 - Chute Garneau stability with closed gates.....	88
Table 10 - Chute Garneau stability with partially closed gates	89

LIST OF SYMBOLS AND ABBREVIATIONS

Symbols

A – Area

A_c – Compressed area

A_h – Area of horizontal surface

B – Dam crest width

B_0 – Dam base width

c – Cohesion

C – Courant number

C_d – Drag coefficient

C_D – Discharge coefficient

C_l – Lift coefficient

$C_{l,max}$ – Maximum lift coefficient

$C_{l,rms}$ – Root mean square of the lift coefficient

C_{max} – Maximum Courant number

$C_{1\varepsilon}, C_{2\varepsilon}, C_{3\varepsilon}, C_\mu$ – k- ε model constants

D – Diameter

e – Moment excentricity

f'_c – Compressive strength

f_t – Tensile strength

\vec{F} – External body force

F_d – Drag force

$F_{d/s}$ – Downstream force

F_h – Horizontal force upstream

F_l – Lift force

F_v – Vertical force on the crest of a dam

\vec{g} – gravity acceleration

G_b – Generation of turbulence kinetic energy due to buoyancy

G_k – Generation of turbulence kinetic energy due to the mean velocity gradients

G_ω – Generation of turbulence specific dissipation rate

H – Total water height

H_{crest} – Crest height

H_d – Design water head

H_{dam} – Dam height

$H_{d/s}$ – Tailwater head

H_p – Pressure water head

H_T – Domain height

H_0 – Overtopping height

I – Unit tensor

J – Moment of inertia

k – Turbulence kinetic energy

L – Dam length

L_1, L_2 – Domain dimensions

m – Mass

\dot{m}_{aw} – Mass transfer from the air phase to the water phase

\dot{m}_{wa} – Mass transfer from the water phase to the air phase

M – Bending moment

M_{+ve} – Stabilizing Moments

M_{-ve} – Destabilizing Moments

n – Ratio between vortex shedding period and time step size

p – Pressure

$p_{u,d/s}$ – Uplift pressure downstream

$p_{u,u/s}$ – Uplift pressure upstream

p_w – External hydrostatic pressure

Q – Flow

Re – Reynolds number

R_x – Resulting horizontal force

R_y – Resulting vertical force

S – Cross section area

S_k – Turbulence kinetic energy source

S_m – Mass source

S_t – Strouhal number

S_{α_w} – Water fraction source

S_ε – Turbulence dissipation rate source

S_ω – Turbulence specific dissipation rate source

t – Time

T – Vortex shedding period

U – Uplift force

U_f – Volume flux through the face of the cell

v_i – Velocity component in one of the three cartesian directions

\bar{v}_i – Average velocity component in one of the three cartesian directions

v'_i – Fluctuating velocity component in one of the three cartesian directions

\vec{v} – Velocity vector

\vec{v}_w – Water phase velocity vector

V – Volume of the cell or control volume

V_c – Concrete dam volume

W – Dam self-weight

x – Horizontal direction coordinate

x_i – One of the cartesian directions

y – Vertical direction coordinate

y' – Distance from point of analysis to the neutral axis

Y_k – Dissipation of k

Y_M – Contribution of the fluctuating dilatation in compressible turbulence to the overall dissipation rate

Y_ω – Dissipation of ω

z – Water depth

$z_{d/s}$ – Water depth downstream

$z_{u/s}$ – Water depth upstream

α, β – Vertical force estimation coefficients

α_a – Air volume fraction

α_w – Water volume fraction

α^* – Correction coefficient for low-Reynolds number in the k - ω model

γ_c – Concrete specific weight

γ_w – Water specific weight

Γ_k – Effective diffusivity of k

Γ_ω – Effective diffusivity of ω

δ_{ij} – Kronecker delta

Δt – Time step size

Δx – Cell length in the direction of the flow

Δy – Vertical distance between two points

ε – Turbulence dissipation rate

ε_m – Mass residual

η, ξ – Cell side dimensions

μ – Dynamic viscosity

μ_t – Turbulent viscosity

ρ – Specific mass

$-\rho \overline{v'_i v'_j}$ – Reynolds stresses

ρ_w – Water specific mass

σ_k – Prandtl number for turbulence kinetic energy

σ_n – Threshold compressive stress

σ_t – Tensile stress

σ_y – Normal stress on a vertical plane

σ_{yd} – Downstream face normal stress on a vertical plane

σ_{yu} – Upstream face normal stress on a vertical plane

σ_z – Normal stress on a horizontal plane

σ_{zd} – Downstream face normal stress on a horizontal plane

σ_{zu} – Upstream face normal stress on a horizontal plane

σ_ε – Prandtl number for turbulence dissipation rate

σ_1 – Maximum normal stress

σ_3 – Minimum normal stress
 ΣH – Sum of horizontal forces
 ΣV – Sum of vertical forces
 $\Sigma \bar{V}$ – Sum of vertical forces (except uplift)
 τ_d – Downstream face shear stress
 τ_u – Upstream face shear stress
 τ_{max} – Maximum shear stress
 $\bar{\tau}$ – Stress tensor
 ϕ – Friction angle
 ϕ_d – Downstream face slope
 ϕ_u – Upstream face slope
 φ – A generic fluid mix property such as specific mass and viscosity
 φ_a – A generic air property such as specific mass and viscosity
 φ_w – A generic water property such as specific mass and viscosity
 ω – Turbulent specific dissipation rate

Abbreviations

ANCOLD – Australian National Committee on Large Dams
CDA – Canadian Dam Association
CFD – Computational Fluid Dynamics
CFL – Courant–Friedrichs–Lewy
CICSAM – Compressive Interface Capturing Scheme for Arbitrary Meshes
FEM – Finite Element Method
FERC – Federal Energy Regulatory Commission

GDFE – Grupo de Dinâmica e Fluido-Estrutura (Group of Dynamics and Fluid-Structure Interaction)

HRIC – High Resolution Interface Capturing

ICOLD – International Commission on Large Dams

MUSCL – Monotone Upstream-Centered Schemes for Conservation Laws

OSF – Overturning Safety Factor

PISO – Pressure-Implicit with Splitting of Operators

PRESTO! – PREssure STaggering Option

QUICK – Quadratic Upstream Interpolation for Convective Kinematics

RANS – Reynolds-Averaged Navier-Stokes

SIMPLE – Semi-Implicit Method for Pressure Linked Equations

SIMPLEC – Semi-Implicit Method for Pressure Linked Equations Consistent

SSF – Sliding Safety Factor

SST – Shear Stress Transport

USACE – United States Army Corps of Engineers

USBR – United States Bureau of Reclamation

USF – Uplift Safety Factor

VOF – Volume of Fluid

WES – Waterway Experimental Station

1. INTRODUCTION

The construction of dams for the purpose of storing water was one of the first big civil engineering activities performed by men. The Sadd-el-Kagara dam, in Egypt, was built around 2600 BC and is the oldest known dam of real significance. Every big civilization has used this kind of structure for one or more of the following uses: (i) normalize water flow, (ii) avoid floods, (iii) store water for periods of drought, (iv) satisfy irrigation demands, (v) generate electricity, among others. Even nowadays, the development level of a nation is associated with its capacity to manage its hydraulic resources. Dams construction continues to represent a significant investment in developing countries like Brazil, China, Turkey and India and to a lesser degree in developed countries like Canada and the United States (Novak et al., 2007).

Dams can be classified by its purpose or its type. Some dams are built for a single purpose, while others are used for many. The International Commission on Large Dams (ICOLD) presents data on 59,071 dams purpose and types. According to the data, among the single-purpose dams, 50% of them are used for irrigation, 20% for hydropower and 11% for water supply. Among the multipurpose dams, 24% are used for irrigation, 16% for hydropower and 17% for water supply (ICOLD, 2019). The list of dam functions also includes flood control, recreation, navigation, fish farming and others.

As for the dam types, 65% of them are earth dams, 13% are rockfill dams, 13% are gravity dams, and 4% are arch dams. Other types include buttress dams, multiple arch dams and barrages. The Rogun dam, in Tajikistan, is the highest earth dam with a height of 335 *m*, while the Grande Dixence dam, in Switzerland, is the highest gravity dam, with a height of 285 *m* (ICOLD, 2018).

All dams need one or more spillways to protect the dam from floods. The spillway should ensure a safe passage of flood water from the reservoir to the river downstream and prevent overtopping of the dam. Spillways can be gated or free. Gated spillways may be operated manually, remotely or automatically. In free spillways, when the water level surpasses the spillway crest level, the water naturally flows over or into the spillway.

The spillway should also ensure that the water does not promote the scouring of the soil downstream. Thus, it is very common to build energy dissipators in the spillway to deaccelerate the flow and prevent erosion downstream. Some of the most common energy dissipators are steps, built along the spillway chute, and the flip bucket, built at the base of the spillway.

The failure of a dam can cause immense destruction and huge losses in terms of human lives, environmental and economic damage. These facts were evidenced in two recent cases in Brazil. The first is the Fundão tailing dam failure in 2015, in Mariana, Minas Gerais, which caused the death of 19 people and the biggest environmental disaster in Brazil history. The second is the Brumadinho tailing dam failure in 2019, also in Minas Gerais, which caused the death of more than 200 people. Thus, it is essential to understand how these structures work, which loads are involved and how to evaluate the structure stability to ensure its safety.

ICOLD studies show that most tailing dams incidents are related to their spillways, either for having insufficient capacity or for being eroded during a flood. (ICOLD, 2001). If the spillway fails to transport the flood water downstream, overtopping is very likely to happen. ICOLD studies also show that overtopping was the main cause of 22% of all dam failures. In masonry dams, overtopping is responsible for 38% of the failures (Douglas et al., 1998). In concrete dams, overtopping is related to the failure of 20% of the dams ICOLD (1995). Even when overtopping itself is not the only cause of the failure it may contribute to it. Overtopping could lead to erosion of the downstream section and an increase in the shear force acting on the dam, both of which may contribute to failure. This happened in the Sella Zerbino dam, a concrete gravity dam which failed in 1935 after being overtopped. This dam had no spillway and the overtopping caused erosion of the foundation at the toe of the dam, which was pointed as one of the possible causes for the failure (Alvi, 2015; Petaccia et al., 2016). Faulty gate operation can also result in a detrimental dam and spillway overtopping (Lewin, 2001; Graham and Hildale, 2002; Allen, 2009; Hartford et al., 2016).

The first rational methods of analysis of masonry dams were developed around 1865 in France, the United Kingdom and the United States. Prior to that, the construction of dams was based mostly on empirical methods. Advances in soil mechanics around 1930 brought new theories for the

analysis of embankments. In recent years, new computational methods, such as the Finite Element Method (FEM) have provided powerful tools for much more precise analysis (Novak et al., 2007).

The Computational Fluid Dynamics (CFD) is one of these techniques developed in recent years. This technique is based on the solution of the Navier-Stokes equations. Since the 1960s, scientists and engineers have used these equations to solve fluid dynamics problems. However, the lack of computational power at the time limited the analysis to very simple cases. As computers become more powerful, CFD was further developed and the technique became more popular. Many advances in the technique were made from 1965 to 2005. The aerospace industry, with companies like NASA and Boeing, was the first to show interest for CFD, followed by the automotive industry, with companies like GM and Ford (Jameson, 2012). Since then, CFD has been used in many other applications, such as complex internal flows, heat exchange problems, and more recently, there have been some applications to hydraulic structures such as dams and spillways (Olsen and Kjellesvig, 1998; Gacek, 2007; Margeirsson, 2007; Kettner, 2010, Fill, 2011; Morais, 2015; Favre, 2018).

The estimation of the hydrodynamic loads on dams and spillways can be done via physical models, numerical analysis or using semi-empirical estimations provided by guidelines. Physical models are the most precise options, but it is very costly and time-consuming. On the other hand, the estimations provided by guidelines are very easy to apply, fast and do not cost anything, but are less precise and may not represent specific cases very well. Thus, guidelines tend to be on the conservative side, leading to a less cost-efficient design. Numerical methods, such as CFD, are an interesting alternative because they are much cheaper than physical models and more precise than the estimations provided by guidelines. However, the use of numerical models in this area is relatively recent and still requires more validation against physical models (Johnson and Savage, 2006).

1.1. Problem Statement

Dams and spillways are subject to many loadings and environmental hazards. Earthquakes, floods, floating debris, silt accumulation and ice are only some of the possible hazards that this type of structure might face. Each of these hazards can be studied as either a static or a dynamic load acting on the structure. Beyond that, the complexity of studying dams and spillways can be further increased if elements like cracking, scouring, fluid-structure interaction, soil-structure interaction and others are considered. Due to the high complexity of this kind of structure, some of these effects have to be studied separately.

The overtopping of dams is a common problem that happens all over the world. It is a consequence of floods in the region where the dam is located and it can be accompanied by the accumulation of floating debris upstream of the structure. In the spring of 2019, a big flood caused overtopping of the Bell Falls dam in Quebec, Canada. The flow rate achieved a level ten times higher than the normal flow. Although the structure survived the event, more than 60 people had to be evacuated from the region for safety reasons. Figure 1 shows pictures of the event published by the press at the time and a out of scale representation of the flow during the flood.

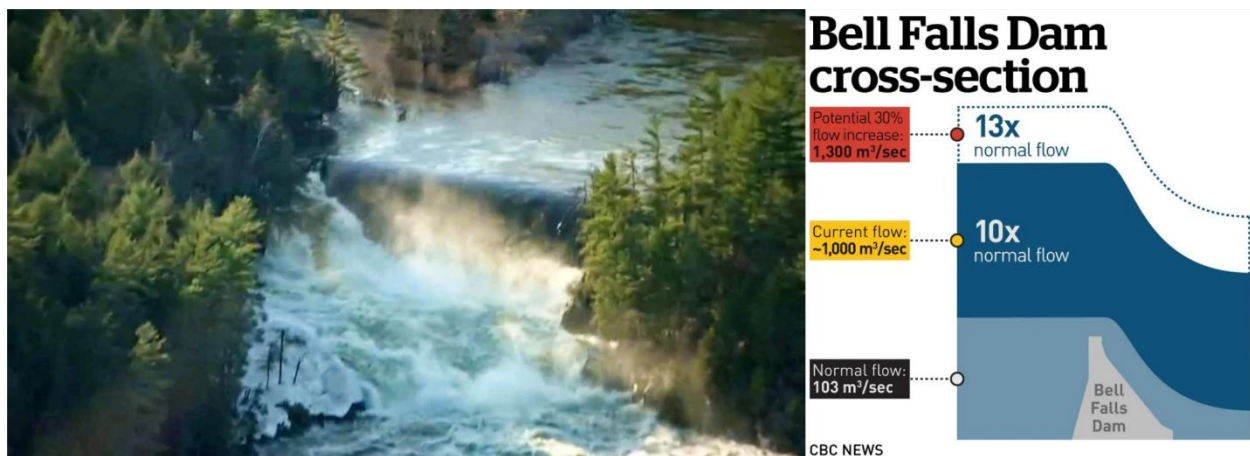


Figure 1 – Bell Falls overtopped (Quebec, Canada) (CBC, 2019)

Another case of flood-induced overtopping that happened in Quebec was the Saguenay flood. This flood happened in July of 1996, caused 10 deaths, 300 million dollars in damage and affected more than 16000 people. Among the structures affected by the flood was the Chute Garneau spillway, shown in Figure 2. During the flood, this spillway was overtopped by 2 metres and also survived the event. There was also a significant accumulation of floating debris on the gates lifting structure.



Figure 2 – Chute Garneau spillway during the Saguenay flood (Nguyen, 2009)

Floods like this represent a big increase in the hydrodynamic forces that the structure is subjected to. If big enough, this increase can cause the failure of the structure. However, precise calculation of the hydrodynamic forces is very complicated and the guidelines only offer simplified estimations. In this work, ANSYS Fluent, a CFD package, is used to evaluate the hydrodynamic pressure fields of overtopped dams and spillways with a higher level of accuracy. Then, a parametric analysis of the structural stability is done and the structure safety is evaluated. Figure 3 shows a summary of the computer model used to simulate the flow and obtain the pressure fields that are used to evaluate the structure safety, including a representation of the mesh, the water volume fraction α_w , the $k-\omega$ turbulence model, and the boundary conditions used, which are all explained later in the dissertation.

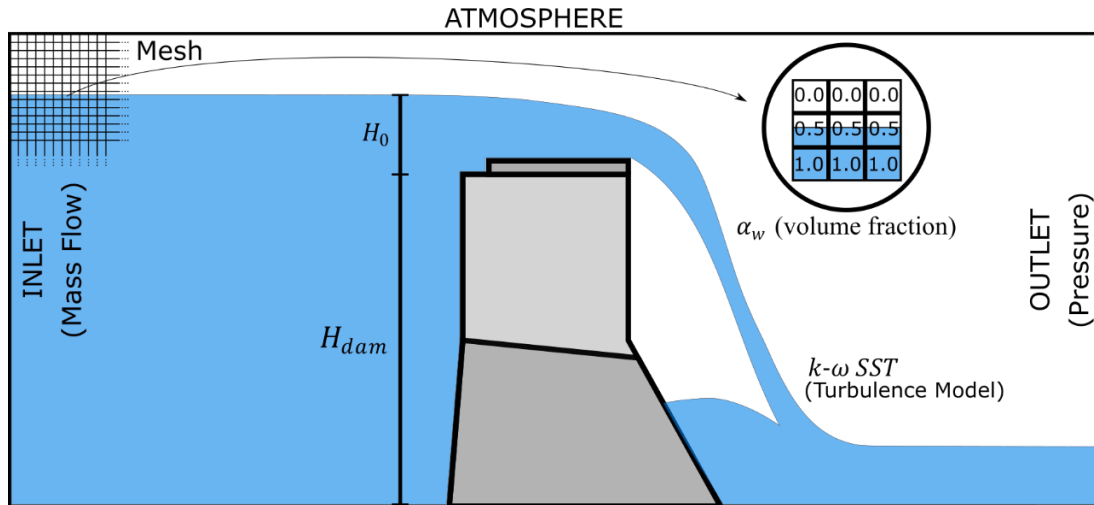


Figure 3 – Summary of CFD model boundary conditions, dimensions, mesh and flow properties

1.2. Objectives

The main objective of this work is to propose a methodology to evaluate the hydrodynamic forces on dams and spillways using CFD. Then, these forces are used to evaluate the structure stability, achieving a level of accuracy comparable to physical models. The specific objectives are detailed as follows:

- Identify the forces that influence the stability of dams and spillways;
- Validate classical flow problems with analytical solutions in Fluent;
- Validate spillway and dam flows in Fluent and compare to guidelines and physical models;
- Obtain hydrodynamic pressure fields;
- Obtain safety indicators for the case study problems under different loads;
- Identify the importance of cohesion and tensile strength to the structural stability.

1.3. Methodology

The overall methodology used in this dissertation primarily consists of doing a series of numerical simulations with CFD. These simulations represent a progressive approach that starts with basic

flows used for validation and verification and ends with case studies in which the flow response is used to evaluate a structure stability. Figure 4 shows a representation of all sets of simulations that are done in this work. The first two are the flow over a square cylinder and the flow from a water tap. These two cases are used mainly for learning and validation. The results and insights obtained from both of them are used in all of the following sets of simulations. The following sets are the flow over an ogee spillway, over a rectangular broad-crested weir, over a dam and, finally, the flow over a real spillway located in Québec, Canada.

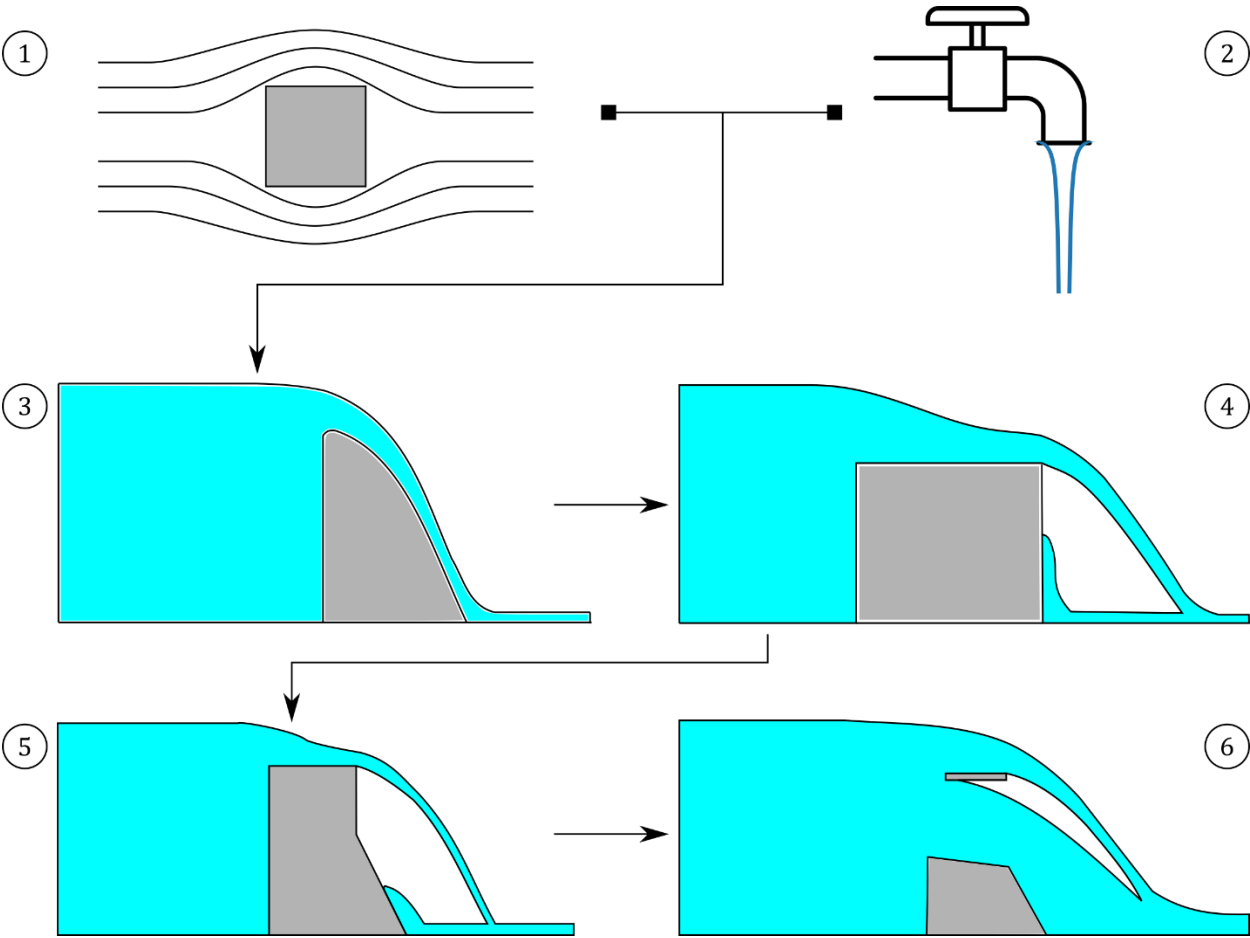


Figure 4 – Numerical simulations sequence

The first step in the development of this work concerning the CFD simulations is to validate classic flow problems to make sure that the software is being used correctly. Because this is the first work

in this department to use CFD applied to structural stability, all the steps to validate the model are clearly presented. Thus, this dissertation could be used as learning material for any future work involving the application of CFD to structural engineering.

The flow of water over a square cylinder, modelled in two dimensions, is the first validation case. First, the flow is modelled as a steady state problem with low Reynolds number. Then, the analysis is changed to transient still keeping the Reynolds number low to ensure laminar flow. Next, the turbulence model is implemented and the Reynolds number is increased significantly. The results in every step are compared to experimental results found in the literature. These steps are used to understand and learn how to model basic flows, how to enter the boundary conditions and to validate the turbulence model. This model can be used to simulate the flow of water around an off-shore platform column, a dam pier or even the flow of air around a tall building.

The flow of water from a tap, also modelled in two dimensions, is the second validation case. This is used to learn how to model a multiphasic flow. The Volume of Fluid (VOF) multiphasic model is used. The results are compared to the analytical solution. This case is important to validate the meshing technique used to properly compute the interface between the phases (water and air).

After validating the previous cases and learning how to implement the turbulence and the multiphasic flow models, the flow over an ogee spillway is studied. The standard ogee spillway is defined by USACE (1970), which provides the spillway geometry, the expected flow profile and the pressure fields for different overtopping heights. This validation case provides better insight as for what mesh size should be used in this work.

Next, the flow over a rectangular broad crested weir is modelled. This model is analogous to the case of overtopping over a dam crest, which is studied afterwards. Different aeration strategies are studied to ensure that the water nappe downstream separates from the structure and proper aeration is achieved. The results obtained with CFD are compared to experimental studies found in the literature.

After all these validation and verification cases are done, then some case studies can be investigated. The main motivation of these case studies is to compare how the real hydrodynamic forces differ from the simplified forces provided by guidelines and how this difference affects the

structure stability. In these case studies, the CFD simulations provide the hydrodynamic forces acting on the structures. The hydrodynamic forces are entered into CADAM3D (Leclerc and Léger, 2017), a software developed at Polytechnique Montreal which is used for the stability calculations. There is also a 2D version of this software called CADAM (Leclerc et al., 2001, 2003) which is used on the 2D analyses. Figure 5 schematically shows the methodology used for the stability calculations.

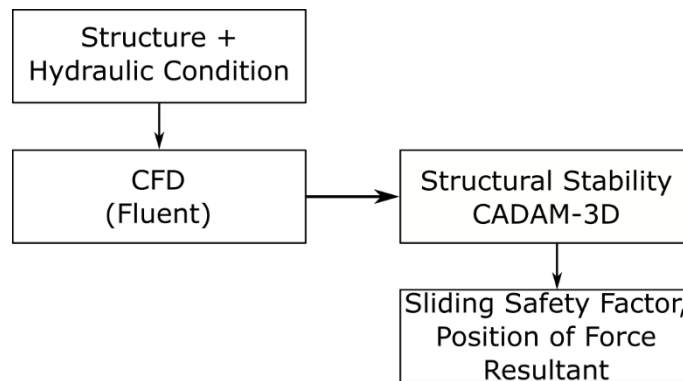


Figure 5 – Stability evaluation from hydrodynamic forces obtained with CFD methodology

First, a typical dam with varying crest width is modelled. The forces on the crest of the dam are computed from CFD and compared to guideline recommendations. Then, the stability of the dam is evaluated for different overtopping heights with and without tailwater. Finally, a back analysis is performed to study the stability of the Chute Garneau spillway. This is a spillway in Québec, Canada, that was overtopped in 1996 by over 2 meters and survived the event. A parametric analysis of the material properties in the dam-foundation interface is done to understand the mechanisms that prevented the structure from failing.

1.4. Scope and Limitations

This work consists in the application of CFD in different types of dams and spillways. Its scope and limitations are as follows:

- The numerical results are compared to experimental data found in the literature, analytical methods and guideline recommendations;
- The author did not perform any experimental analysis himself;
- As of the time when this work was done, the computational cost for complex CFD models was still considered high for mainstream computers. Thus, the computational mesh had to be somewhat limited to allow for reasonable computational time;
- All structures studied are considered rigid;
- All structures are made of concrete;
- Concrete is considered homogenous, isotropic and elastic.

1.5. Contributions

This dissertation presents a number of contributions to the Department of Civil and Environmental Engineering of the University of Brasília and to the scientific community in general. The contributions are as follows:

- A clear methodology for validation and verification of the CFD models is presented herein. This methodology can be used in future works on the flow of wind around tall buildings and towers, the flow of water around off-shore structures or over dams and spillways, among other cases.
- The water tap model demonstrates that in multiphase flow, especially with free fall of fluid, the mesh refinement is most important around the interface between phases. Also, this model shows that mesh adaptation can be used to refine the mesh around the interface and achieve better results in computing the interface position accurately.

- Two strategies to obtain aeration of the overflowing water nappe are presented. One consists of adding a pressure outlet to provide a source of air to the lower nappe of the flow and the other consists in enlarging part of the domain so that air can come from the sides. It is shown that the second strategy works better and is easier to implement in complex cases.
- An improvement to an estimation of the vertical force on the crest of overtopped dams suggested by FERC is presented herein.
- A methodology to evaluate the stability of dams and spillways using the hydrodynamic forces obtained from CFD is presented herein.
- From the back analysis of an overtopped spillway, it is shown that the tensile strength and cohesion at the base of the structure, which are usually not considered in design, provide a significant contribution to stability.

1.6. Organization

This dissertation is divided into 7 chapters as follows:

- The first chapter presents the introduction to the dissertation theme. The background and motivation for the research are presented to show the reasons why the topic is important for the scientific community. Then, the objectives of this research and the methodology used are presented. The scope, limitations and the contributions made from this work are presented next.
- The second chapter consists of a brief review of the literature. Works on CFD, dam stability overtopping and floating debris accumulation are discussed. Both works that were developed nationally and internationally are presented, including some from this department.
- In the third chapter, all the theoretical foundation used in this work is presented including, the CFD governing equation, the multiphase and turbulence models used, the solution

methodology and the numerical methods. The loads that are expected in the case study structures are also presented.

- Chapter four contains a series of simulation results used for validation and verification. The goal of this section is to individually validate each model, numerical method and boundary condition that are later used in the case study problems.
- Chapter five presents an investigation of the vertical force on the crest of dams. The goal is to obtain an improved estimation for this force based on the CFD results and an estimation technique found in the literature.
- In chapter six, the stability of an overtopped typical dam with varying dimension is analyzed. The safety factors obtained using the forces from CFD are compared to the ones obtained using the guidelines recommendations and with the improved estimation presented in chapter five.
- In chapter seven, a case study featuring a real spillway that was overtopped during a flood is presented. A back analysis is performed to evaluate the structure stability under this extreme load. The structure is analyzed under different conditions and a parametric analysis is done to study the influence of the soil-structure interface properties on the stability.
- Chapter eight presents the conclusions from this work and recommendations for future works.

2. LITERATURE REVIEW

In recent years, the use of CFD (Computational Fluid Dynamics), which allows the numerical computation of fluid flow characteristics around structures, has become more common in various fields of engineering. Advances in CFD have made it an attractive alternative in terms of cost and time to physical models that were, until recently, the only tools available to study the hydrodynamic effects on overtopped structures. Burnham (2011) summarized past successes and new directions in modelling dam flows with CFD. The author focuses his analysis on FLOW-3D, a commercial software that is very well known for its capabilities of solving dam and river flows very well. Burnham states that the most common simulations on this type of problem are spillway flow analysis, nappe impingement analysis, pressure/shear distribution and tractive force analysis, tailrace and stilling basin analysis, and river reach and intake analysis. The spillway flow analyses include ogee, labyrinth, stepped, gated spillways among other types.

Spillways are essential for safety and to provide sufficient flow discharge capacity during floods. Water flows over many types of spillway sections have been widely modelled by CFD, such as ogee spillways (Olsen and Kjellesvig, 1998; Kanyabujinja, 2015), stepped spillways (Arantes, 2007; Kositgittiwong et al., 2013), trapezoidal broad-crested weirs (Haun et al., 2011), non-standard spillways (Kermani and Barani 2014). Numerical results have shown good agreement with experimental data. Among the different types of spillways investigated, stepped spillways have been the subject of many studies using CFD because of their capacity to dissipate energy flow by aeration. Studies performed by Vosoughifar et al. (2013), Kositgittiwong et al. (2013) and Sweeney (2014) have demonstrated the capability of CFD to model air entrainment in stepped spillways. The capability of CFD to model air entrainment and energy dissipation of falling jets in dissipation basins has also been studied by Castillo and Carrillo (2012, 2013) and Castillo et al. (2014). Moreover, CFD simulations have been performed to model water flow on specific spillways with complex geometries. Gacek (2007) used FLOW-3D to model the flow through the Keeyask Generating Station's diversion and spillway and compared the numerical results with a physical model. The diversion structure was gated and analyses were made for different gate openings. Margeirsson (2007) modelled a converging overfall spillway with a series of baffles at

the stilling basin used to dissipate energy. Ho and Riddette (2010) present CFD models for many different spillways in Australia with types ranging from ogee to morning glory and labyrinth spillways. Other complex geometry spillways are studied by Paxson et al. (2008), Kettner (2010), Willey et al. (2012), Patarroyo et al. (2015), Rad (2016) and Ebner et al. (2016). CFD has also been used to determine, with improved accuracy, the pressures and forces acting on the Wanapum spillway to perform structural stability calculations (Griffith et al. 2007). The authors concluded that the standard stability analysis approach may underestimate the sliding safety factor (SSF) by 40-50% in comparison to the stability results based on CFD water pressures.

Many commercial CFD software packages have been developed in the last decades such as FLOW-3D, Fluent, CFX, PHOENICS and OpenFOAM. Several authors have used these or in-house programs to study the flow over hydraulic structures and the resulting velocity and pressure fields. Aydin and Ozturk (2009) have used Fluent to model a spillway aerator. The air-entrainment rates they obtained with CFD were compared to empirical equations, a prototype model and a small scale physical model. Their CFD results were in agreement with the empirical equations and prototype models and were even better than the physical model due to the fact that the latter includes scale effects. Sabzi and Afrous (2015) have also used Fluent to study the possibility of cavitation in an ogee spillway.

Kermani and Barani (2014) used Flow-3D to model the spillway on the Shahid Abbaspour dam in Iran. The authors used the renormalization group turbulence model (RNG $k-\epsilon$) and a modified version of the volume of fluid model (VOF) called FAVOR, which is available in FLOW-3D. The results were compared with an experimental model of the spillway. The pressure and velocity values computed from CFD differed by less than 6% and 8%, respectively, compared to the physical model, showing that the software can yield very accurate results. Gessler (2005) has also used FLOW-3D to model a much more complex spillway with a catch chute on an arch dam and also found results that are in accordance with a physical model. Kim and Park (2005) studied the influence of scale and roughness effects on an ogee spillway and they concluded that these parameters do not significantly affect the flow profile and the vertical pressures on the spillway. Other authors who used this software to study spillways include Ho et al. (2001), Savage and Johnson (2001), Johnson and Savage (2006), and Kumcu (2017).

The 1996 Saguenay flood, shown in Figure 2, was studied by many specialists in different areas. There were meteorological studies (Milbrandt and Yau, 2001; Nagarajan et al., 2006), studies about the application of remote sensing to flood monitoring (Fung et al., 1998), hydraulic and geological studies (Lapointe et al., 1998; Brooks and Lawrence, 2000; Capart et al., 2007), among many others. At Polytechnique Montreal, a series of studies on the Chute Garneau spillway, which was also affected by the Saguenay flood, was developed. Palavicini (1998) studied the overtopping of the Chute Garneau spillway with simplified analytical and numerical methods. Favre (2018), among other things, studied the same spillway with CFD using OpenFOAM. This dissertation is a continuation of these studies where ANSYS Fluent is used to improve on the CFD results obtained by Favre and to obtain new results that were not explored by either author.

During the Saguenay flood, there was a significant accumulation of floating debris in front of the spillways. Floating debris is a major problem during floods in several parts of the world. They produce additional thrusts on structures and clog spillway openings, thus reducing the discharge capacity while increasing the upstream water level (Abela 2018, SCD 2017, Godtland and Tesaker 1994). The effect of the floating debris on the Chute Garneau spillway was studied by Léger et al. (2000).

CFD has been used in many works for different purposes in Brazil. Morais (2015) used FLOW-3D to model an ogee spillway with a roller-bucket. He used the $k-\varepsilon$ turbulence model and compared the numerical results with experimental results, achieving good agreement between the two. Fill (2011) also used FLOW-3D to model the flow of water over the São Salvador hydroelectric powerplant spillway. Dias (2011) analyzed the flow over a side weir using three different turbulence models, $k-\varepsilon$, $k-\varepsilon$ (RNG) and SST $k-\omega$. Souza (2016), Arakaki Jr. (2016) and Lopes (2019) studied the flow around a cylinder under different aspects. Souza studied the von Kármán vortex street formation, Arakaki Jr. studied how the drag and lift coefficients change depending on the boundary conditions and the Strouhal number, and Lopes studied the flow around a 3D cylinder with low aspect ratio. Carneiro (2007) studied the flow induced vibration on offshore structures. Hallak (2002) and Costa (2018) used CFD to study the vibration of bridges subject to wind.

The University of Brasília's Group of Dynamics and Fluid-Structure Interaction (Grupo de Dinâmica e Fluido-Estrutura - GDFE) has previously developed some works on CFD. Ferreira (2012) has studied the effects of the water flow on an off-shore platform using CFX. He successfully modelled the water flow, obtained the pressure field along the structure and modelled the dynamic response of the structure using the ANSYS structural module. Santos (2017) also used CFX to model the effect of wind on a tall building, which was modelled as a circular cylinder. Silva (2018) used a similar circular cylinder model on CFX to study the flow of wind on a wind turbine tower. Pedroso et al. (2000) analyze the use of CFD in concrete dam engineering and Pedroso (2017) explains the basic CFD equations used in ANSYS.

The group has also developed many works on dams, spillways and gates. Oliveira (2002) has studied in depth the stresses and the stability of dams based on the gravity method. He has also developed and validated a computer software to evaluate the stability and stress distribution of a dam. Pedroso (2002) also describes the fundamentals of the gravity method. Melo (2006) and Ribeiro (2006) studied the effects of an earthquake on the stress distribution of a dam. Melo's approach as numerical, comparing the Finite Element method to the gravity method. Ribeiro, on the other hand, made an analytical study. There are also some works on the fluid-structure interaction between the water and the dam or the gates among other topics (Silva and Pedroso, 2007; Melo, 2009; Melo et al., 2010; Ribeiro 2010; Melo et al., 2013; Silveira, 2018; Mendes, 2018).

On the course of the development of this project, a series of complementary reports have been produced. In Freitas and Pedroso (2018a), a basic tutorial of how to model a 2D flow, from the geometry definition to the post-processing is presented. In Freitas and Pedroso (2018b), a detailed validation study for the laminar steady state flow of water around a square cylinder showing all the modelling steps are presented. In Freitas and Pedroso (2018c), another validation study of flow around a square cylinder is presented, this time, for a transient case. Other important detailed guides are presented in the appendices of this dissertation. In Appendix A, a guide on how to model a multiphasic open channel flow including the turbulence model is presented. In Appendix B a guide on how to use mesh adaptation in Fluent is presented. Appendix C presents the specifications of the computer used in this work.

This dissertation presents one of the first applications of CFD on hydraulic structures such as dams and spillways with the goal to analyze the structure stability. Its main contribution is to show a clear methodology for the evaluation of the stability using the hydrodynamic forces obtained from CFD. Another contribution is to present an improvement to a simplified estimation of the vertical force on the crest of an overtopped dam, which was obtained from the CFD results.

3. THEORETICAL FOUNDATION

In this chapter, the governing equations, discretization techniques and numerical methods that are used in CFD and are necessary for this work are presented. The expected loads on a gravity dam similar to the ones that are analyzed later are also presented.

3.1. Computational Fluid Dynamics

Computational fluid dynamics (CFD) consists of a series of methods and techniques used to solve fluid flow problems numerically. It can be used not only to solve the mechanical aspects of the flow, such as flow trajectory, speed and pressure fields, but also to solve heat transfer and chemical reactions in the flow. Fluid flow problems are governed by Navier-Stokes (also known as momentum equations) and mass conservation equations. Like other computational techniques, CFD works by transforming a continuous problem into a discrete problem and thus transforming a series of differential equations into algebraic equations.

In CFD, the discretization is done using control volumes. A control volume is a finite region delimited by a control surface. It can be fixed in space and have the fluid move through it or it can move along with the fluid, in which case the particles inside the control volume are always the same. When control volumes are used for discretization, the fluid flow equations are obtained in integral form.

Alternatively, the fluid discretization can be done with infinitesimal volumes. Just like control volumes, infinitesimal volumes can be fixed in space or move along with the fluid. When using infinitesimal volumes, the fluid flow equations are obtained in differential form. In both cases, it is possible to manipulate the equations to transform the integral form into differential form and vice-versa. Figure 6 shows a visual representation of all four types of discretization: using control volumes (top) or infinitesimal volumes (bottom) and making the element fixed (left) or move with the fluid (right).

When the element is fixed in space, the integral or differential equations obtained are called the conservation form of the governing equations. When the element move with the fluid, the integral or differential equations obtained are called the non-conservation form of the governing equations. In an analytical approach to fluid flow problems, the form of the equations is generally irrelevant, but for CFD they actually matter. Thus, it is important to understand the difference between them. There is also a third discretization approach which considers the movement of atoms and molecules themselves (Wendt et al., 2009).

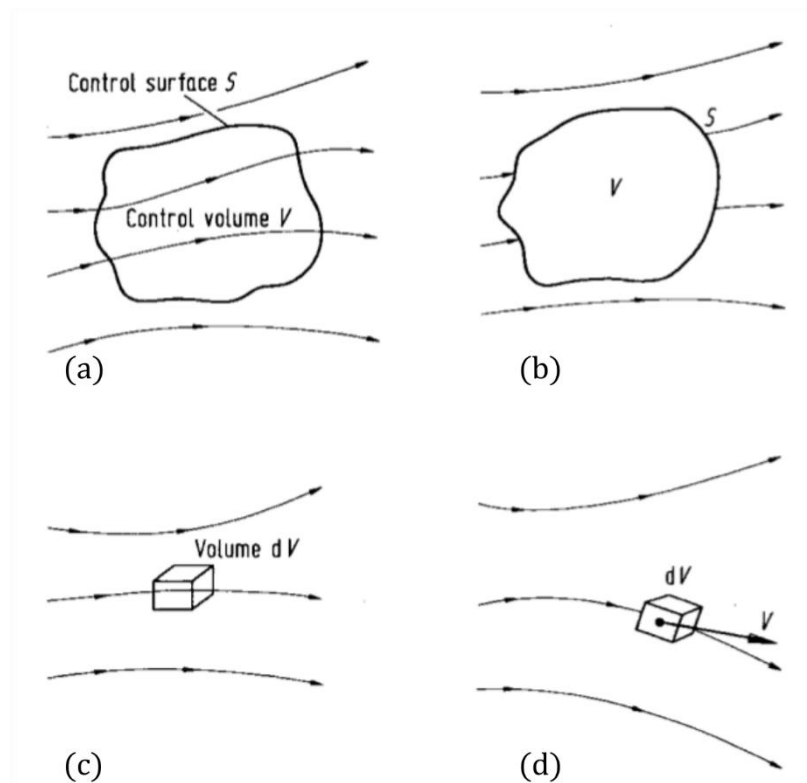


Figure 6 – Fluid discretization with (a) fixed control volume, (b) moving control volume, (c) fixed infinitesimal volume, (d) moving infinitesimal volume (Wendt et al., 2009)

3.1.1. Basic Governing Equations

The substantial derivative is a very important concept for fluid mechanics. The substantial derivative describes a material property change in time as it moves in space. It is divided into two parts, the convective derivative and the local derivative. The convective derivative describes the property change with respect to space while the local derivative describes the property change with respect to time. The following equation represents the substantial derivative operator.

$$\frac{D}{Dt} = \frac{\partial}{\partial t} + (\vec{v} \cdot \nabla) \quad (1)$$

where t is time and \vec{v} is the velocity vector. The term $\partial/\partial t$ represents the local derivative and the term $\vec{v} \cdot \nabla$ represents the convective derivative. The two main equations for fluid flow problems are the mass conservation equation and the Navier-Stokes equations. The mass conservation equation represents the idea that the mass in a control volume should remain constant. Thus, the net sum of mass flowing into the control volume and going out of the control volume should be zero. Using the differential formulation, it means that the substantial derivative of the mass differential dm is zero, that is:

$$\frac{D(dm)}{Dt} = 0 \quad (2)$$

The mass differential dm can be written as the product of the density ρ by the volume differential dV . Then, the mass conservation equation can be written as

$$\frac{D(\rho dV)}{Dt} = 0 \quad (3)$$

Since the differential volume dV is constant, the equation can be rewritten as

$$dV \frac{D\rho}{Dt} = 0 \quad (4)$$

$$\frac{D\rho}{Dt} = 0 \quad (5)$$

$$\frac{\partial \rho}{\partial t} + \nabla \cdot (\rho \vec{v}) = 0 \quad (6)$$

ANSYS uses a more general version of the mass conservation equation which considers a possible mass source S_m . This source is the mass added to the continuous phase from the dispersed second phase (for example, due to vaporization of liquid droplets) and any user-defined sources (ANSYS, 2018).

$$\frac{\partial \rho}{\partial t} + \nabla \cdot (\rho \vec{v}) = S_m \quad (7)$$

If no mass source is present, the temperature is constant and the flow is incompressible, the mass conservation equation can be simply written as

$$\nabla \cdot \vec{v} = 0 \quad (8)$$

The Navier-Stokes equations are obtained from Newton's second law, by summing all the forces applied to a control volume or infinitesimal volume. Figure 7 shows all the forces that are applied to an infinitesimal volume of fluid in the x direction.

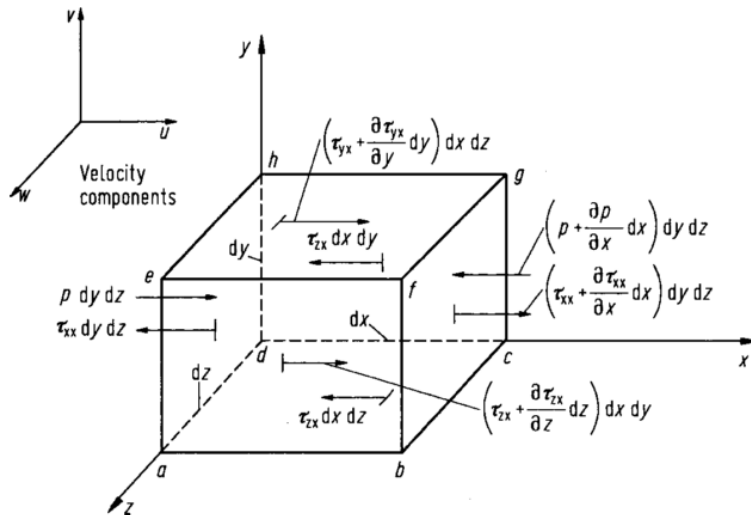


Figure 7 – Infinitesimally small, moving fluid element. Only the forces in the x direction are shown (Wendt et al., 2009)

A system of three equations (one for each direction) is obtained by summing all the forces in each direction. The complete deduction of the Navier-Stokes equations can be found in many books such as Batchelor (2000) and Wendt et al. (2009). Algebraic manipulations can be used to rewrite the Navier-Stokes equations in many different forms. ANSYS Fluent (ANSYS, 2018) combines the three equations into a linear system as shown:

$$\frac{\partial}{\partial t}(\rho \vec{v}) + \nabla \cdot (\rho \vec{v} \vec{v}) = -\nabla p + \nabla \cdot (\bar{\tau}) + \rho \vec{g} + \vec{F} \quad (9)$$

where p is the static pressure, $\rho \vec{g}$ and \vec{F} are the gravitational body force and external body forces, respectively, and $\bar{\tau}$ is the stress tensor given by

$$\bar{\tau} = \mu \left[(\nabla \vec{v} + \nabla \vec{v}^T) - \frac{2}{3} \nabla \cdot \vec{v} I \right] \quad (10)$$

where μ is the dynamic viscosity and I is the unit tensor. In this representation the velocity \vec{v} , gravity acceleration \vec{g} and external body force \vec{F} are vectors with components in the three directions. The stress tensor $\bar{\tau}$ is a three by three matrix and the pressure p is a scalar.

In CFD applications, a mesh is generated to divide the problem domain into cells. This is analogous to how finite element analysis applications are divided into elements. In Figure 3, part of the mesh is represented on the top-left corner. The governing equations are solved in each cell iteratively. In each iteration, convergence is checked by comparing the governing equations residue to a stop criterion.

3.1.2. Multiphasic System Modeling

The mass conservation and Navier-Stokes equations are enough to describe single-phase flows, but for biphasic flows (air-water), a multiphase model is also needed to locate the interface position. The Volume of Fluid model (VOF), introduced by Hirt and Nichols (1981) is an ideal multiphase model when there is a clear separation between the phases and no interpenetration,

such as the air-water interface in open-channel flow. The VOF model works by tracking the motion of fluid masses and determining the volume fraction in each mesh cell. The volume fraction α_w represents the percentage of the cell occupied by water. Figure 8a shows the α_w values in each cell of a hypothetical flow section.

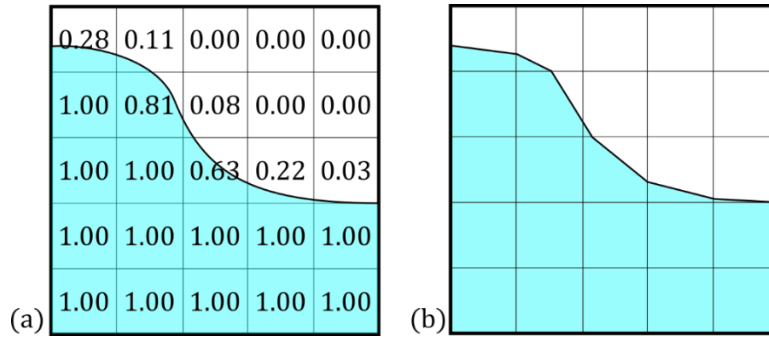


Figure 8 – VOF interface location: (a) real interface and (b) linear interpolation

If α_w is equal to one in a given cell in a given time, the entirety of the cell is filled with water. If α_w is equal to zero, then the entirety of the cell is filled with air. If α_w has any value between 0 and 1, then part of the cell is filled with water and the rest with air. This means that the free surface is localized in that cell.

The equations used to track the of the interface between each phase is described in the Fluent theory guide (2018). In a system with two phases (air and water), the tracking is accomplished by the solution of a mass conservation equation for one of the phases. For the water phase, the equation has the following form:

$$\frac{1}{\rho_w} \left[\frac{\partial}{\partial t} (\alpha_w \rho_w) + \nabla \cdot (\alpha_w \rho_w \vec{v}_w) \right] = S_{\alpha_q} + (\dot{m}_{aw} - \dot{m}_{wa}) \quad (11)$$

where ρ_w is the water density, α_w is the water volume fraction, \vec{v}_w is the water phase velocity vector, S_{α_q} is the water source term, \dot{m}_{wa} is the mass transfer from the water phase to the air phase, and \dot{m}_{aw} is the mass transfer from the air phase to the water phase. By default, S_{α_q} is zero, but the Fluent user can specify a value to it. When the implicit formulation is used, the volume fraction equation is discretized as

$$\frac{\alpha_w^{n+1}\rho_w^{n+1} - \alpha_w^n\rho_w^n}{\Delta t}V + \sum_f (\rho_w^{n+1}U_f^{n+1}\alpha_{w,f}^{n+1}) = [S_{\alpha_w} + \dot{m}_{aw} - \dot{m}_{wa}]V \quad (12)$$

where the superscript n is the index for the previous time step, the superscript $n + 1$ is the index for the current time step, the subscript f indicates that the parameter is evaluated at the face instead of in the cell, U_f^{n+1} is the volume flux through the face at the current time step and V is the cell volume.

The volume fraction equation is solved for the water phase to obtain α_w in each cell. The air volume fraction α_a is obtained as

$$\alpha_a = 1 - \alpha_w \quad (13)$$

When more than two phases are present, the volume fraction equation is solved for each phase, except the primary one. The primary phase volume fraction is obtained subtracting the sum of the other volume fractions from one.

The evaluation of the free surface profile is done by interpolating the volume fractions in neighbouring cells. Figure 8b shows interface location computed through CFD using linear interpolation. After computing the volume fractions, these values are used to perform a weighted average of the fluid properties, such as density and viscosity, in each cell. Thus, a generic fluid property φ is computed in each cell as

$$\varphi = \alpha_w\varphi_w + \alpha_a\varphi_a \quad (14)$$

Those averaged properties are the ones used in the Navier-Stokes and mass conservation equations.

3.1.3. Turbulence Model

In flows over dams and spillways, the vertical fluid acceleration on the downstream section and the possible hydraulic jump formation generates a significant amount of turbulence. Therefore, in addition to governing equations and the VOF model, a turbulence model is needed to determine the complex and erratic changes in pressures and velocities in open-channel flow systems. The Reynolds-Averaged Navier-Stokes (RANS) method is one of the most popular approaches because

it provides good accuracy for many engineering applications with a relatively small computational cost.

The RANS method decomposes the velocities in the Navier-Stokes equations into mean and fluctuating components. Thus, the velocity components v_i can be written as:

$$v_i = \bar{v}_i + v'_i \quad (15)$$

where \bar{v}_i and v'_i are the average and fluctuating velocity components. Other scalar quantities, like pressure, can be decomposed in average and fluctuating components in the same way. Substituting the velocity vectors by its components in the Navier-Stokes equations and dropping the overbar on the mean velocity \bar{v}_i , the following form of the Navier-Stokes equations is obtained:

$$\frac{\partial}{\partial t}(\rho v_i) + \frac{\partial}{\partial x_j}(\rho v_i v_j) = -\frac{\partial p}{\partial x_i} + \frac{\partial}{\partial x_j} \left[\mu \left(\frac{\partial v_i}{\partial x_j} + \frac{\partial v_j}{\partial x_i} - \frac{2}{3} \delta_{ij} \frac{\partial v_l}{\partial x_l} \right) \right] + \frac{\partial}{\partial x_j} (-\rho \overline{v'_i v'_j}) \quad (16)$$

where δ_{ij} is the Kronecker delta and $-\rho \overline{v'_i v'_j}$ are the Reynolds stresses. By doing this, additional terms that represent the effects of turbulence appear in the Navier-Stokes equations. According to the Boussinesq hypothesis, the Reynolds stresses are defined as:

$$-\rho \overline{v'_i v'_j} = \mu_t \left(\frac{\partial v_i}{\partial x_j} + \frac{\partial v_j}{\partial x_i} \right) - \frac{2}{3} \left(\rho k + \mu_t \frac{\partial v_k}{\partial x_k} \right) \delta_{ij} \quad (17)$$

where μ_t is the turbulent viscosity and k is the turbulence kinetic energy. The turbulence terms are modelled using a turbulence model, such as the k- ε model or k- ω model.

The k- ε model, introduced by Launder and Spalding (1974), is widely used in many industrial applications due to its good accuracy, fast convergence and low computational cost, especially in internal flows. In this model, the turbulent viscosity is defined as:

$$\mu_t = \rho C_\mu \frac{k^2}{\varepsilon} \quad (18)$$

where ε is the dissipation rate and C_μ is a model constant. The turbulence kinetic energy k and the dissipation rate ε are obtained from the following transport equations:

$$\frac{\partial}{\partial t}(\rho k) + \frac{\partial}{\partial x_i}(\rho k v_i) = \frac{\partial}{\partial x_j} \left[\left(\mu + \frac{\mu_t}{\sigma_k} \right) \frac{\partial k}{\partial x_j} \right] + G_k + G_b - \rho \varepsilon - Y_M + S_k \quad (19)$$

$$\frac{\partial}{\partial t}(\rho \varepsilon) + \frac{\partial}{\partial x_i}(\rho \varepsilon v_i) = \frac{\partial}{\partial x_j} \left[\left(\mu + \frac{\mu_t}{\sigma_\varepsilon} \right) \frac{\partial \varepsilon}{\partial x_j} \right] + C_{1\varepsilon} \frac{\varepsilon}{k} (G_k + C_{3\varepsilon} G_b) - C_{2\varepsilon} \rho \frac{\varepsilon^2}{k} + S_\varepsilon \quad (20)$$

where G_k is the generation of turbulence kinetic energy due to the mean velocity gradients, G_b is the generation of turbulence kinetic energy due to buoyancy, Y_M is the contribution of the fluctuating dilatation in compressible turbulence to the overall dissipation rate, $C_{1\varepsilon}$, $C_{2\varepsilon}$ and $C_{3\varepsilon}$ are model constants, σ_k and σ_ε are the Prandtl numbers for k and ε , respectively and S_k and S_ε are user-defined source terms. The model constants, as recommended by Launder and Spalding (1974) are shown in Table 1.

Table 1 – Constants from the k- ε model

$C_{1\varepsilon}$	$C_{2\varepsilon}$	C_μ	σ_k	σ_ε
1.44	1.92	0.09	1.0	1.3

However, in external flows, the k- ε model does not perform well due to its insensitivity to adverse pressure gradients. On the other hand, the k- ω model introduced by Wilcox (1988) can represent well pressure gradients in boundary layers but struggles in the freestream region compared to the k- ε model. The k- ω model defines the turbulent viscosity μ_t as:

$$\mu_t = \alpha^* \frac{\rho k}{\omega} \quad (21)$$

where ω is the specific dissipation rate and α^* is a coefficient for low-Reynolds number correction. The turbulence kinetic energy k and specific dissipation rate ω are obtained from the following transport equations:

$$\frac{\partial}{\partial t}(\rho k) + \frac{\partial}{\partial x_i}(\rho k v_i) = \frac{\partial}{\partial x_j} \left(\Gamma_k \frac{\partial k}{\partial x_j} \right) + G_k - Y_k + S_k \quad (22)$$

$$\frac{\partial}{\partial t}(\rho\omega) + \frac{\partial}{\partial x_i}(\rho\omega v_i) = \frac{\partial}{\partial x_j}\left(\Gamma_\omega \frac{\partial \omega}{\partial x_j}\right) + G_\omega - Y_\omega + S_\omega \quad (23)$$

where Γ_k and Γ_ω represent the effective diffusivity of k and ω , respectively, G_k represents the generation of k due to mean velocity gradients, G_ω represents the generation of ω , Y_k and Y_ω represent the dissipation of k and ω and S_k and S_ω are user-defined source terms.

The shear stress transport (SST) k - ω model developed by Menter (1993) combines the advantages of both models by applying the k - ω model in the boundary layer region and the k - ϵ model in the freestream. Therefore, the SST k - ω model is most appropriate to study overtopped gravity dams and spillways and is the turbulence model selected for this work.

3.1.4. Solution Methodology

There are two big families of solvers for flow problems: pressure-based solvers and density-based solvers. Pressure-based solvers were developed for low-speed incompressible flows while density-based solvers were developed for high-speed compressible flows. However, as both methods evolved, both became able to solve problems with flow conditions outside their original intent (ANSYS, 2018). In this work, only incompressible flows are analyzed, so a pressure-based solver is used.

Pressure-based solvers use a pressure correction equation obtained from the mass conservation and Navier-Stokes equations to compute the pressure fields. The solution method consists of dividing the domain into discrete control volumes using a computational grid. Then the governing equations are integrated into each control volume to obtain algebraic equations. These equations are linearized and solved to obtain the velocity and pressure fields (ANSYS, 2018).

Pressure-based solvers can be divided into segregated and coupled algorithms. In the segregated algorithm, the governing equations for each variable (velocity in each direction, pressure, temperature, etc) are solved one at a time, sequentially. The solution process for the segregated algorithm is described in Fluent theory guide as (ANSYS, 2018):

1. Update the flow properties such as density and viscosity based on the current solution;
2. Solve the Navier-Stokes equations sequentially using the most up-to-date values of pressure and mass fluxes;
3. Solve the pressure correction equation with the recently obtained velocity field and mass-flux;
4. Correct the mass fluxes, pressure and velocity fields using the pressure correction just obtained;
5. Solve the equations for additional scalars such as the turbulent quantities and volume fractions;
6. Update source terms arising from the interactions among different phases (which are not present in any of the simulations in this work);
7. Check for convergence of the equations

The process described above is one iteration of the solution method. New iterations are run until convergence is reached. Then, the solution advances one time step and a new set of iterations is run. The coupled algorithm solution process differs from the segregated one as all the equations in steps 2 and 3 are solved as a system of equations in a single step. Because of this, the coupled algorithm requires fewer iterations but uses significantly more system memory. Figure 9 shows an overview of both segregated and coupled algorithms.

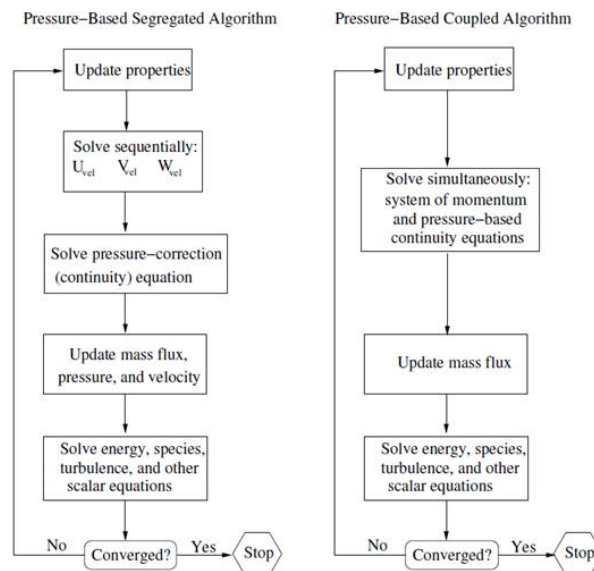


Figure 9 – Fluent solution workflow for pressure-based methods (ANSYS, 2018)

The pressure-based segregated algorithm has some variants that add some modifications to the procedure that was just described. The SIMPLE (Semi-Implicit Method for Pressure Linked Equations) algorithm is the standard one and works just as described above. It is recommended for most flow cases. The SIMPLEC (SIMPLE-Consistent) algorithm is a variant that aims to accelerate convergence for simple (laminar) flows. However, if the mesh is highly skewed or if the flow is very turbulent, using the SIMPLEC algorithm might lead to convergence problems.

The PISO (Pressure-Implicit with Splitting of Operators) algorithm introduces neighbour correction and skewness correction to address the problem that the new velocities and corresponding fluxes do not satisfy the momentum balance after the pressure-correction equation is solved in the SIMPLE and SIMPLEC algorithms. By solving this problem, the number of iterations needed for convergence is reduced. The neighbour correction means that the pressure-correction equation step is solved iteratively so that the corrected velocities satisfy the Navier-Stokes and pressure-correction equations more closely. The skewness correction uses the pressure-correction gradient to recalculate the mass flux correction, which facilitates convergence in highly distorted meshes. Due to these modifications, the PISO algorithm takes more time to perform each iteration but requires fewer iterations to converge. This algorithm is recommended for transient flow calculations with highly distorted meshes and when you want to use a large time step.

In this work, the SIMPLE algorithm is used in all problems. This is because the flow is generally turbulent, so the SIMPLEC algorithm would not be recommended, and the mesh is not very distorted. Some tests with the PISO algorithm were run but no significant improvement in computational time was observed for our specific cases.

3.1.5. Numerical Methods

Inside each of the solution iteration steps, many numerical methods are required to solve the governing equations. These include numerical methods for calculation of gradients, pressures, velocities, volume fractions, turbulence parameters and time discretization. Each of these

numerical methods is described by Fluent theory guide (ANSYS, 2018) and the choice for each one was made based on the manual recommendation.

The calculation of both the velocities (through Navier-Stokes equations) and turbulent parameters (such as the turbulent kinetic energy k and specific dissipation rate ω) fall into the spatial discretization category. For these variables, in our flow cases, Fluent offers the First Order Upwind, Second Order Upwind, Power Law, QUICK and Third-Order MUSCL schemes. The First Order Upwind scheme is recommended for simple flows aligned with the mesh, while the Second Order Upwind scheme is more robust and capable of running more complex flows and achieve better accuracy. The downside, however, is that the Second Order Upwind scheme does not converge as easily as the First Order Upwind scheme. The other schemes offer higher accuracy for the cost of higher computational time. For these variables, the Second Order Upwind scheme was selected.

The pressure calculation also falls into the spatial discretization category. However, the available discretization schemes are different. For multiphasic flows, only the PRESTO! and Body Force Weighted schemes are available. For single-phase flows the Linear, Second Order and Standard schemes are also available. The Second Order scheme is recommended for most cases since it is more accurate than the Linear and Standard schemes while keeping the computational cost low. This scheme is used for the single-phase flow problems presented herein. The Body Force Weighted scheme is used for the multiphasic flows because it is recommended over PRESTO! when there are known and relevant body force in the model, which in our case is the gravitational force.

The volume fraction schemes are used to interpolate the volume fractions among the cells and capture the interface between phases. The Geo-Reconstruct, CICSAM, Modified HRIC and Compressive schemes are available. The Modified HRIC is chosen because it provides very good accuracy with a smaller computational cost if compared to the more accurate Geo-Reconstruct scheme.

For gradient calculation, the Green-Gauss Cell Based, Green-Gauss Node Based and Least Squares Cell Based schemes are available. The Least Squares Cell Based scheme is the Fluent default and the one selected here because it is generally much more precise than the Green-Gauss Cell Based

scheme and has similar accuracy and lower computational cost than the Green-Gauss Node Based scheme.

The temporal discretization is used for the integration of the time-dependent terms over a time step Δt . This discretization is necessary in transient cases. Fluent offers implicit and explicit formulations. The explicit formulation is only available when using the density-based solver and it is dependent on the CFL condition (mentioned later in this work) for stability. The implicit formulation, on the other hand, is unconditionally stable with respect to the time step size. The temporal discretization can be done with first or second order finite differences method. The Second Order Implicit scheme is used in all cases.

3.2. Expected Loads on Spillways and Gravity Dams

The main type of concrete dam is the gravity dam. This type of dam typically has a roughly trapezoidal shape where the base is much broader than the crest. Its shape is designed so that the dam self-weight acts as its main stabilizing force. If properly designed, gravity dams require very little maintenance.

The main loads in any dam under normal conditions are its self-weight, the hydrostatic forces upstream and downstream and the uplift force. Beyond these, there might also be loads due to floating debris, silt, ice, waves, earthquakes and overtopping. Figure 10a shows all loads that are considered in the static analysis of dams in a flood scenario including overtopping. On the other hand, Figure 10b shows the loads that are expected to be obtained with CFD. The hydrostatic pressure p_w upstream and downstream are calculated as

$$p_w = \gamma_w z \quad (24)$$

where γ_w is the water specific weight and z is the water depth. The hydrostatic forces can be computed by integrating the pressure field over the wetted area.

The dam self-weight W is computed as

$$W = \gamma_c V_c \quad (25)$$

where γ_c is the concrete specific weight and V_c is the dam volume.

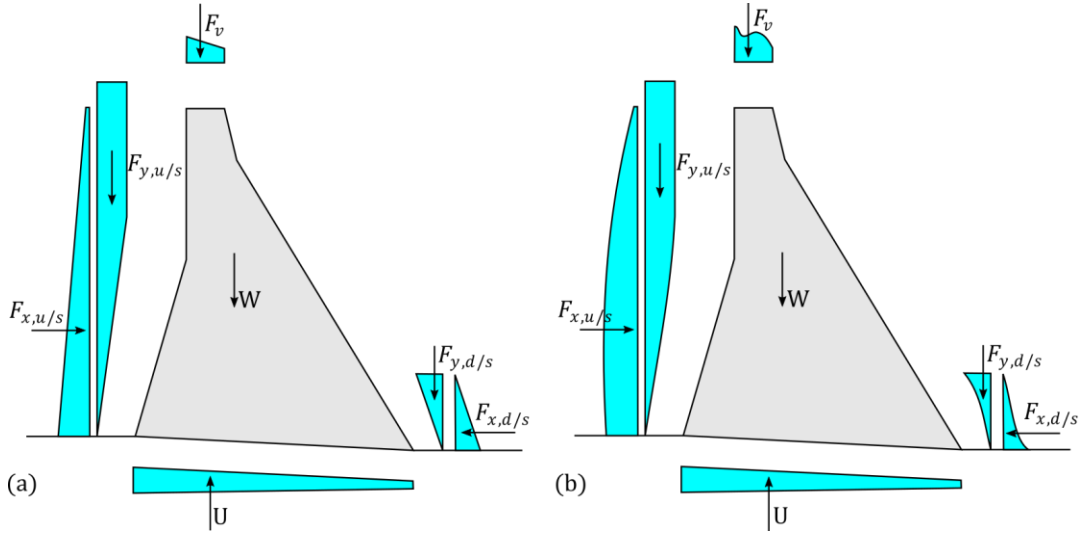


Figure 10 – Expected loads on a gravity dam: (a) estimated loads provided by guidelines and (b) hydrodynamic loads obtained with CFD

The uplift pressure is a little harder to compute. Figure 11 shows that the real uplift pressure field depends on the flownet through the dam and its foundation. The theoretical pressure distribution is non-linear, but for design purposes, a linear envelope is assumed.

The upstream uplift pressure $p_{u,u/s}$ is computed as

$$p_{u,u/s} = \gamma_w z_{u/s} \quad (26)$$

where $z_{u/s}$ is the total water depth upstream.

The downstream uplift pressure $p_{u,d/s}$ is computed as

$$p_{u,d/s} = \gamma_w z_{d/s} \quad (27)$$

where $z_{d/s}$ is the tailwater depth. If the dam is equipped with a drain to reduce the uplift pressure, the uplift distribution becomes bilinear, as shown in Figure 11. The upstream and downstream

uplift pressures are still computed the same way and the uplift pressure reduction at the drain is proportional to its efficiency.

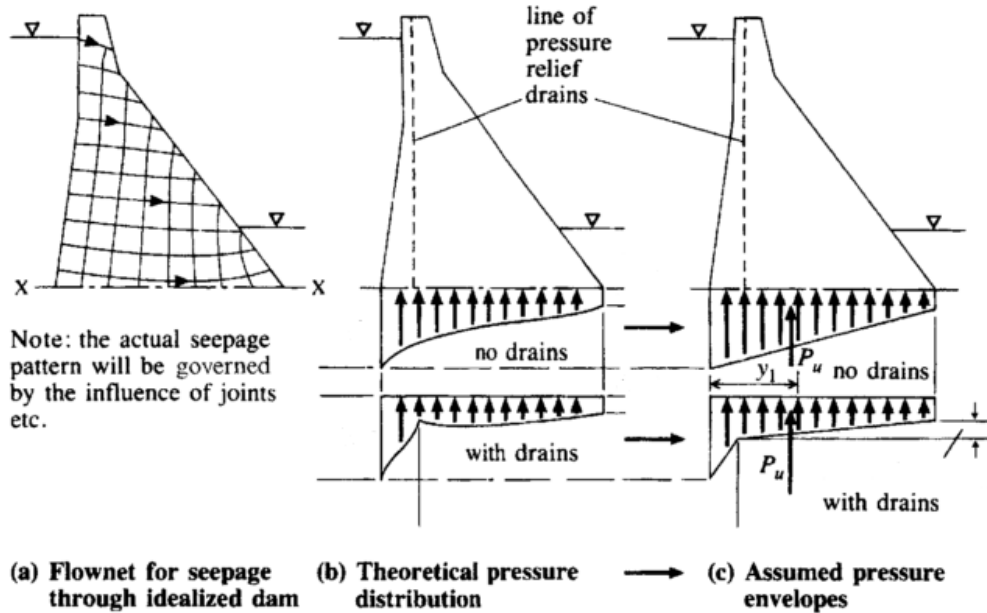


Figure 11 – Uplift pressure distribution (Novak et al., 2007 - adapted)

The uplift force U is computed by integrating the uplift pressure field over the area of the dam base. If the uplift pressure field and the dam base geometry is constant along its length and if no drain is present, U is computed as

$$U = LB_0 \frac{(p_{u,u/s} + p_{u,d/s})}{2} \quad (28)$$

$$U = LB_0 \gamma_w \frac{(z_{u/s} + z_{d/s})}{2} \quad (29)$$

where L is the dam length and B_0 is the dam base width.

Overtopping could also affect non-overflow gravity dam sections with flat crests that will then be subjected to stabilizing or destabilizing forces of unknown magnitude and for which there is no validated or verified guidance in the existing dam safety guidelines (USBR 1987, ANCOLD 1991, FERC 1991, USACE 1995, CDA 2013, FERC 2016). For overtopped gravity structures, USACE

(1995) and FERC (2016) suggest ignoring the stabilizing weight of the water nappe on top of the structure and reducing the tailwater head to 60% of the expected value to avoid overestimating the downstream stabilizing forces in case of hydrodynamic effects. This reduction is not applied to evaluate the uplift pressure acting at the toe. It is common to estimate the expected tailwater head $H_{d/s}$ as being equal to the overtopping height H_0 for overtopped dams. FERC (2016) mentions that for small discharges, nappe forces may be neglected in stability analyses of overflow spillways; however, for significant discharges, "nappe forces can become significant and should be taken into account in the analysis of dam stability". FERC (1991) presented an alternative method to CFD to estimate the nappe forces. It requires the implementation and numerical solution of energy-flow equations according to the curvature of streamlines that are assumed to change gradually with respect to the distance along the streamline parallel to the spillway. This method is not applicable when there are sharp geometric discontinuities in the studied hydraulic structures, such as in gravity dams with typical sections. However, FERC (1991) presented a computational stability example in the Appendix of an overtopped gravity dam using a very simple rule of thumb. The stabilizing vertical nappe pressures correspond to the water head H_0 over the upstream edge of the crest and one-half of this value ($H_0/2$) at the downstream edge (Figure 12).

Thus, using the rule of thumb, the vertical force on the crest F_v can be estimated as

$$F_v = 0.75\gamma_w LBH_0 \quad (30)$$

where B is the dam crest width.

It is also noted in FERC (1991) that "the pressure distribution on the crest has been assumed, the actual distribution may vary". This last comment motivated our research to use CFD to provide validated recommendations to the profession to define the magnitude of the vertical nappe force resultant and its location on the crest.

Figure 12 shows the possible failure mechanisms for an overtopped gravity dam. It also shows the expected flow conditions for different parts of the domain.

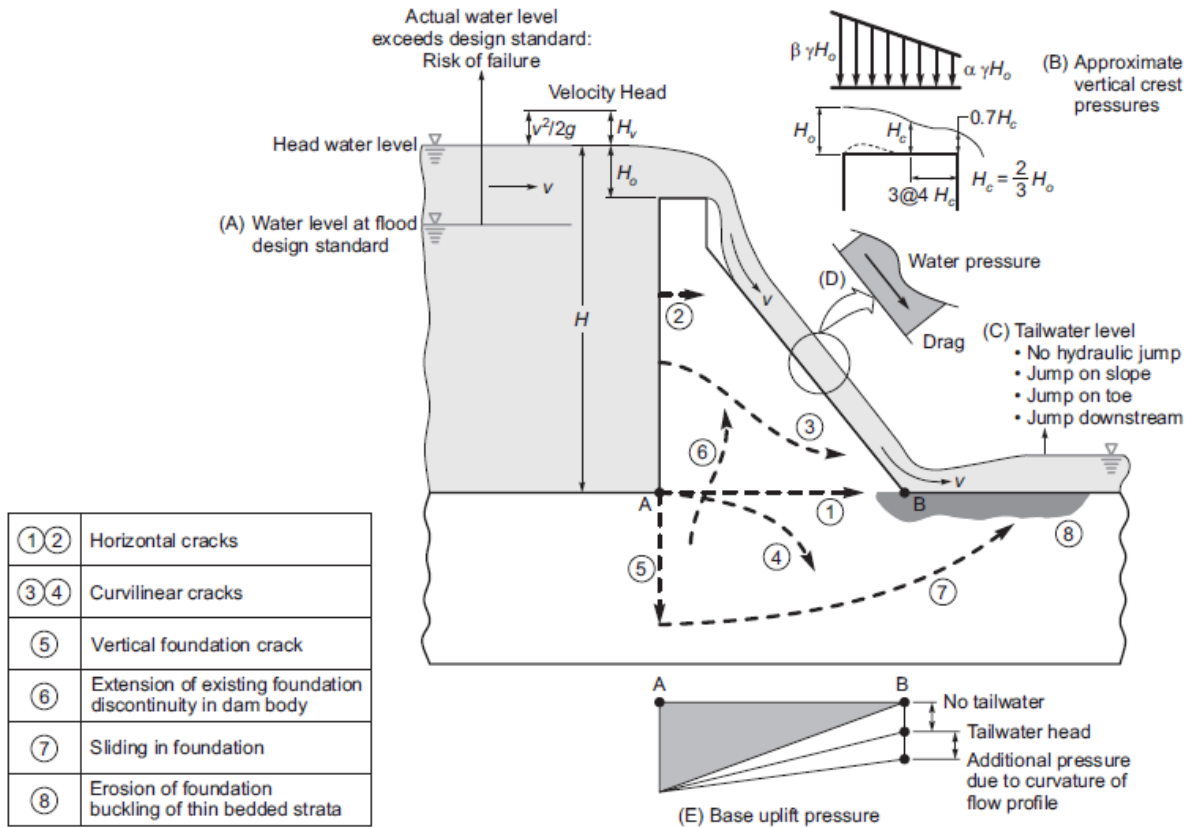


Figure 12 – Failure mechanisms of an overtopped dam (Léger, 2019)

4. CFD PRELIMINARY RESULTS - VALIDATIONS AND VERIFICATION

In this chapter, a series of models are simulated to progressively validate the numerical methods, techniques and boundary conditions used in the case studies. First, the flow around a square cylinder is modelled to validate the software and choice of turbulence model. Then, a water tap model is simulated to validate the multiphasic model and obtain insight into the mesh refinement necessary. Next, a spillway is modelled to validate the boundary conditions. Finally, a rectangular broad-crested weir is modelled to validate the flow aeration technique.

4.1. Flow Around a Square Cylinder

The flow around a cylinder is a well know problem with analytical solutions and a lot of experimental data that can be found in the literature. This problem occurs in structural engineering in situations such as the flow of air around tall buildings and the flow of water around off-shore platform columns, for example. This type of flow is characterized by the formation of vortices behind the cylinder. The vortex pattern is dependant on the Reynolds number. For very low Reynolds number, a pair of stationary vortices are formed behind the cylinder. As the Reynolds number increases and the flow transitions from laminar to turbulent, an alternating vortex street wake is formed behind the cylinder. This phenomenon is called von Karman vortex shedding.

The flow around a square cylinder is studied here as the first validation problem for Fluent. The problem is studied in 2D using the geometry presented in Figure 13. The computational domain consists only in the fluid domain, that is, the region where the fluid can be present. This means that the structure is represented as a void in the geometry. Thus, only the walls of the structure are represented and the structure itself is modelled as being perfectly rigid.

In Figure 13, The left boundary is a velocity inlet and the right boundary is a pressure outlet. The upper and bottom boundaries are slip walls while the square walls in the middle are set to no-slip

walls. The velocity in the inlet is adjusted to achieve a desired Reynolds number. The Reynolds number Re is calculated as

$$Re = \frac{\rho v D}{\mu} \quad (31)$$

where ρ is the water density (998.2 kg/m^3), v is the velocity at the inlet, D is the cylinder diameter and μ is the water kinematic viscosity ($1.003 \cdot 10^{-3} \text{ kg/m.s}$). The pressure in the outlet is set to the reference atmospheric pressure, in this case, 0 Pa . The cylinder diameter used in all simulations is 1 m .

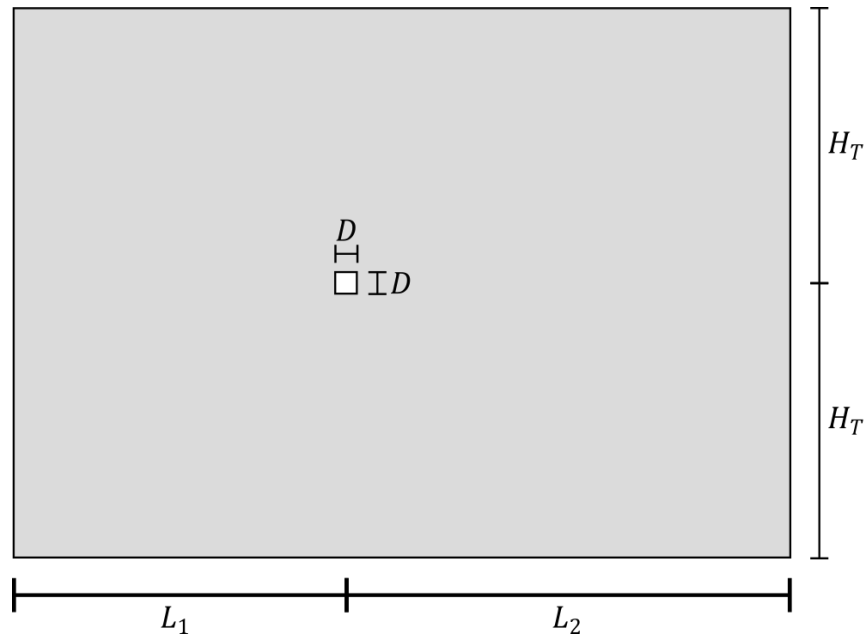


Figure 13 – Geometry model for flow over a square cylinder

The mesh used in this problem is a structured mesh with a bias towards the cylinder. In fact, the choice of studying a square cylinder over a circular cylinder was motivated by the fact that with the square one, a structured mesh can be used. This simplifies the numerical solution and helps to avoid numerical errors due to an irregular mesh. The bias towards the cylinder means that the cells that are closer to the cylinder are smaller than the ones that are further from it. For this study, a

bias factor of 4 was used to generate the mesh. This means that the cells adjacent to the cylinder are 4 times smaller than the ones that are furthest from the structure. Since the same cell size is used in the x and y directions, the bias factor can be defined as

$$\text{Bias Factor} = \frac{\xi_0}{\xi_n} = \frac{\eta_0}{\eta_n} \quad (32)$$

where ξ_0 , ξ_n , η_0 and η_n are the cell side dimensions shown in Figure 14a. A finalized mesh used in this validation problem is shown in Figure 14b.

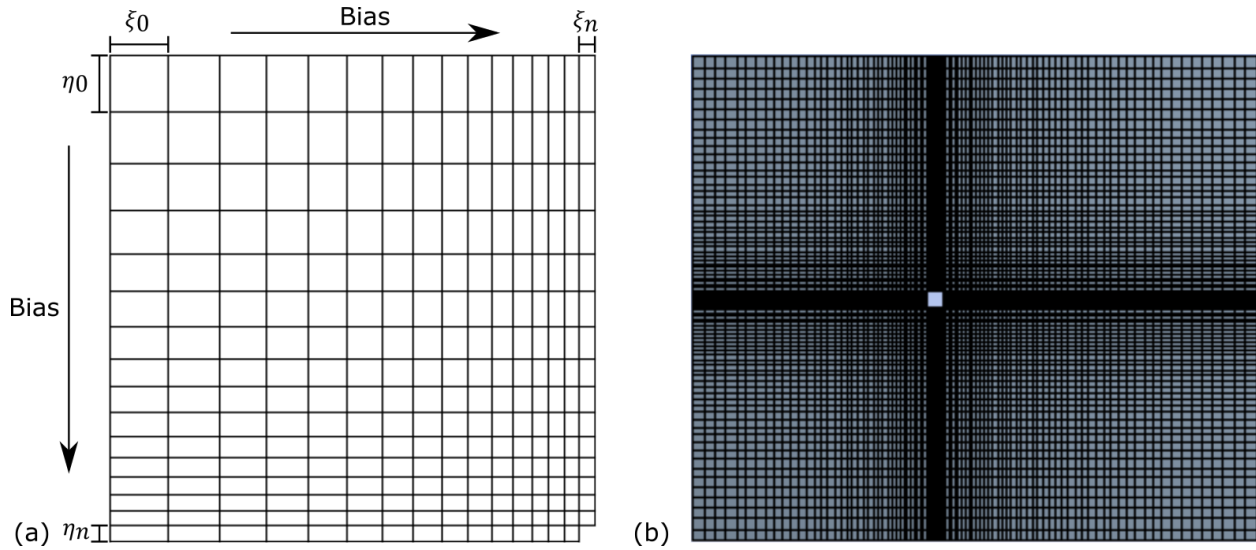


Figure 14 – Flow over a square cylinder mesh: (a) Biasing detail and (b) complete mesh

After defining the geometry and the mesh on ANSYS, the boundary conditions and material properties, are input into Fluent and the models and solution methods are chosen. Drag coefficients C_d and lift coefficients C_l are monitored during the solution. The drag and lift coefficients can be defined as:

$$C_d = \frac{2F_d}{\rho v^2 A} \quad (33)$$

$$C_l = \frac{2F_l}{\rho v^2 A} \quad (34)$$

where F_d and F_l are the drag and lift forces and A is the reference area. The drag and lift forces are the components of the total force applied by the fluid on the structure parallel and perpendicular to the flow direction, respectively. The total force can be obtained by integrating the pressure fields on the structure surface.

In transient cases with alternate vortex shedding, the simulation is run until the drag and lift coefficients reach steady state, oscillating around the same values in every cycle. Figure 15 shows how these coefficients vary during a simulation.

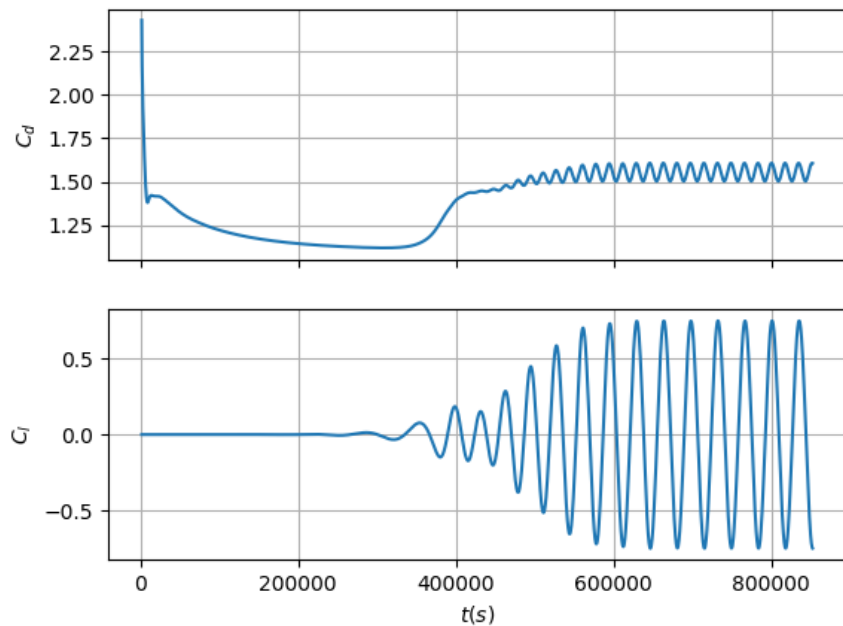


Figure 15 – Drag coefficient (C_d) and lift coefficient (C_l) in a transient simulation

4.1.1. Steady State Laminar Flow

The first set of simulations for the flow around a square cylinder is done using a steady state and laminar flow models. The Reynolds number is kept below 60 to ensure that only a stationary vortex is formed behind the cylinder. Then, a domain convergence study with $Re = 40$ is conducted to find the minimum appropriate dimensions for L_1 , L_2 and H_T with respect to the cylinder diameter

D. First, the dimensions L_2 and H_T were set to $20D$ and $15D$, respectively while the dimension L_1 was varied from $5D$ to $50D$. The drag coefficient C_d was obtained for each variation of L_1 . The same was done to L_2 while L_1 and H_T were set to $15D$ each, and to H_T while L_1 and L_2 were set to $15D$ and $20D$, respectively. The results are shown in Figure 16. The figure shows that adopting values smaller than $15D$ for L_1 , $10D$ for L_2 and $15D$ for H_T leads to considerable relative error. Otherwise, the error with respect to the highest adopt dimension is inferior to 1%. That is because as the boundaries become too close to the structure, the boundary conditions end up affecting the response close to the cylinder. Thus, we decided to keep using the values of $L_1 = 15D$, $L_2 = 20D$ and $H_T = 15D$.

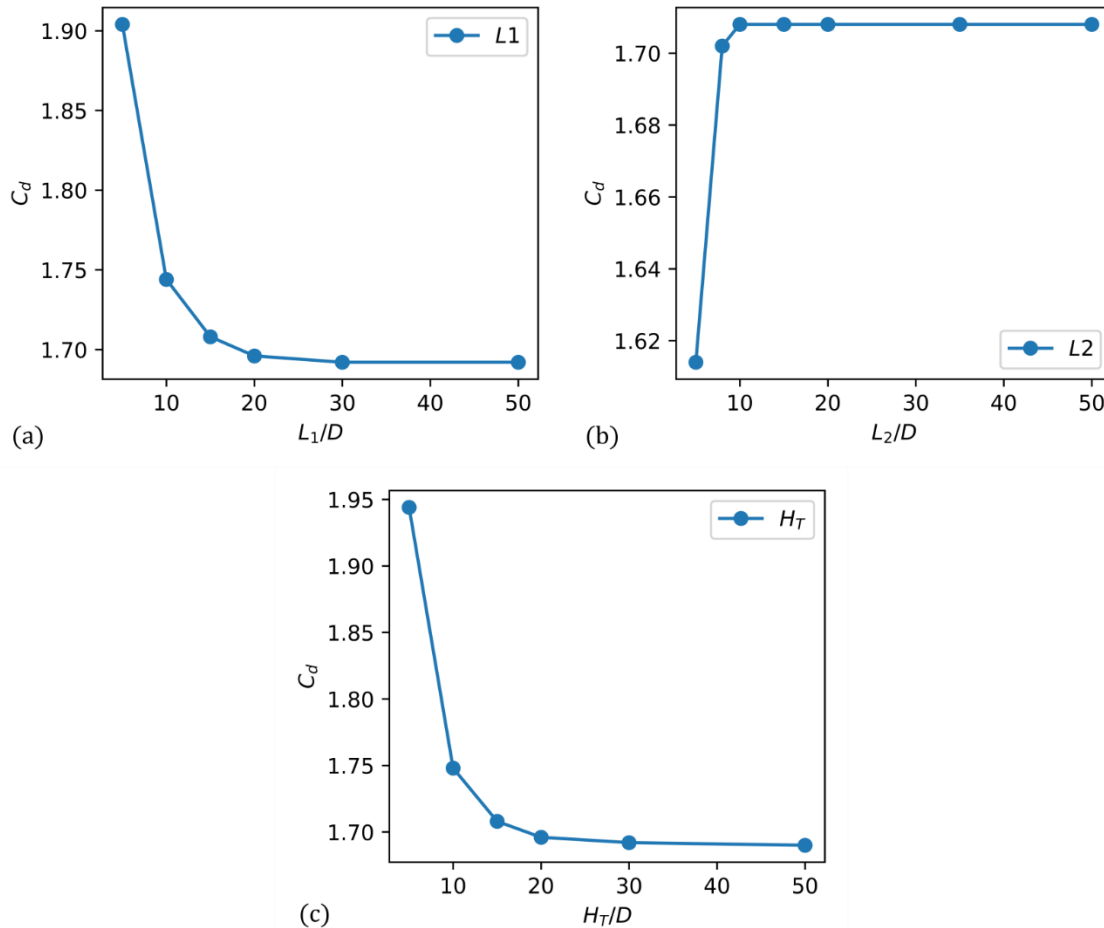


Figure 16 – Domain convergence for steady-state laminar flow over a square cylinder ($Re = 40$): (a) upstream length L_1 (b) downstream length L_2 and (c) domain height H_T

Next, a mesh convergence study with $Re = 40$ is conducted to find the minimum refinement required for convergence. The bias factor is fixed at 4 and the number of cells per meter on the interface between the fluid and the structure is varied. The drag coefficient is monitored and the results are presented in Figure 17. The figure shows that for more than 8 cells/m, the relative error with relation to the finest mesh is inferior to 1%. Bellow that, the relative error increases significantly and for 2 cell/m it reaches about 10%. Thus, a mesh with 40 cells/m was chosen as it yields very accurate results with a reasonable computational time.

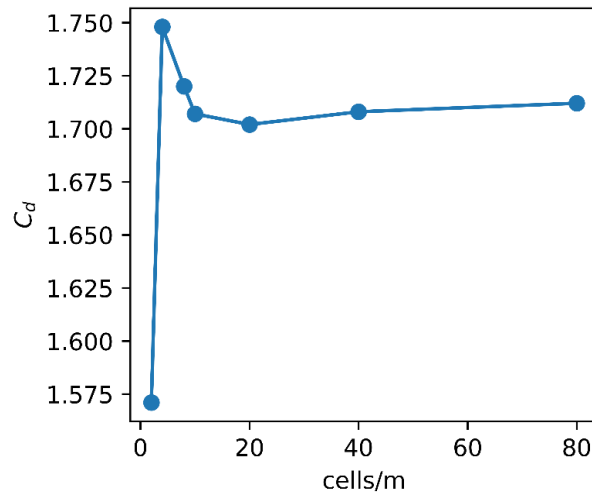


Figure 17 – Mesh convergence for steady-state laminar flow over a square cylinder ($Re = 40$)

Using a mesh with 40 cells/m, $L_1 = 15D$, $L_2 = 20D$ and $H_T = 15D$, the drag coefficient was evaluated for different Reynolds numbers. The results were compared with four cases found in the literature. Breur et al. (2000) computed the drag coefficients using two different methods: lattice-Boltzmann automata (LBA) and finite volume method (FVM). Dhiman et al. (2006) used the power-law fluid theory to study the flow around a square cylinder. Lamura et al (2001) used the multi-particle collision dynamics method to study the same problem. Figure 18 shows that the drag coefficients obtained with Fluent are in accordance with what was found by all these authors.

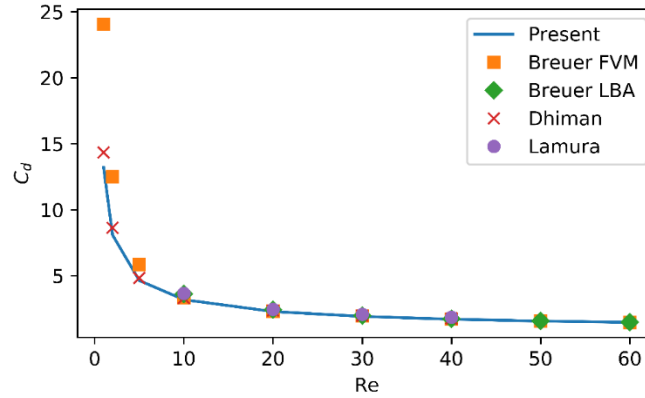
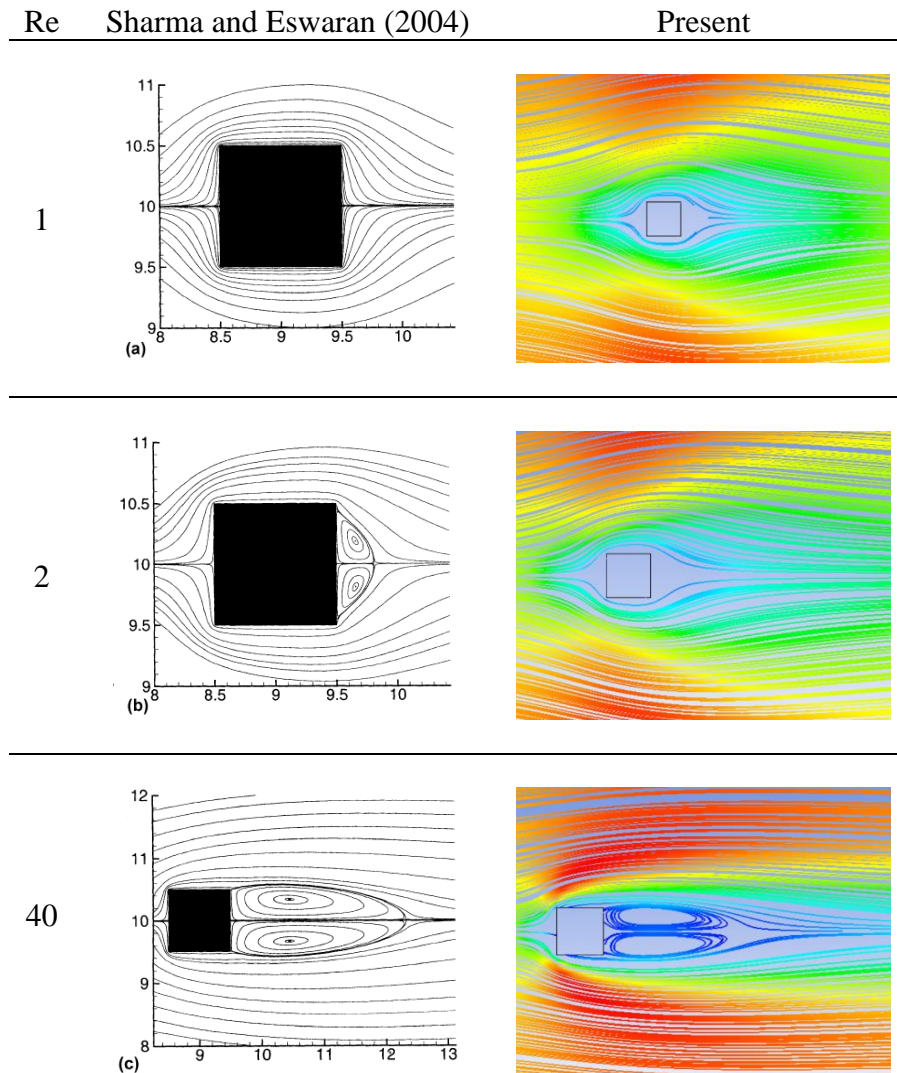


Figure 18 – Steady-state laminar flow over a square cylinder validation

The streamline patterns are compared with results presented by Sharma and Eswaran (2004). From Table 2, it can be noted that the streamlines patterns obtained are very similar to the ones found in the literature. Also, the pair of stationary vortices can be easily seen for $Re = 40$ as expected.

Table 2 – Comparison of streamlines for steady laminar flow around a square cylinder for multiple Reynolds numbers



4.1.2. Transient Laminar Flow

Transient laminar flow is now modelled using Reynolds numbers from 50 to 200. In this range, the vortex wake starts to become unstable and the von Karman vortex street is formed. The alternate vortex shedding produces varying lift and drag force. The drag force oscillates around a mean value while the lift force oscillates around zero. Also, the drag force oscillation frequency is double the lift force oscillation frequency (Figure 15).

A domain convergence study was done for the transient laminar flow using $Re = 200$. The methodology used here is the same that was used in the steady-state laminar flow. The results are shown in Figure 19. However, this time, the mean drag coefficient C_d , the maximum lift coefficient $C_{l,max}$ and the root mean square of the lift coefficient $C_{l,rms}$ are plotted. Once again, it can be seen that the values $L_1 = 15D$, $L_2 = 20D$ and $H_T = 15D$ are sufficient for convergence. This means that these values can be used for mesh convergence and validation. However, the downstream length L_2 is increased to $50D$ for the purpose of capturing more of the von Karman street and its dissipation. The upstream length and domain height are kept at $L_1 = 15D$ and $H_T = 15D$, respectively.

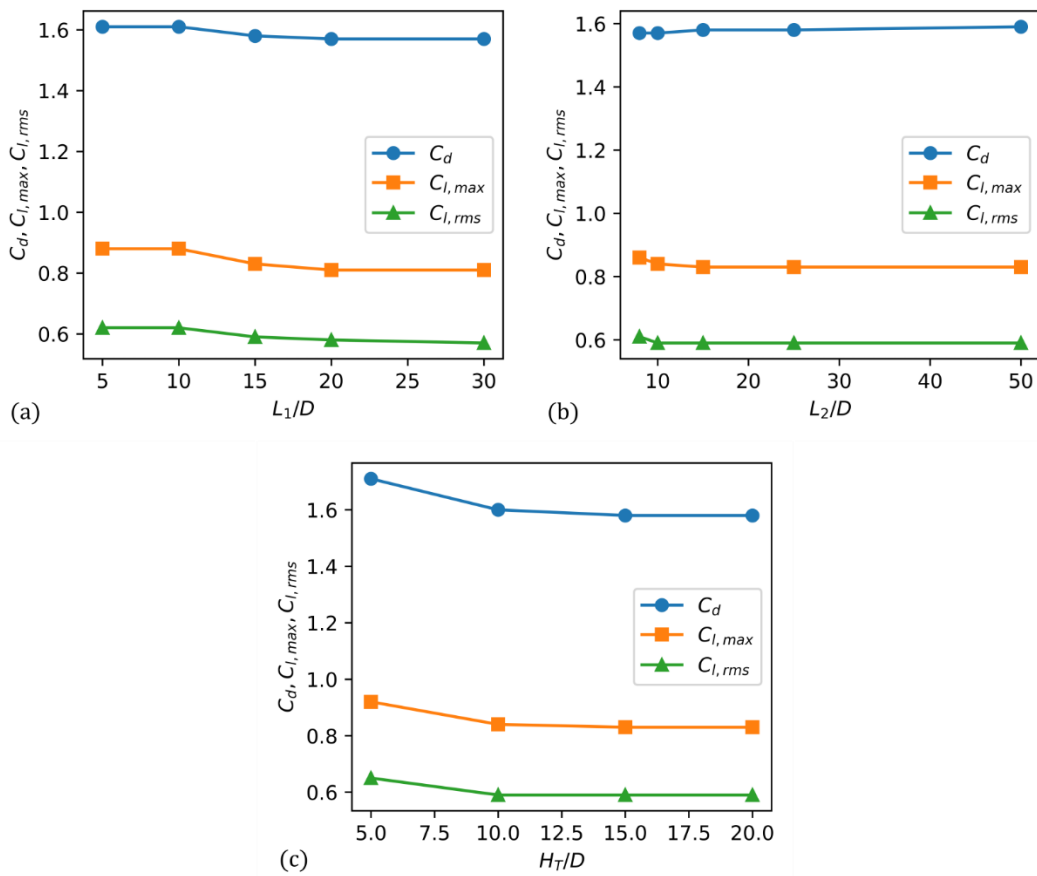


Figure 19 – Domain convergence for transient laminar flow over a square cylinder ($Re = 200$):
 (a) upstream length L_1 (b) downstream length L_2 and (c) domain height H_T

A mesh convergence study is conducted for the transient laminar flow using $Re = 200$. Once again, the bias factor was set to 4 and the number of cells per meter on the interface between the fluid and the structure is varied. The mean drag coefficient C_d , maximum lift coefficient $C_{l,max}$ and root mean square of the lift coefficient $C_{l,rms}$ are monitored. Figure 20 shows that the transient case is more sensitive to mesh refinement than the steady-state case, especially for the average drag coefficient. Nevertheless, the mesh with 40 *cells/m* still yield less than 5% relative error as compared to the finest mesh (50 *cells/m*).

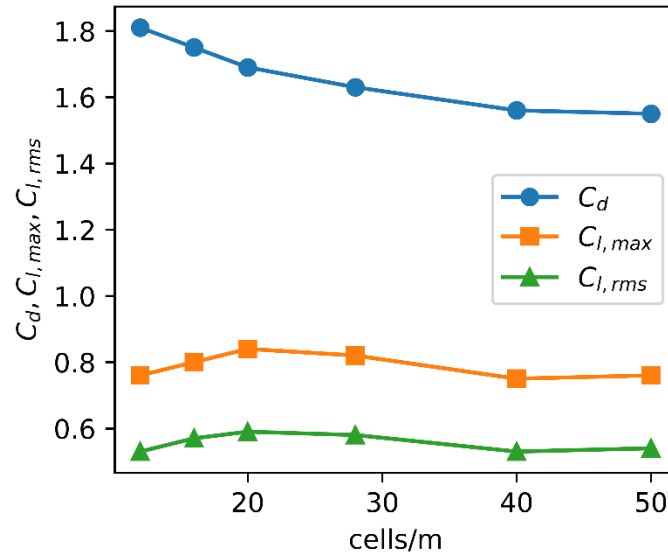


Figure 20 – Mesh convergence for transient laminar flow over a square cylinder ($Re = 200$)

The transient solution convergence is very dependent on the time step size used in each iteration. There are multiple convergence criteria for transient flows. The first criterium is the CFL condition, which states that the Courant number C should be smaller than a maximum value C_{max} , usually assumed as 1. The Courant number is the relation between the space travelled by a particle of water in one time step and the mesh size. It is defined as

$$C = \frac{v\Delta t}{\Delta x} \leq C_{max} \quad (35)$$

where v is the velocity of the particle, Δt is the time step size and Δx is the cell length in the direction of v . If the CFL condition is met, the results are likely to converge. However, in some cases, convergence can be achieved even if C is greater than 1.

For the transient laminar flow around a square cylinder with low Reynolds number, the CFL condition yields a very conservative time step, thus, another criterion is used. Since the vortex shedding is a periodic event, the time step can be defined as a fraction of the vortex shedding period T . Thus, the ratio n between the period T and the time step Δt can be written as

$$\frac{T}{\Delta t} = n \quad (36)$$

The Strouhal number is defined as the ratio between the cylinder diameter and the distance travelled by a water particle in one vortex shedding cycle. It can be written in terms of the vortex shedding period as

$$St = \frac{D}{Tv} \quad (37)$$

where T is the vortex shedding period, D is the cylinder diameter and v is the flow velocity at a distance. Thus, if the Strouhal number is known, the time step can be estimated as

$$\Delta t = \frac{T}{n} \quad (38)$$

$$\Delta t = \frac{D}{nvSt} \quad (39)$$

A time step convergence analysis is conducted using a mesh with 40 *cells/m* and $Re = 200$. The time step Δt is varied from 100 *s* to 4000 *s* and the mean drag coefficient C_d , maximum lift coefficient $C_{l,max}$ and root mean square of the lift coefficient $C_{l,rms}$ are monitored. The results are plotted in Figure 21 as a function of the ratio $T/\Delta t$. The vortex shedding period obtained numerically was $T = 35000$ *s* and the Strouhal number computed was $St = 0.14$.

As a rule of thumb, it is considered that $n = T/\Delta t$ should be greater than 25 to achieve convergence. From the data in Figure 21 it can be seen that for $T/\Delta t = 23$, compared to the case with the smallest time step, the relative error in the drag coefficient was 1%, while for the

maximum and root mean square of the lift coefficient the relative error was around 10%. For $T/\Delta t = 35$, the relative error in the drag coefficient drops to less than 1% and for the maximum and root mean square of the lift coefficient it drops to 3%. Thus, the rule of thumb can be used as an initial estimate to the time step size comfortably.

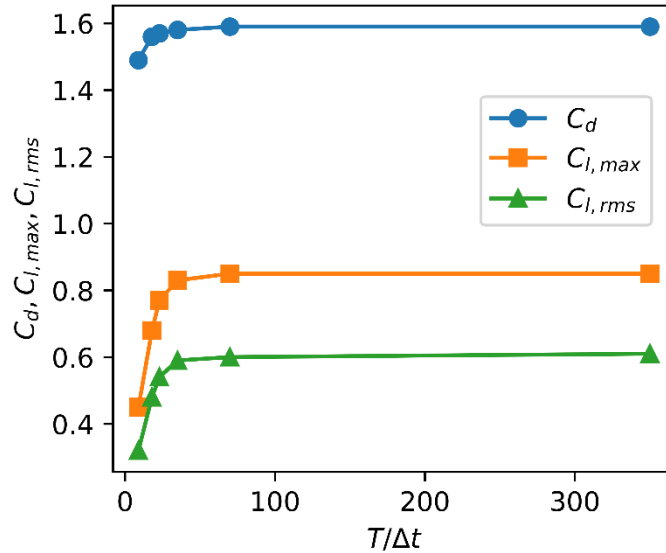


Figure 21 – Time step convergence for transient laminar flow over a square cylinder ($Re = 200$)

After checking for the domain, mesh and time step convergence, a verification study against data found in the literature is done with Reynolds varying from 50 to 200. The time step is estimated using equation (39) with $n = 35$ and $St = 0.14$. The mean drag coefficient obtained numerically is compared with the results by Franke et al. (1990), Jaiman et al. (2015), Sharma and Eswaran (2004), Shimizu and Tanida (1978) and Sohankar et al. (1999). The comparison is presented in Figure 22. Due to the transient nature of the problem, the results are more dispersed if compared to the steady-state case, Nonetheless, the C_d obtained with Fluet is in accordance with the results found in the literature.

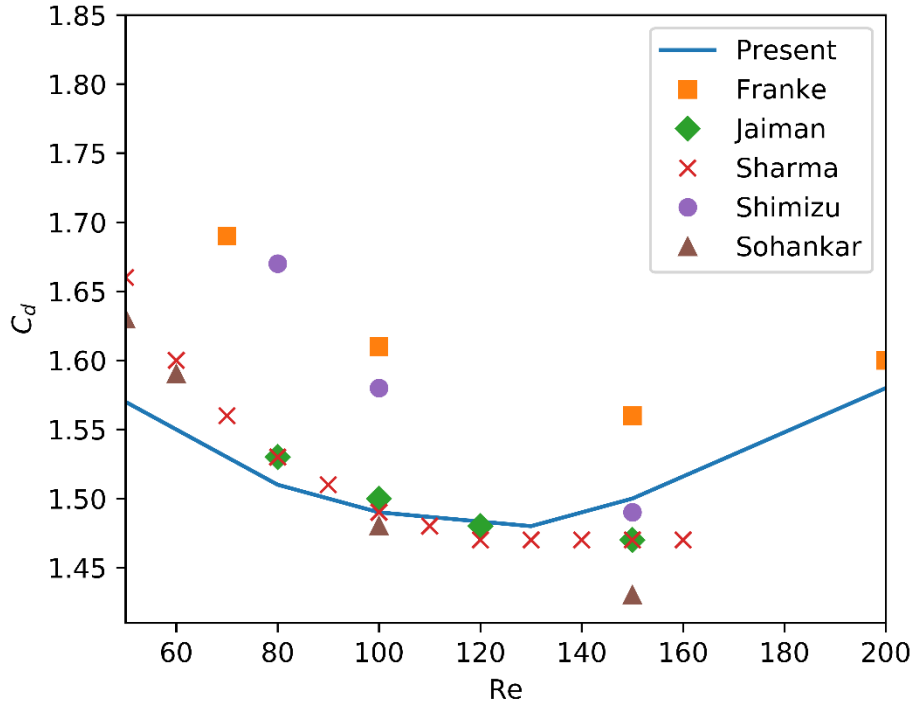


Figure 22 – Transient laminar flow over square cylinder verification

4.1.3. Transient Turbulent Flow

A transient turbulent flow is now modelled using the $k-\omega$ turbulence model. The results from the domain, mesh and time step convergence analyses performed on the transient laminar flow are used here. Using $Re = 22000$, the mean drag coefficient obtained was $C_d = 2.08$ and the Strouhal number was $St = 0.133$. These values are in accordance with the results obtained by Bosch (1996). Bosch numerical and experimental results for this case. Numerically, he obtained a drag coefficient $C_d = 2.108$ and Strouhal number $St = 0.146$. Experimentally, he found that the drag coefficient varied from 2.05 to 2.23 and the Strouhal number varied from 0.135 to 0.139. These results are shown in Table 3.

Table 3 – Transient turbulent flow over square cylinder results with $Re = 22000$

Present		Bosch (1996) - Numerical		Bosch (1996) - Experimental	
Cd	St	Cd	St	Cd	St
2.084	0.133	2.108	0.146	2.05-2.23	0.135-0.139

Figure 23 shows the streamlines coloured by the velocity magnitude. The figure clearly shows the formation of the von Karman vortex street on the back of the cylinder. It can also be seen that the velocity increases on the side of the cylinder, as predicted by the analytical solutions for the circular cylinder. These results give us confidence that the SST $k-\omega$ turbulence model is being properly used.

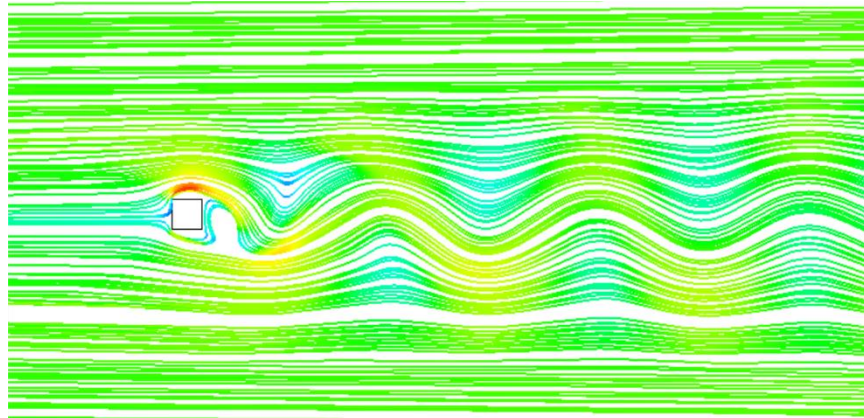


Figure 23 – Transient turbulent flow over square cylinder streamlines

4.2. Water Tap Flow Model

The first validation case for multiphase flow is to model the profile of a water stream falling from a tap. Due to continuity, the flow in any cross-section of the stream must be the same. However, as the water falls, it accelerates and gains speed. To maintain the same flow, the cross-sectional area must be reduced proportionally. Figure 24 illustrates this concept.

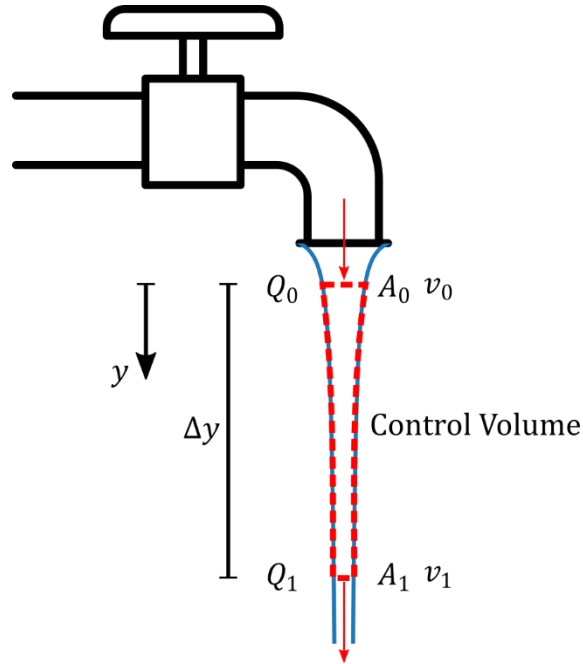


Figure 24 – Free fall water stream control volume

The analytical solution for the cross-sectional area A as a function of the fall distance y can be obtained by combining Torricelli's equation and the continuity equation. Applying the continuity equation in the control volume in Figure 24 we have that the flow entering the control volume must be equal to the flow exiting the control volume, that is

$$Q_1 = Q_0 \quad (40)$$

$$v_1 A_1 = v_0 A_0 \quad (41)$$

$$A_1 = \frac{v_0 A_0}{v_1} \quad (42)$$

where v_0 is the velocity at point 0, A_0 is the area at point 0, v_1 is the velocity at point 1 and A_1 is the area at point 1. Applying Torricelli's equation, we have

$$v_1^2 = v_0^2 + 2g\Delta y \quad (43)$$

$$v_1 = \sqrt{v_0^2 + 2g\Delta y} \quad (44)$$

where g is the gravitational acceleration and Δy is the distance between points 0 and 1. Substituting equation (44) into equation (42) we get

$$A_1 = \frac{v_0 A_0}{\sqrt{v_0^2 + 2g\Delta y}} \quad (45)$$

which can be generalized to

$$A(y) = \sqrt{\frac{v_0^2 A_0^2}{v_0^2 + 2gy}} \quad (46)$$

As mentioned before, the VOF method uses interpolation of the volume fractions in neighbouring cells to determine the profile of the interface. Thus, the smaller the cells are, the better the interpolation will be and the closer the computed interface profile will be to the real interface.

To test that, we modelled the water tap problem with three meshes. All the meshes were structured with all square elements. The first mesh had cells with 0.25 m sides (M0.25), the second had cells with 0.10 m sides (M0.10) and the third 0.05 m sides (M0.05). The meshes are named and are presented in Table 4. The flow had an initial area of 1 m^2 and an initial velocity of 1 m/s . Gravity was set to 10 m/s^2 . Because the problem is symmetric, only half of the geometry was modelled and a symmetry boundary condition was set at the plane of symmetry. The upper boundary was set as a mass flow inlet and the lower boundary was set as a pressure outlet at atmospheric pressure.

Table 4 - Meshes used for the water tap problem

Mesh Name	Cell Size (m)	Adaptative Iterations
M0.25	0.25	0
M0.10	0.10	0
M0.05	0.05	0
M0.25A2	0.25	2
M0.25A4	0.25	4
M0.10A2	0.10	2

Figure 25 shows the water volume fraction plots obtained with the three meshes. Only the regions with water volume fraction equal to or greater than 50% were plotted to make the visualization of the interface easier. Thus, regions with α_w greater than 50% were considered water and less than 50% were considered air. Figure 25 shows that as the mesh is refined, not only the interface profile gets smoother but also more information is preserved through the domain. In the coarsest mesh, as the water falls and the cross-section area decreases, the cells become too big to capture the water profile. As a result, the lower portion of the stream could be interpreted as containing only air, which makes no physical sense. On the other hand, the finest mesh has cells that are small enough to capture the water profile and preserve the expected interface.

By manually comparing the α_w values in equivalent cells on the three meshes, especially between M0.10 and M0.05, it was noted that cells with $\alpha_w = 1$ and $\alpha_w = 0$ were consistent across different meshes. That is, if a cell was completely filled with water in a coarser mesh it would also be completely filled with water in a finer mesh. The same goes for cells completely filled with air. The differences in water volume fraction would only show up in the cells with α_w between 0 and 1, that is, in the interface. This motivated us to try to refine the mesh only along the interface.

To study the influence of the refinement along the interface, three other meshes were generated using a mesh adaptation strategy. The adaptation strategy consists in running an initial simulation using a coarse mesh, then, based on the volume fractions obtained, the cells containing the air-water interface are refined and another simulation is run with the adapted mesh. Multiple iterations of the adaptation process can be run to obtain a mesh that is well refined along the interface and coarser everywhere else. Figure 26 shows the two iterations of the adaptation strategy used on mesh M0.25 to obtain mesh M0.25A2. Appendix B shows how to use mesh adaptation on Fluent.

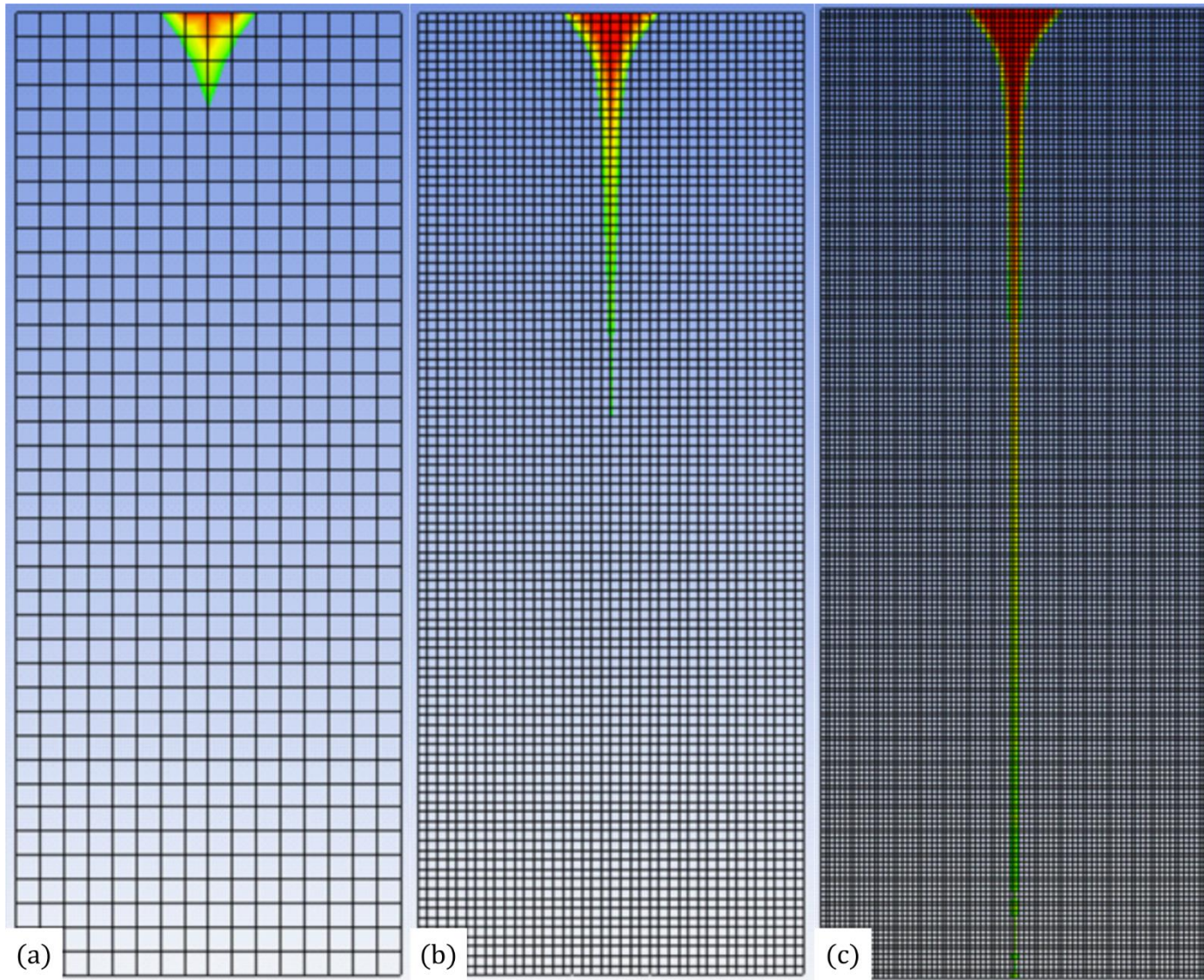


Figure 25 – Free fall water stream profile with three meshes (a) M0.25, (b) M 0.10, (c) M0.05

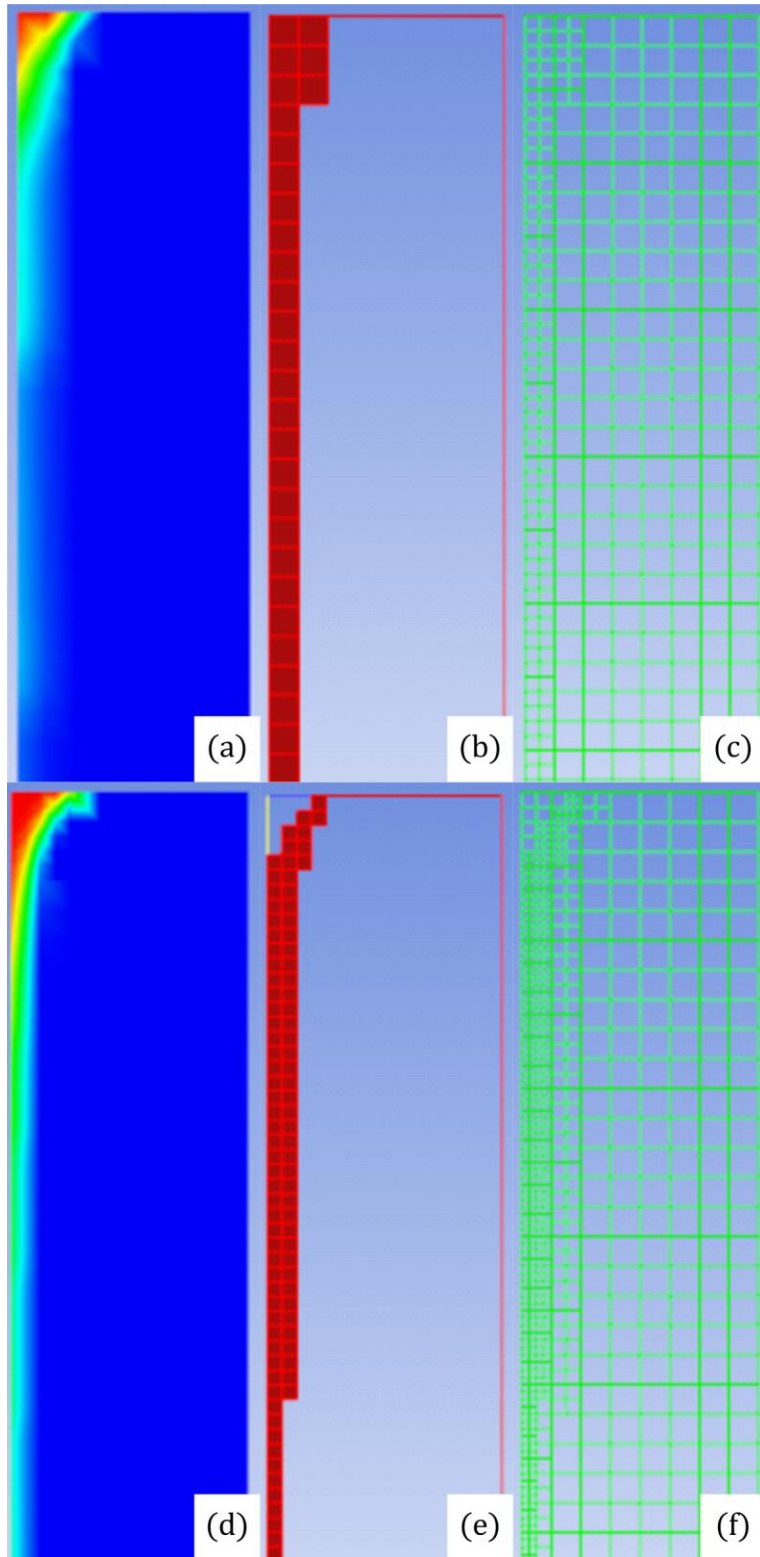


Figure 26 – Mesh adaptation - First iteration (a) volume fraction, (b) adapted cells, (c) resulting mesh. Second iteration (d) volume fraction, (e) adapted cells, (f) resulting mesh

To evaluate the convergence of the solution, the mass residual ε_m is computed using equation (47), where S is the cross section. The results for each mesh are plotted in Figure 27. This figure clearly shows that the number of cells along the interface is strongly related to the convergence of the solution.

$$\varepsilon_m = 1 - \frac{\int_S \alpha_w \rho dS}{\int A(y) \rho dy} \quad (47)$$

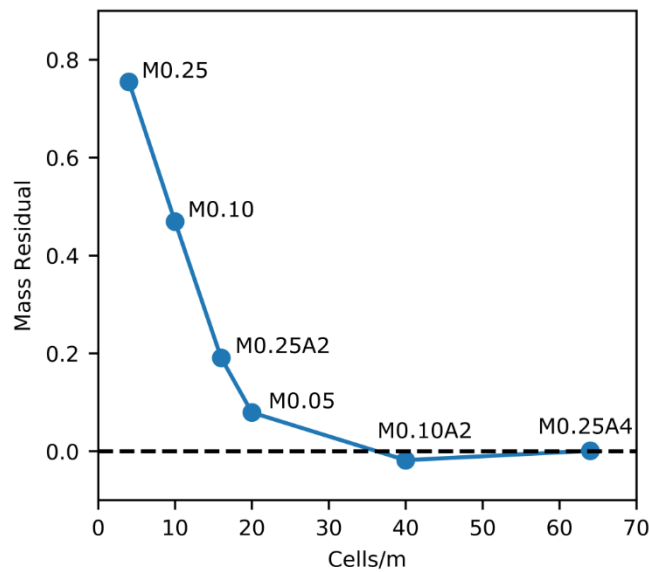


Figure 27 – Mass residual obtained using different meshes

Figure 28 shows the comparison between the numerical solutions obtained with the six meshes described in Table 4 and the analytical solution from equation (46). This figure shows that the coarsest mesh is far from representing the profile accurately. However, after some adaptation iterations, even the coarsest mesh is able to yield good results. Thus, the refinement along the interface is what really matters for computing the profile accurately. The adaptation mesh refinement can significantly affect the water profile obtained numerically without increasing the total number of cells nearly as much as refining the entire domain. Some refinement along the air-water interface is needed to represent the water profile correctly.

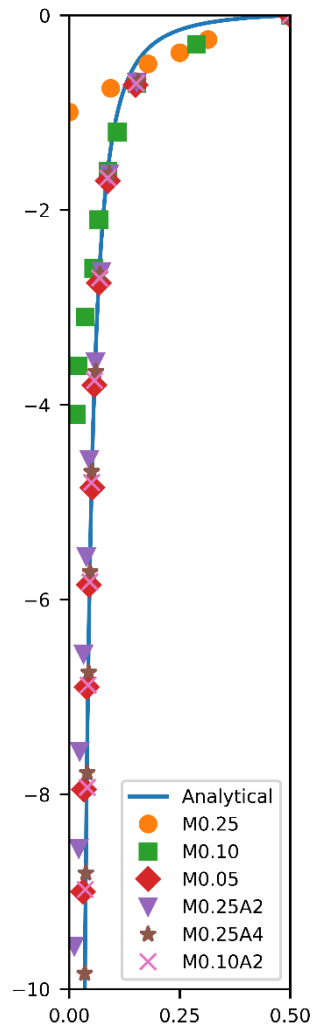


Figure 28 – Free fall water stream profile comparison between analytical and numerical solutions

This adaptation strategy proved to be very efficient, as it allows the use of a coarse mesh in regions of minor interest to the study, such as the layer of air, reducing the total number of cells and saving significant computational time. Mesh adaptation is used in all following numerical models when an improvement in the volume fractions resolution is needed.

4.3. Flow Over Ogee Spillway

A standard ogee spillway, often called WES spillway, described in USACE (1970) is studied herein to validate the CFD model for overtopped structures and find an appropriate mesh size to be used in the next simulations. The standard spillway profile is defined by a collection of curves and is designed to follow the natural profile of the water nappe such that pressure along the spillway crest is zero when the overtopping water head, H_0 , is equal to the design water head, H_d . The United States Army Corps of Engineers (USACE) defines the geometry of the WES spillway as shown in Figure 29.

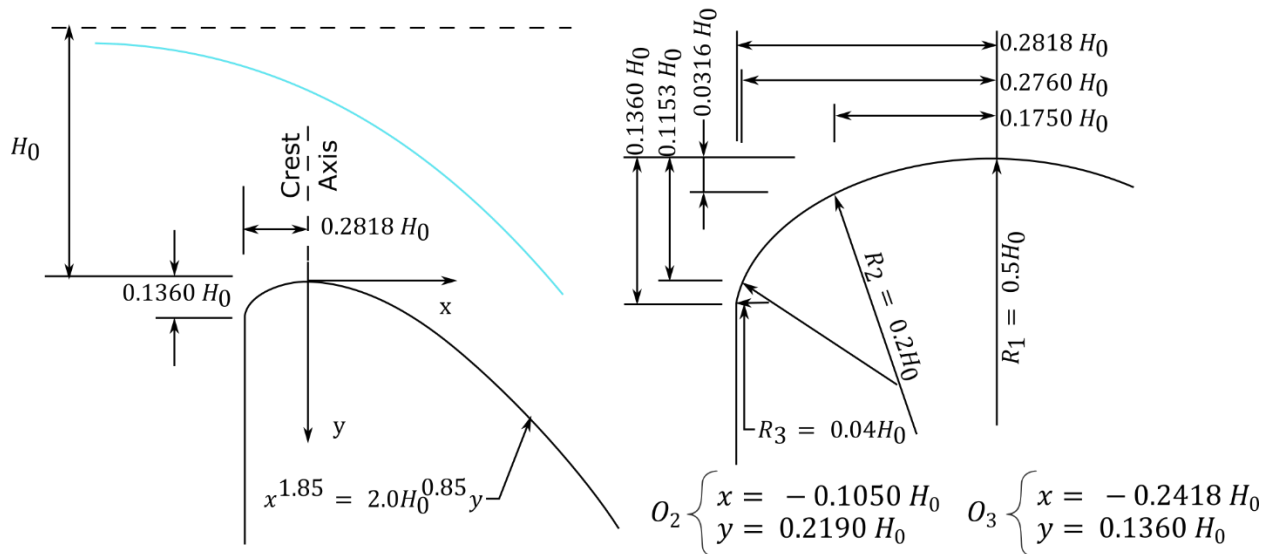


Figure 29 – WES spillway geometry definition (Instituto da Água, 2001)

Numerical modelling of the standard spillway with a total height $H = 5 \text{ m}$ and design water head $H_d = 1 \text{ m}$ is performed using four different meshes with cell sizes of 0.125 m (M0.125), 0.10 m (M0.10), 0.05 m (M0.05) and 0.02 m (M0.02). The computational model used is shown in Figure 30. Gravity acceleration was set to 9.81 m/s^2 and the water surface tension is set to 0.072 N/m . The reference atmospheric pressure was set to 0 Pa to facilitate post processing. Air density is set to 1.225 kg/m^3 and air viscosity is set to $1.79 \cdot 10^{-5} \text{ kg/m.s}$. Water density is set to

998.2 kg/m^3 and water viscosity is set to $1.003 \cdot 10^{-3} \text{ kg/m.s}$. These values are also used on all other models going forward.

The upstream boundary is set as a mass flow inlet, and the downstream and upper boundaries are set as pressure outlets. The boundaries corresponding to the floor and structure are set as no-slip walls. In addition, the open channel option present in Fluent is enabled. This option allows the specification of the inlet water level. Fluent then computes the related inlet pressure. With this option enabled, the pressure in the outlets can be determined (i) by specifying the tailwater level, (ii) by interpolation from the neighbouring cells, or (iii) by specifying a gauge pressure. On the downstream boundary, the pressure is computed from the neighbouring cells; on the upper boundary, it is set to the atmospheric pressure.

The problem is initialized with water filling the upstream side of the structure up to the crest level. The rest of the domain is filled with air. Variable time stepping is used so that the Courant number does not exceed 1, ensuring convergence.

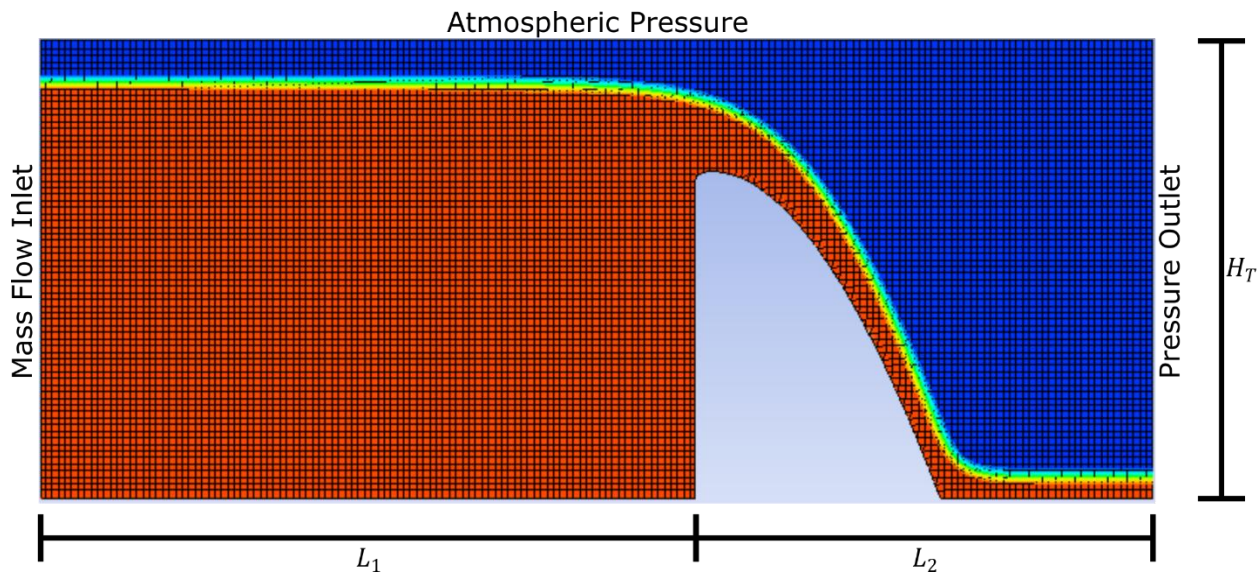


Figure 30 – Ogee spillway computational model

Initially, the dimensions L_1 , L_2 and H_T are set to 20 m , 15 m and 7 m , respectively. The overtopping height H_0 was set to 1.33 m , that is $H_0 = 1.33H_d$. Using these dimensions and

overtopping height, a mesh convergence analysis is done. Simulations are run for all four meshes until steady state is achieved. The resulting horizontal force R_x and resulting vertical force R_y on the spillway are evaluated and plotted in Figure 31. The results are plotted as a ratio between the resulting force obtained with a given mesh and the one obtained with the finest mesh (M0.02).

Figure 31 shows that the horizontal force does not vary much among the different meshes. The vertical forces, however, vary more significantly. In spite of that, the difference between the finest and coarsest mesh is lower than 10%. On the other hand, the computational time increases by many orders of magnitude as the mesh is refined. Thus, we chose to use the mesh M0.10 (10 cells per metre) as it provides relatively accurate results within a reasonable computational time.

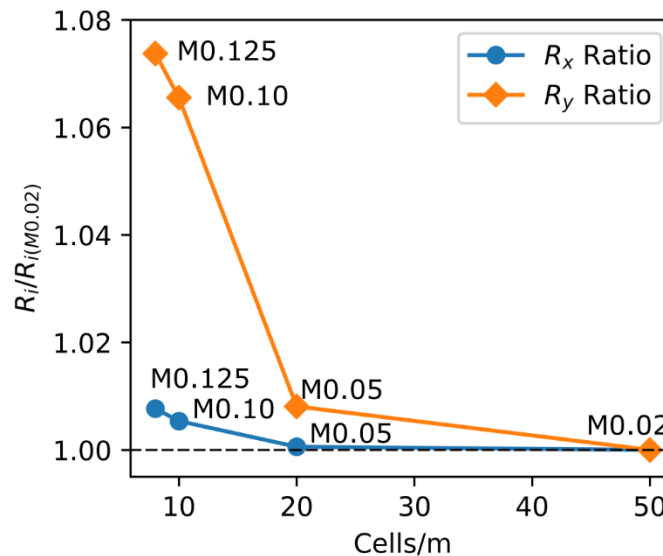


Figure 31 – Mesh convergence analysis for standard ogee spillway

After defining that mesh M0.10 is the most appropriate for this work, the influence of the domain dimensions was studied. First, the dimensions L_2 and H_T were fixed at 15 m and 7 m, respectively. Then, horizontal (R_x) and vertical (R_y) resultant forces were evaluated for L_1 equals to 40 m, 20 m, 10 m, 5 m and 2 m. The results were plotted in Figure 32a as a ratio of the results for a given L_1 compared to the result for $L_1 = 40$ m. It can be seen that for L_1 larger or equal to 5 m, the resultants vary less than 3%. However, for $L_1 = 2$ m, the vertical resultant diverges

completely, indicating that the inlet boundary is too close to the structure and is now affecting the pressure field on the structure. Thus, a minimum of 5 m should be used for L_1 .

Next, L_1 and H_T were fixed at 5 m and 7 m, respectively. Then, R_x and R_y were evaluated for L_2 equals to 15 m, 7 m, 5 m and 4.5 m. The results were plotted in Figure 32b as a ratio of the results for a given L_2 compared to the result for $L_2 = 15$ m. It can be seen that for L_2 larger or equal to 5 m, the results vary less than 2%. However, for $L_2 = 4.5$ m, the results diverge, indicating that the outlet boundary is too close to the structure and is affecting the pressure fields on the structure. Thus, a minimum of 5 m should be used for L_2 .

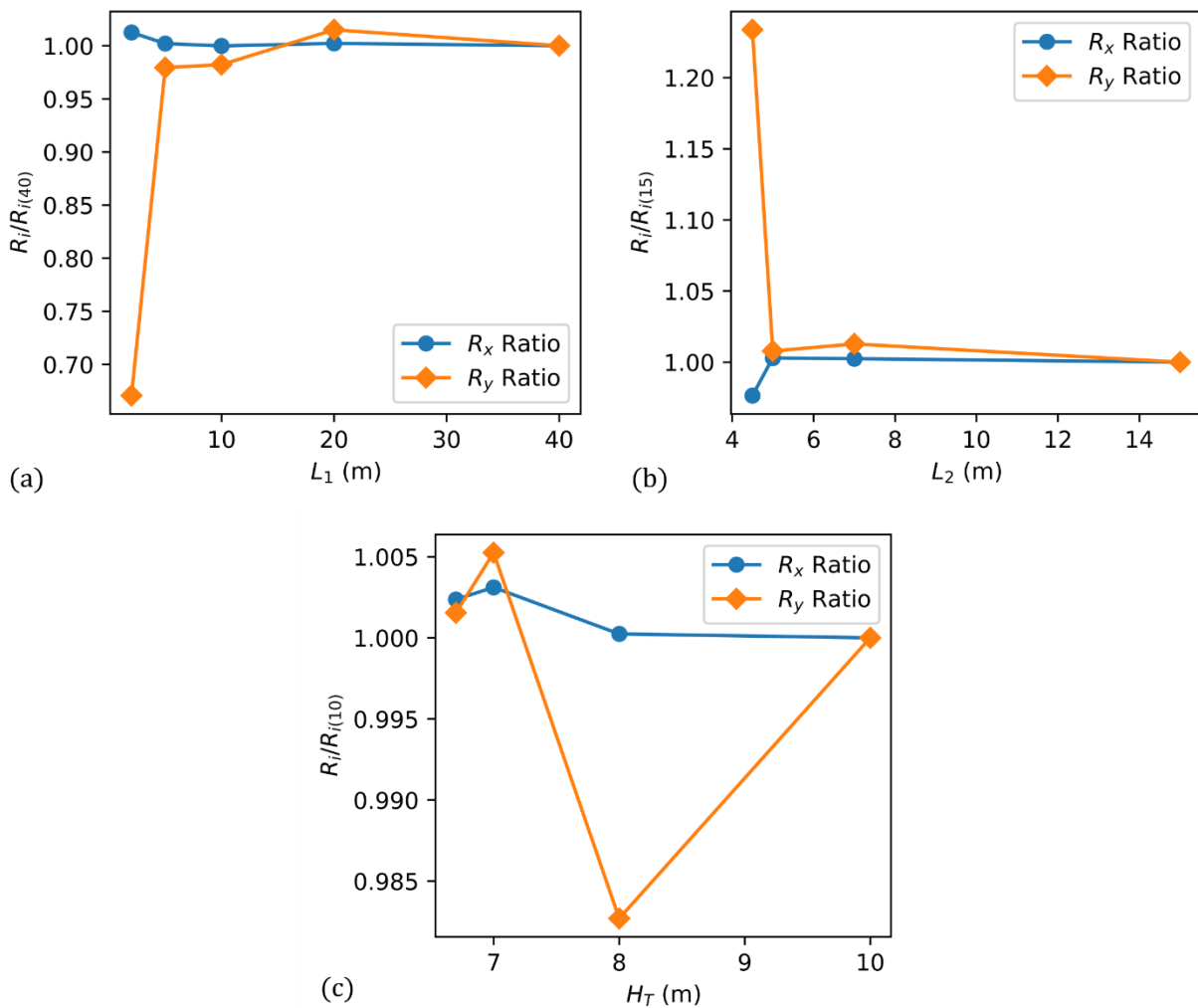


Figure 32 – Domain convergence analysis for standard ogee spillway: (a) upstream length L_1 , (b) downstream length L_2 , (c) domain height H_T

Finally, L_1 and L_2 were fixed at 5 m each while H_T assumed the values 10 m, 8 m, 7 m, 6.7 m and 6.5 m. The results were plotted in Figure 32c as a ratio of the results for a given H_T compared to the result for $H_T = 10$ m. It can be seen that all results plotted in Figure 32c (from 6.7 m to 10 m) were within 2% difference. However, the simulation with $H_T = 6.5$ m diverged due to numerical errors and was not completed. Thus, a minimum of 6.7 m should be used for H_T to ensure numerical convergence.

After obtaining these results, some manual verifications of the flow conditions for each case were done. It was noted that three conditions are necessary to achieve convergence of the results: (i) the upstream length L_1 has to be big enough to contain a section where the flow is uniform; (ii) the downstream length L_2 has to be big enough so that the turbulent region is within the domain and uniform flow is developed again; (iii) the total domain height H_T has to be big enough to contain at least a thin layer of air above the water. If the three conditions are met, increasing the domain dimensions does not improve results and only increase computational cost.

After doing mesh and domain convergence, the profile of the water nappe above the spillway was obtained numerically with $L_1 = 10$ m, $L_2 = 7$ m and $H_T = 7$ m for $H_0 = 1.33$ m. The results obtained with each mesh are compared to the profile provided by USACE (1970) in Figure 33. All meshes were capable of representing the water profile very well, with no significant difference between them. This, once again, confirms that mesh M0.10 is adequate for the simulations.

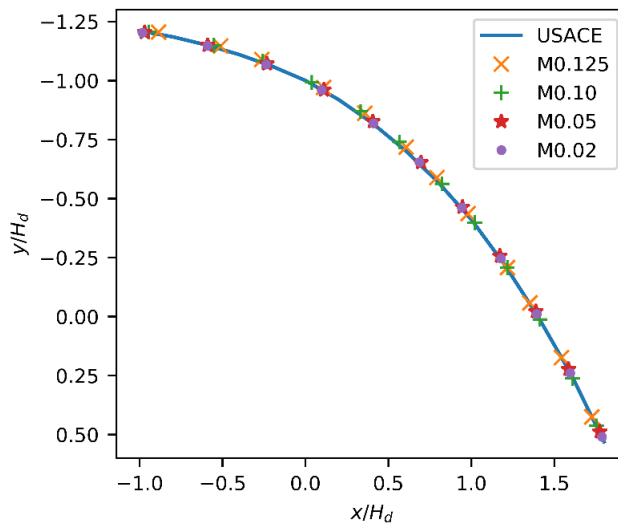


Figure 33 – Water nappe profile over ogee spillway with $H_0 = 1.33H_d$

Using mesh M0.10, the pressure on the spillway crest is evaluated for $H_0 = 0.50 m$, $H_0 = 1.00 m$ and $H_0 = 1.33 m$. The results are plotted and compared with pressures provided in USACE (1970) as the reference solution in Figure 34. CFD simulations were able to represent the pressure field on the crest with adequate accuracy compared to the reference solution, especially for the case with positive pressures ($H_0 = 0.5 m$), which is the scenario the is found the most in this work. It is also important to notice that the case with negative pressures is also very important for the study of cavitation, which this computational model could be used for.

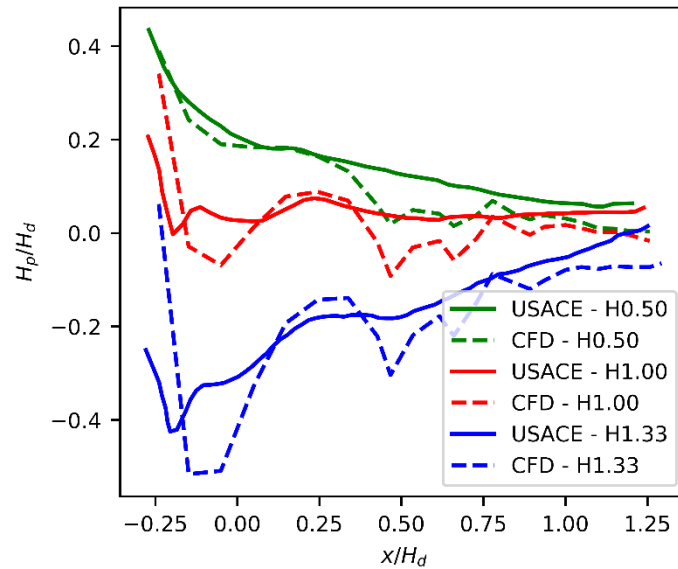


Figure 34 – Pressure field comparison between CFD and USACE (1970) for the flow over ogee spillway with $H_0 = 0.50H_d$, $H_0 = 1.00H_d$ and $H_0 = 1.33H_d$

Thus, in CFD simulations in the following sections of this work, a 0.10 m cell size is used. Moreover, the mesh adaptation strategy is applied when needed, as this provides good accuracy with reasonable computational time.

4.4. Flow Over Broad-Crested Weir

In this section, the flow over a broad-crested weir is studied to compare two aeration strategies: (i) using a 2D model with a small pressure outlet in the downstream wall of the weir, which allows

air to come from the outlet to maintain atmospheric pressure below the overflowing nappe, as proposed by Hargreaves et al. (2007), and (ii) using a 3D model with a broadening of the domain on the downstream side that allows the air to penetrate from the sides, as presented by Favre and Léger (2018). This problem is very similar to the flow over the rectangular crest of gravity dams and over the slab of an existing spillway presented next in this work.

The weir modelled herein is the one presented by Hager and Schwalt (1994). They conducted an experimental study on a small-scale channel that was 0.5 m wide, 7.0 m long and 0.7 m high. The weir was 0.4 m high and 0.5 m long. They ran their experiment with multiple overtopping heights H_0 and obtained dimensionless flow profiles, pressure fields on the crest and boundary separation curves, among other results. The numerical results obtained with both aeration strategies are compared to the experimental results obtained by Hager and Schwalt (1994). Figure 35 shows the computational models used on both aeration strategies. The 3D model has a symmetry plane perpendicular to the z axis. Thus, only half of the geometry is modelled and a symmetry boundary condition is applied to the symmetry plane in order to reduce the computational cost. This strategy is adopted in all 3D models presented in this work because all of them have symmetry planes.

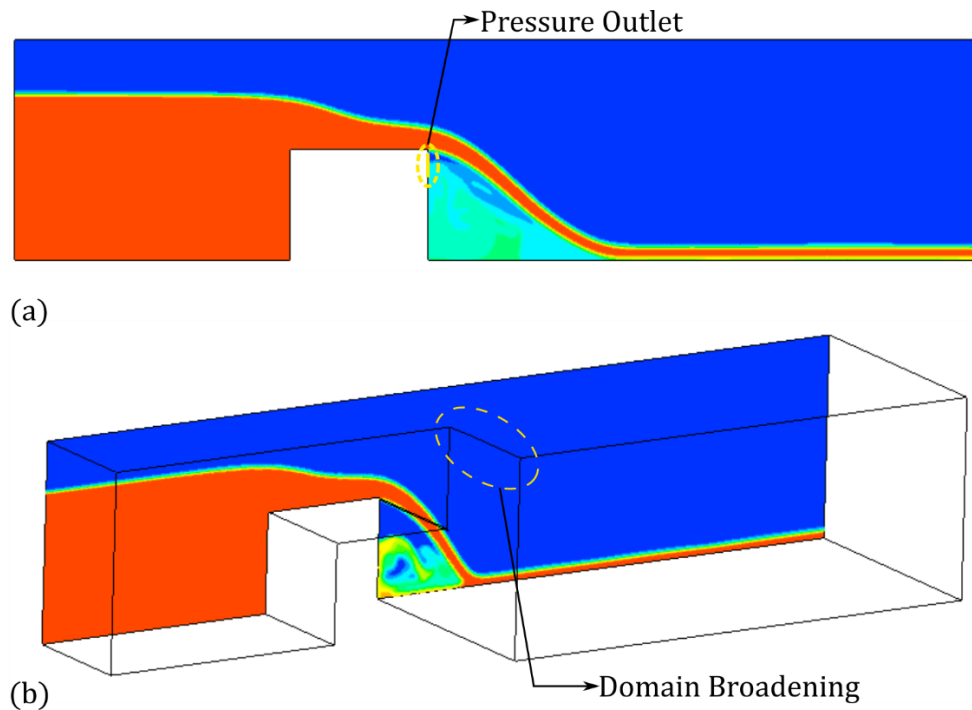


Figure 35 – Broad crested weir computer models: (a) 2D model with aeration outlet and (b) 3D model with domain broadening

The computational models studied here are run using a flow of $68.07 \cdot 10^{-3} \text{ m}^3/\text{s}$, which led to an overtopping height of 0.200 m . This corresponds to the run with the highest flow in Hager and Schwalt's experiment, which, in their case, led to an overtopping height of 0.205 m .

Figure 36 shows the water profile obtained with the 2D and 3D models compared to the result obtained by Hager and Schwalt (1994). Overall, both profiles are very similar to the experimental results, with the 2D model being slightly more accurate on the downstream side.

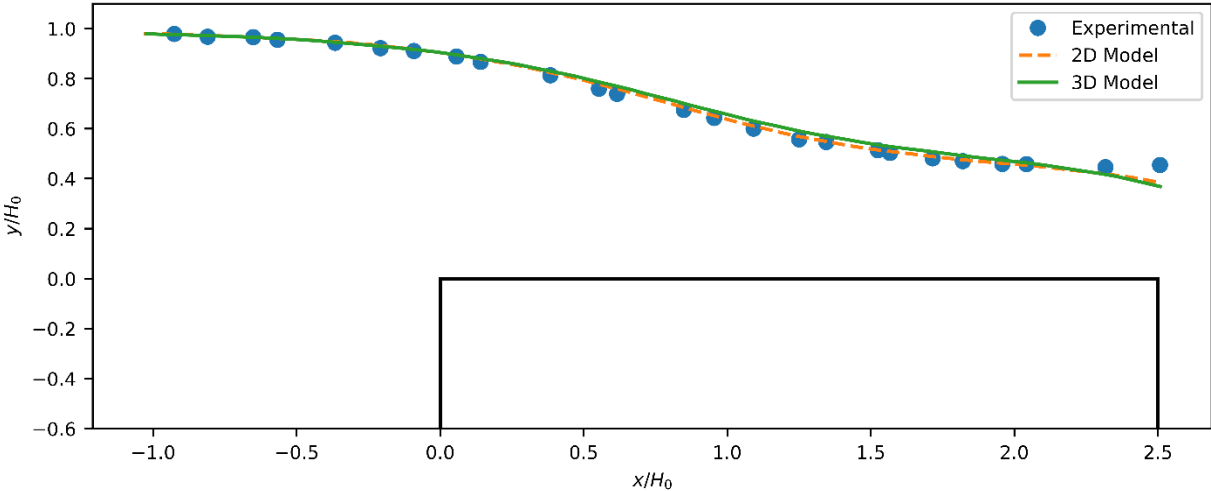


Figure 36 – Dimensionless water profile over a broad-crested weir

The dimensionless pressure field over the crest is presented in Figure 37. Again, both models are very close to the experimental results, with the 3D model being more accurate in the middle section and the 2D model is more accurate at the upstream and downstream ends.

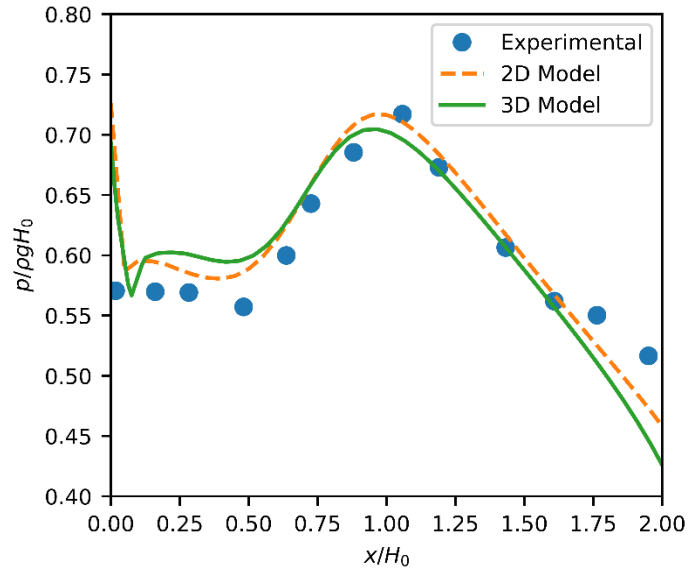


Figure 37 – Dimensionless pressure field over a broad-crested weir

Figure 38 shows that the flow separation due to the upstream weir corner computed from CFD is about the same as that obtained experimentally. Figure 38 also shows the streamlines for the 2D model. The streamlines for the 3D model are nearly identical to those of the 2D model.

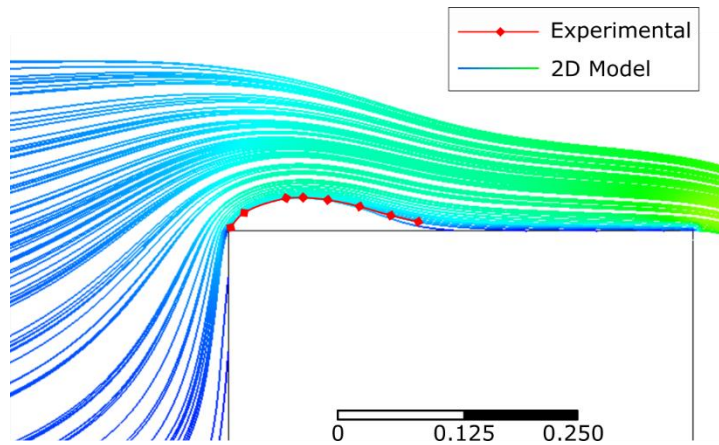


Figure 38 – Numerical streamlines compared to experimental boundary separation curve

These results show that both aeration strategies yield very similar, accurate results. The 2D model with a small pressure outlet on the downstream wall of the weir has a much lower computational cost and is more convenient to use in simple flow problems similar to this experiment. However,

this approach requires prior knowledge of a section in the domain that will not contain any water. The 3D model with domain broadening, on the other hand, can be applied in any situation and may be required if the engineer does not know whether the flow will have full aeration. For this reason, the 3D model approach is used in all the following modelling and simulation. Moreover, from Figure 35, it can be seen that the volume fractions are much more well defined in the 3D model, despite both models using the same cell sizes. This indicates that the 3D strategy is better suited to represent the tailwater condition.

After completing all validation cases and obtaining results that were in agreement with analytical and experimental results, we were confident that the computational models used in this work were capable of simulating well the overtopping of dams and spillways. Therefore, the hydrodynamic forces computed with the simulations can be used for stability analysis.

5. OVERTOPPING OF RECTANGULAR CREST

In this chapter, the flow of a rectangular crest is modelled to study the vertical force due to overtopping. The vertical force obtained from CFD is compared with an estimation found in FERC (1991) and an improvement to this estimation is suggested.

5.1. Rectangular Crest Analyzed

The overtopping of rectangular sections is now considered to represent the crest of a gravity dam and to study several essential aspects of related CFD models. Figure 39 shows the computational model used in this section. To quantify the overtopping pressure acting on gravity dam rectangular crests, three CFD models are developed with a 5 m height and width B varying among 2.5 m, 3.75 m and 5 m. These models are similar to the broad crest weir validation example and use the same 3D modelling strategy with broadening of the downstream domain for aeration. The scale of the model, however, is closer to the standard ogee spillway studied previously. Thus, a mesh with a cell size of 0.1 m (M0.10) is used. Three overtopping levels H_0 are modelled for each crest length. Using the computed CFD pressures, the resultant vertical force magnitude and position are evaluated. The results are summarized in Table 5.

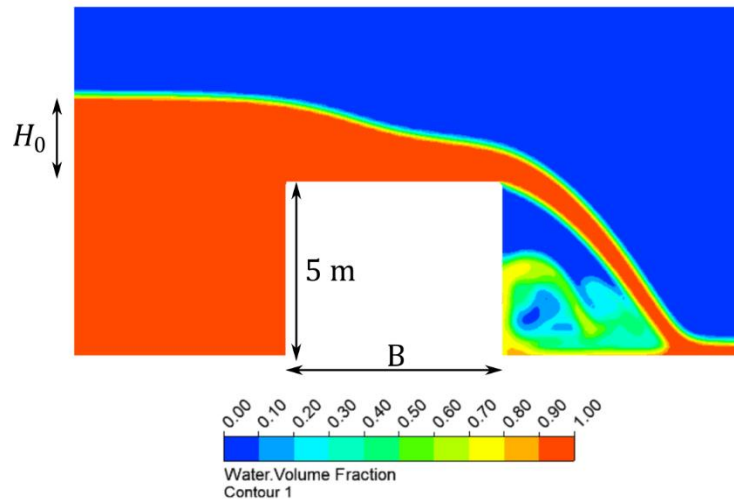


Figure 39 – Numerical model used for evaluation of vertical forces on a rectangular crest

5.2. CFD Comparison with Dam Safety Guidelines

In dam stability assessment, water pressures on gravity dam crests are usually neglected because of their small magnitude for small overtopping heights (USACE 1995, FERC 2016). This assumption is conservative due to the stabilizing effect of the positive vertical pressure on the crest, as shown in Figure 12. A common rule of thumb used to estimate the overtopping pressure is shown in Figure 40 (FERC, 1991 Appendix - sample calculation of overtopped gravity dam). The pressure field is estimated to be trapezoidal. The magnitude of the upstream pressure is taken as $\alpha \rho g H_0$, while the downstream pressure is $\beta \rho g H_0$. Usually, the coefficients α and β are considered equal to 1.0 and 0.5, respectively. However, this rule of thumb is not supported by experimentation or numerical analysis. The literature does not provide simplified practical guidelines that have been validated or verified to account for the fluid flow pressures on overtopped rectangular crests, which are typical of gravity dams; this shortfall has motivated the present study.

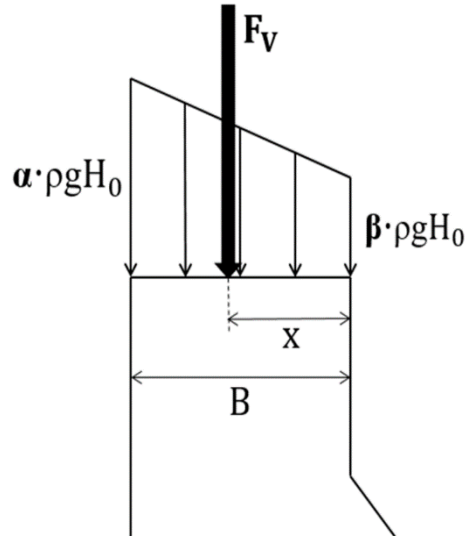


Figure 40 – Simplified pressure field on crest subject to overtopping

Using the trapezoidal pressure field hypothesis, the resultant vertical force on the crest F_v and its position x are given by:

$$F_v = 0.5(\alpha + \beta)\rho g B H_0 \quad (48)$$

$$x = \frac{\alpha + 2\beta}{3(\alpha + \beta)} B \quad (49)$$

The vertical forces on the crest are computed using CFD (F_v^{CFD}) and using the rule of thumb with $\alpha = 1.0$ and $\beta = 0.5$ ($F_v^{\alpha=1.0, \beta=0.5}$), and with $\alpha = 2/3$ and $\beta = 1/3$ ($F_v^{\alpha=2/3, \beta=1/3}$), which are presented in Table 5. The coefficients α_{CFD} and β_{CFD} and the position x/B_{CFD} that result in equivalent force and moment for each CFD simulation are also indicated in Table 5. The coefficients α_{CFD} and β_{CFD} are obtained by calculating the equivalent trapezoidal pressure field that results in the same vertical force on the crest magnitude F_v^{CFD} and position x/B_{CFD} as the CFD pressure field.

The position of the resultant force obtained with the rule of thumb with both sets of coefficients is always equal to $x = 0.56B$. The rule of thumb estimates the position of F_v^{CFD} with a high level of accuracy, but the force magnitude using $\alpha = 1.0$ and $\beta = 0.5$ is overestimated by an average of 43%. This leads to an overestimation of the structure stability (sliding and overturning) because

the force on the crest is a stabilizing force. On the other hand, the use of $\alpha = 2/3$ and $\beta = 1/3$ estimates the vertical force on the crest with much better accuracy, underestimating it by only 5% on average. The average equivalent coefficients α_{CFD} and β_{CFD} obtained with CFD are 0.69 and 0.36, respectively. These values were then approximated by $\alpha = 2/3$ and $\beta = 1/3$ for practical use. Figure 41 shows that the pressure field estimated by the rule of thumb with $\alpha = 1.0$ and $\beta = 0.5$ is an overestimated envelope of the pressure field obtained with CFD while the one obtained with $\alpha = 2/3$ and $\beta = 1/3$ seems to estimate the pressure more accurately. The CFD curve in this figure was obtained for $H_0 = 1.84 \text{ m}$ and $B = 5.0 \text{ m}$.

Table 5 - Crest pressure coefficients obtained from CFD

$B \text{ (m)}$	$Q \text{ (m}^3\text{/s)}$	$H_0 \text{ (m)}$	$F_v^{CFD} \text{ (kN)}$	$F_v^{\alpha=2/3, \beta=1/3} \text{ (kN)}$	$F_v^{\alpha=1.0, \beta=0.5} \text{ (kN)}$	x/B_{CFD}	α_{CFD}	β_{CFD}
2.50	0.84	0.65	8.55 (1.00)	7.96 (0.93)	11.93 (1.40)	0.57	0.78	0.30
	2.40	1.22	16.40 (1.00)	14.93 (0.91)	22.40 (1.37)	0.55	0.71	0.39
	3.91	1.78	22.30 (1.00)	21.79 (0.98)	32.68 (1.47)	0.52	0.58	0.45
3.75	0.85	0.60	10.61 (1.00)	11.02 (1.04)	16.52 (1.56)	0.56	0.66	0.30
	2.71	1.47	29.30 (1.00)	26.99 (0.92)	40.49 (1.38)	0.56	0.73	0.36
	3.61	1.79	37.07 (1.00)	32.87 (0.89)	49.30 (1.33)	0.54	0.71	0.42
5.00	0.84	0.58	13.87 (1.00)	14.20 (1.02)	21.30 (1.54)	0.55	0.64	0.34
	2.60	1.45	37.01 (1.00)	35.50 (0.96)	53.25 (1.44)	0.57	0.73	0.32
	3.71	1.84	48.53 (1.00)	45.04 (0.93)	67.57 (1.39)	0.56	0.72	0.35

Note: Values in parenthesis represent the ratio between the vertical forces obtained using the simplified method and CFD, taken as reference.

For both $\alpha = 1.0, \beta = 0.5$ and $\alpha = 2/3, \beta = 1/3$, the value of x/B_{CFD} is always 0.56.

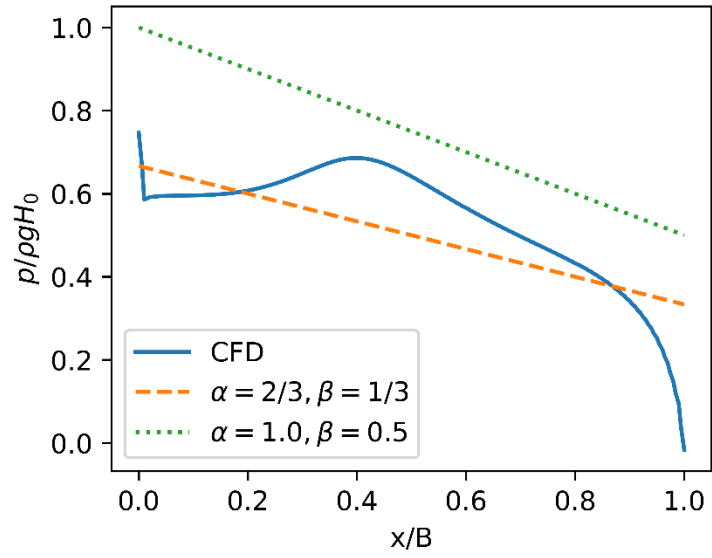


Figure 41 – Comparison between pressure field using CFD and simplified method with $\alpha=1.0$ and $\beta=0.5$, and with $\alpha=2/3$ and $\beta=1/3$

6. STABILITY OF OVERTOPPED GRAVITY DAMS

In the next sections, existing structures are analyzed for different overtopping conditions. CFD models are used to compute hydrodynamic pressure fields acting on all wetted surfaces. These pressure fields are then integrated to compute resultant forces. Those forces are input into the concrete dam structural stability computer program CADAM3D with assumed dam-foundation interface uplift pressures. Based on the safety factors obtained and guideline recommendations, the stability of the structures is assessed. This methodology is presented in Figure 5.

6.1. Gravity Dam Analyzed

A gravity dam section with a height of 7.62 m was adapted from an existing structure to represent a small dam. This dam is characterized by a vertical upstream face, a rectangular crest, and a downstream face with a constant slope. Figure 42a shows a typical cross section for this kind of dam, and the forces involved in an overtopping situation. Figure 42b shows the computational model and a representation of the pressure fields obtained with CFD.

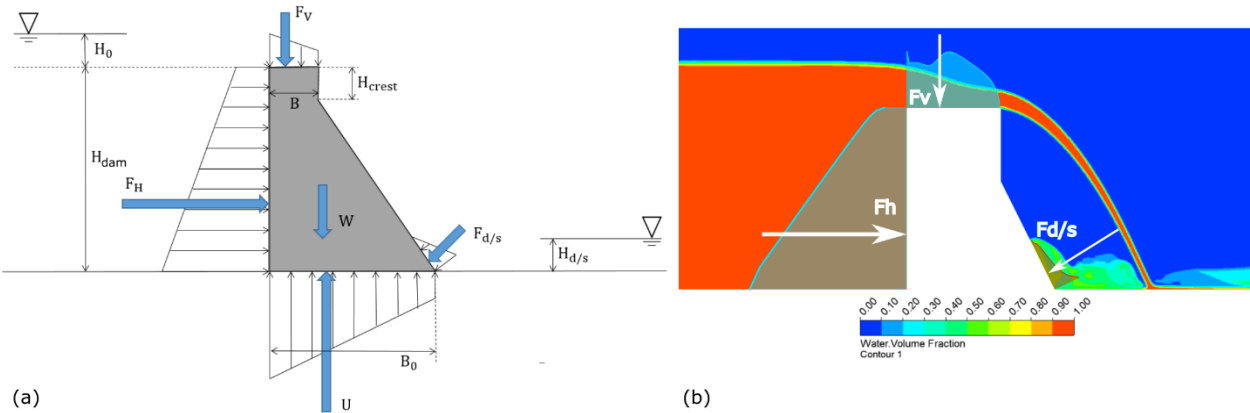


Figure 42 – Pressure fields and forces obtained from (a) safety guideline and (b) CFD

6.2. Stability Analysis with Gravity Method

The gravity method is the classical method used for performing stability analyses of gravity dams. This method uses the equilibrium of rigid bodies to determine the internal forces acting on the potential failure planes (lift joints and concrete-rock interface) and uses beam theory to compute stresses. The method is based on the following hypotheses:

- Concrete is homogeneous, isotropic and uniformly elastic;
- All loads are carried by gravity action of vertical parallel-sided cantilevers with no mutual support between adjacent cantilevers;
- No differential movements effects on the dam or foundation occur as a result of the water load from the reservoir;
- The dam is analyzed as a cantilever beam with unitary thickness;
- The normal stresses in horizontal planes vary linearly;
- The shear stresses in horizontal planes vary parabolically.

In general, this method yields very good results, except in horizontal planes next to the base due to foundation strain effects that are not considered by the method (Ribeiro, 2006).

The stability of the dam is evaluated in terms of three safety factors: the overturning safety factor (OSF), the sliding safety factor (SSF) and the uplift safety factor (USF). The OSF is defined as the ratio between the sum of the stabilizing moments $\sum M_{+ve}$ and destabilizing moments $\sum M_{-ve}$, that is:

$$OSF = \frac{\sum M_{+ve}}{\sum M_{-ve}} \quad (50)$$

The horizontal component of the upstream hydrostatic pressure, silt, ice and uplift pressure contribute to the destabilizing moment while the dam self-weight, downstream hydrostatic pressure and overtopping pressure contribute to the stabilizing moment. Vertical components of hydrostatic pressures both upstream and downstream also contribute towards the stabilizing moment. Seismic loads are not considered in the OSF due to its random oscillatory nature.

The SSF is defined as the ratio between the sum of the stabilizing cohesion and frictional forces and the destabilizing horizontal forces. Thus, the SSF is computed as

$$SSF = \frac{(\sum \bar{V} - U)\tan\phi + cA_c}{\sum H} \quad (51)$$

where $\sum \bar{V}$ is the sum of the vertical forces except for the uplift, U is the uplift force, ϕ is the friction angle in the dam-foundation interface, c is the cohesion, A_c is the area of the interface under compression and $\sum H$ is the sum of horizontal forces. It is important to notice that only the portion of the interface that is under compression contributes to cohesion. Any area of the interface in tension does not contribute to cohesion. The dam self-weight and the overtopping pressure contribute towards the stabilizing vertical forces alongside with vertical components of silt and hydrostatic forces. The horizontal components of the upstream and downstream hydrostatic forces contribute towards the horizontal forces. However, the downstream portion is stabilizing and, thus, should contribute negatively to $\sum H$.

Finally, the USF is defined as the ratio between the sum of the stabilizing vertical forces and the sum of the destabilizing vertical forces. It can be computed as

$$USF = \frac{\sum \bar{V}}{U} \quad (52)$$

The dam self-weight, the overtopping pressure and the vertical components of hydrostatic forces contribute towards the stabilizing vertical forces while the uplift pressure contributes towards the destabilizing vertical forces.

The gravity method also provides a simple way to calculate the stresses on the dam. Novak et al. (2007) present the following equations to estimate these stresses. The normal stress on a horizontal plane σ_z is given by:

$$\sigma_z = \frac{\sum V}{A_h} \pm \frac{\sum M y'}{J} \quad (53)$$

where $\sum V$ is the sum of all vertical forces, A_h is the area of the horizontal surface, M is the bending moment, y' is the distance from the point of analysis to the neutral axis and J is the moment of

inertia of the section. This expression can be rewritten for the normal stress on the upstream face σ_{zu} and on the downstream face σ_{zd} as:

$$\sigma_{zu} = \frac{\Sigma V}{B_0} \left(1 - \frac{6e}{B_0}\right) \quad (54)$$

$$\sigma_{zd} = \frac{\Sigma V}{B_0} \left(1 + \frac{6e}{B_0}\right) \quad (55)$$

where e is the moment excentricity given by

$$e = \Sigma M / \Sigma \bar{V} \quad (56)$$

The sum of the moments ΣM in the eccentricity calculation is taken from the centroid of the section.

The shear stress on the upstream face τ_u and on the downstream face τ_d are a function of the angle between the vertical and the upstream face slope ϕ_u or the downstream face slope ϕ_d , as follows:

$$\tau_u = (p_w - \sigma_{zu}) \tan(\phi_u) \quad (57)$$

$$\tau_d = \sigma_{zd} \tan(\phi_d) \quad (58)$$

where p_w is the external hydrostatic pressure. The normal stresses on vertical planes σ_y can be determined by considering that the difference in the shear forces above and bellow of a certain element is balanced by σ_y . Thus, it can be deduced that the normal stresses on vertical planes on the upstream face σ_{yu} and on the downstream face σ_{yd} are as follows:

$$\sigma_{yu} = p_w + (\sigma_{zu} - p_w) \tan^2(\phi_u) \quad (59)$$

$$\sigma_{yd} = \sigma_{zd} \tan^2(\phi_u) \quad (60)$$

The maximum and minimum normal stresses σ_1 and σ_3 and the maximum shear stress τ_{max} can be obtained by the Mohr's circle theory as

$$\sigma_1 = \frac{\sigma_z + \sigma_y}{2} + \tau_{max} \quad (61)$$

$$\sigma_3 = \frac{\sigma_z + \sigma_y}{2} - \tau_{max} \quad (62)$$

$$\tau_{max} = \sqrt{\left(\frac{\sigma_z - \sigma_y}{2}\right)^2 + \tau^2} \quad (63)$$

6.3. Stability Criteria

The stability of dams and spillways are generally assessed in terms of the position of the resultant (which is a measure of the OSF), normal and shear stresses, and the SSF. For global stability, guidelines such as FERC (2016), CDA (2013), and USACE (1995) recommend that the resultant position shall be within the middle third of the structure base for usual load cases. For unusual and extreme load cases, it may be outside of the middle third and within the base as long as the other performance indicators satisfy acceptance criteria. This ensures that the structure will not fail by overturning.

The compressive stress should not exceed 30% of the compressive strength f'_c in usual loading cases and 50% of f'_c in unusual and extreme loading cases. For design, tensile strength is usually considered zero unless material tests are conducted. However, Lo and Grass (1994) show that small but significant amounts of tensile strength exist in many dams along the contact with the foundation. The shear stresses are usually considered uniformly distributed over the compressed zone and shall be within the available shear strength that could be mobilized.

The SSF acceptance criteria are dependent on the considerations of friction and cohesion. If only friction is considered, then the SSF must be equal to or higher than 1.5 for usual cases, 1.3 for unusual cases and 1.1 for flood cases (CDA 2013). However, if cohesion is also considered and no tests are available, then the acceptance criteria increase to 3.0 for usual cases, 2.0 for unusual cases and 1.3 for flood cases.

The structural stability analyses for all the dams and loading cases are performed by the gravity method using the computer program CADAM3D. The hydrodynamic pressure fields are initially obtained either from CFD using ANSYS-Fluent or dam safety guidelines. All stability computations are performed considering a concrete volumetric mass of 2400 kg/m³. The SSF is

evaluated from a cracked base analysis, at the dam-foundation interface, assuming at first that the tensile strength and cohesion are zero.

In some stability calculations performed herein, a small amount of tensile strength and cohesion have to be considered to meet the SSF acceptance criterion (minimum of 1.3). Tensile strength is needed to control the crack initiation and propagation, which in turn, prevents an increase in uplift pressures. Moreover, from our tests we noticed that small overtopped gravity structures exhibit highly brittle behaviour. As soon as a crack initiates, it propagates through the entire section, leading to failure.

Lo and Grass (1994) evaluated, from in situ testing, the rock-concrete tensile strength, f_t , in multiple dams in Ontario, Canada. The average tensile strength along the contact between rock and concrete in existing dams was found to be 1.08 MPa with a minimum of 0.18 MPa. EPRI (1992) also presented data indicating that for the peak shear strength in concrete-granite-gneiss foundations, the best-fit cohesion c is 1.30 MPa, the friction angle ϕ is 57° and the tensile strength f_t is 0.83 MPa. The lower bound cohesion is 0.48 MPa, the friction angle is 57° , and the tensile strength is 0.31 MPa. Based on these data, we used a peak friction angle $\phi = 55^\circ$ and computed the required tensile strength and cohesion to meet stability criteria, while staying within the plausible range presented by these authors. The structure-foundation interface is considered bonded, initially uncracked, and it is assumed that no sliding occurs.

Figure 43 shows comparisons among three different models to estimate the available shear strength along the concrete-rock joint. The expected real behaviour of a bounded interface includes a small tensile and shear resistance as well as real cohesion, c . Some shear resistance can be developed even in tension. However, the model adopted in this work neglects any shear resistance in tension and only fully mobilizes cohesion when a threshold compressive stress, σ_n , is applied.

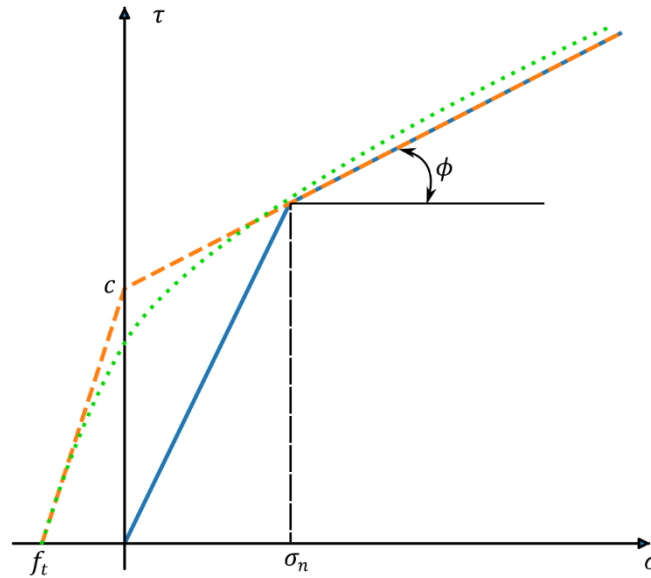


Figure 43 – Shear and tensile strength of concrete-rock joint

6.4. Hydrostatic and Hydrodynamic Pressures

The stability of dams and spillways is addressed in many guidelines, such as FERC (2016), CDA (2013) and USACE (1995). These guidelines suggest that the pressure on the upstream wall can be considered hydrostatic. The force and its position on the crest can be estimated as shown in Equations (48) and (49). The pressure on the downstream face can be estimated by assuming that the tailwater level $H_{d/s}$ is equal to H_0 if the tailwater condition significantly reduces or eliminates the hydraulic jump, or $0.6H_0$ otherwise. The amount of reduction in the effective tailwater depth may vary according to the degree of submergence of the crest of the structure and the backwater conditions in the downstream channel (USACE 1995). Thus, it is expected that the downstream force computed from CFD might be larger than that estimated by the guidelines. The forces on the upstream and downstream faces can be obtained by integrating the hydrostatic pressures on the wetted surfaces. To compute the uplift pressure, however, the tailwater level is always considered equal to H_0 .

The stability of the gravity dam in Figure 42 is analyzed for a case without tailwater. The upstream and crest forces are evaluated using CFD simulations and guideline recommendations. Table 6 shows that the horizontal forces on the upstream face were almost identical between CFD and guideline values. Figure 42b shows that the pressure field on this face is almost hydrostatic and has a nearly trapezoidal shape. The vertical forces on the crest are overestimated by the guidelines by approximately 40% when using $\alpha = 1.0$ and $\beta = 0.5$. This result is consistent with what was found for the rectangular crest. It reinforces the importance of adopting $\alpha = 2/3$ and $\beta = 1/3$ instead of the usual values of $\alpha = 1.0$ and $\beta = 0.5$ in the simplified analysis.

Table 6 also presents discharge coefficients C_D obtained from CFD, which were computed from:

$$C_D = \frac{Q}{LH_0^{3/2}} \quad (64)$$

where L is the dam width, assumed as 1 m, and Q is the water inflow. The results were compared with the experimental values presented by the French Ministry of Agriculture (1977) for a sharp rectangular crest. The difference between the experimental and numerical results is no more than 6%, again validating the CFD model.

Table 6 - Dam stability without tailwater

Dam height H_{dam} (m)		7.62	
Dam base width B_0 (m)		6.25	
Crest height H_{crest} (m)		3.05	
Crest width B (m)		3.96	
Inflow rate Q (m^3/s)	1	2	4
Overtopping height H_0 (m)	0.78	1.24	1.9
Inlet velocity v (m/s)	0.12	0.23	0.42
Discharge coefficient C_D^{CFD} - reference	1.45 (1.00)	1.45 (1.00)	1.53 (1.00)
Discharge coefficient C_D^{theory}	1.43 (0.99)	1.44 (0.99)	1.44 (0.94)
Upstream pressure head - $U_{u/s}^{CFD}$ (m) - reference	8.12 (1.00)	8.59 (1.00)	9.25 (1.00)
Upstream pressure head - $U_{u/s}^{static}$ (m)	8.40 (1.03)	8.86 (1.03)	9.52 (1.03)
Horizontal force upstream - F_h^{CFD} (kN) - reference	341.7 (1.00)	376.2 (1.00)	424.5 (1.00)
Hydrostatic force upstream - F_h^{static} (kN)	342.5 (1.00)	376.8 (1.00)	426.1 (1.00)
Vertical force on crest - F_v^{CFD} (kN) - reference	15.9 (1.00)	25.5 (1.00)	37.7 (1.00)
Vertical force on crest - $F_v^{\alpha=2/3, \beta=1/3}$ (kN)	15.1 (0.95)	24.0 (0.94)	36.8 (0.98)
Vertical force on crest - $F_v^{\alpha=1.0, \beta=0.5}$ (kN)	22.7 (1.42)	36.1 (1.41)	55.3 (1.47)
SSF F_v^{CFD} - reference	2.47 (1.00)	2.09 (1.00)	1.48 (1.00)
SSF $F_v = 0$	2.40 (0.97)	1.86 (0.89)	1.09 (0.73)
SSF $F_v^{\alpha=2/3, \beta=1/3}$	2.46 (0.99)	2.06 (0.99)	1.45 (0.98)
SSF $F_v^{\alpha=1.0, \beta=0.5}$	2.49 (1.01)	2.16 (1.03)	1.61 (1.09)
Note: Values in parenthesis represent the ratio between parameter values computed using the simplified method and CFD, taken as reference.			

Now, the same gravity dam is analyzed for a case with tailwater. Table 7 presents the downstream pressure head at the toe of the dam $H_{d/s}$ and the downstream force $F_{d/s}$. The CFD pressure at the dam toe is significantly smaller than the uplift pressure recommended in the guidelines. On the other hand, the CFD downstream force is considerably larger than guideline recommendations, especially when using a tailwater level of $0.6H_0$. These can be explained by the high turbulence level and significant downstream velocities.

Table 7 - Dam stability with tailwater

Inflow rate Q (m^3/s)	1	2	4
Overtopping height H_0 (m)	0.78	1.24	1.9
Downstream pressure head - $U_{d/s}^{CFD}$ (m) - reference	0.67 (1.00)	0.76 (1.00)	0.76 (1.00)
Downstream pressure head - $U_{d/s}^{1.0H_0}$ (m)	0.78 (1.17)	1.24 (1.64)	1.90 (2.50)
Downstream force - $F_{d/s}^{CFD}$ (kN) - reference	5.8 (1.00)	11.4 (1.00)	20.0 (1.00)
Downstream force - $F_{d/s}^{1.0H_0}$ (kN)	3.3 (0.57)	8.4 (0.74)	19.8 (0.99)
Downstream force - $F_{d/s}^{0.6H_0}$ (kN)	1.2 (0.21)	3.0 (0.27)	7.1 (0.36)
SSF - $F_{d/s}^{0.6H_0}, U_{d/s}^{1.0H_0}, F_v^{\alpha=2/3, \beta=1/3}$ - reference	2.37 (1.00)	1.96 (1.00)	1.38 (1.00)
SSF - $F_{d/s}^{0.6H_0}, U_{d/s}^{1.0H_0}, F_v = 0$	2.31 (0.97)	1.77 (0.90)	1.07 (0.78)
SSF - $F_{d/s}^{0.6H_0}, U_{d/s}^{1.0H_0}, F_v^{\alpha=1.0, \beta=0.5}$	2.40 (1.01)	2.05 (1.05)	1.53 (1.11)
SSF - $F_{d/s}^{0.6H_0}, U_{d/s}^{1.0H_0}, F_v^{CFD}$	2.38 (1.00)	1.98 (1.01)	1.41 (1.02)
SSF - $F_{d/s}^{1.0H_0}, U_{d/s}^{1.0H_0}, F_v^{\alpha=2/3, \beta=1/3}$	2.39 (1.01)	1.99 (1.02)	1.45 (1.05)
SSF - $F_{d/s}^{CFD}, U_{d/s}^{1.0H_0}, F_v^{CFD}$	2.42 (1.02)	2.04 (1.04)	1.47 (1.07)
SSF - $F_{d/s}^{CFD}, U_{d/s}^{CFD}, F_v^{CFD}$	2.44 (1.03)	2.08 (1.06)	1.54 (1.12)

Note: Downstream pressure head and downstream force values in parenthesis represent the ratio between parameter values computed using the simplified method and CFD, taken as reference.

Sliding Safety Factor (SSF) values in parenthesis represent the ratio between the parameter values and those using downstream force $F_{d/s}^{0.6H_0}$, downstream uplift pressure $U_{d/s}^{1.0H_0}$ and vertical force on the crest $F_v^{\alpha=2/3, \beta=1/3}$, taken as reference.

6.5. Safety Factors

The SSF is first calculated for the case without tailwater. This can be interpreted as a local analysis of a lift joint at a higher elevation than the base in a larger dam. In this case, only the horizontal force upstream and vertical force on the crest are present, while the downstream force is zero. The uplift pressure field is triangular. It is assumed to be equal to the hydrostatic pressure due to an overtopping of H_0 metres on the upstream side and zero on the downstream side. The SSF obtained using CFD forces are compared with three cases (Table 6): (i) one in which the vertical force on the crest is considered zero, which is recommended in guidelines as being on the safe side, (ii) one in which the vertical force is estimated using the trapezoidal distribution with $\alpha = 2/3$ and $\beta = 1/3$, (iii) and one in which the vertical force is estimated using $\alpha = 1.0$ and $\beta = 0.5$. For the

smallest overtopping height, the SSF obtained from the different hypotheses were very close to the SSF obtained from CFD forces. This is because the crest vertical force is almost negligible compared to the dam weight. However, as the overtopping height H_0 increases, the difference between the SSF from CFD forces and those from different hypotheses increases. For 1.9 m of overtopping, compared to the SSF obtained from CFD, it is shown that (i) considering $F_v = 0$ underestimates the SSF by 27%, (ii) using $\alpha = 1.0$ and $\beta = 0.5$ overestimates the SSF by 9%, and (iii) using $\alpha = 2/3$ and $\beta = 1/3$ yields the best approximation, with only 2% underestimation.

The SSF is also evaluated for a case with tailwater. Multiple hypotheses for the tailwater level, downstream uplift pressure and vertical force on the crest are analyzed. We selected for reference the one we considered as the most appropriate simplified estimation with (i) the crest vertical force estimated from $\alpha = 2/3$ and $\beta = 1/3$, (ii) the downstream force computed with $0.6H_0$ tailwater, and (iii) the downstream uplift pressure estimated with a tailwater of $1.0H_0$. These hypotheses can be applied in practical stability evaluation without the need for CFD, while still yielding comparable results. Table 7 shows that the difference in the SSF between assuming $0.6H_0$ or $1.0H_0$ for the tailwater level is only 5% in the case with an overtopping height H_0 of 1.9 m. This is because the downstream force is relatively small compared to all other forces involved to maintain equilibrium. Thus, both hypotheses can be used interchangeably without a significant impact on the SSF. For an overtopping height H_0 of 1.9 m, assuming $F_v = 0$ underestimates the SSF by 22%, and using $\alpha = 1.0$ and $\beta = 0.5$ overestimates the SSF by 11%. Table 7 also presents a load case for which the downstream force, F_v , and downstream uplift pressure are all taken from CFD. The SSF using these hypotheses is 9% larger than the SSF obtained from the reference case with $H_0 = 1.9$ m.

Although the CFD model has been validated for overtopping, taking the uplift pressure from CFD is not recommended, because the model does not simulate the underground flow, and the high level of downstream turbulence can affect the pressure significantly.

7. CASE STUDY: EXISTING GATED SPILLWAY

One of the main advantages of CFD is that it can model overtopping flow on structures with complex geometries to obtain the corresponding pressure fields and perform structural stability assessments. The simplified procedures proposed herein for gravity dams with typical cross sections may not always be applicable to more complex geometries. The purpose of this section is to model the overtopping responses of an existing spillway with complex geometry while using CFD results to perform the stability assessment.

7.1. Spillway Description

In 1996, a major flood occurred in the Saguenay region (Québec, Canada). The rain-induced flow was much greater than the spillway capacity of the several gravity structures located in this area. During this flood, the gravity dams and spillways were subjected to intense hydrodynamic loading conditions, which resulted in overtopping of more than 2 *m* in some cases (Léger et al. 1998). One of the structures affected by this flood was the Chute Garneau spillway, which is studied herein. This spillway is made of a series of piers that support a concrete bridge.

The same methodology used to study the stability of a gravity dam is used to study the Chute Garneau spillway. This is a small spillway that is 6.30 *m* high from the bottom to the top of the slab. Figure 44a shows the plan view, and Figure 44b shows the elevation of one section of this structure.

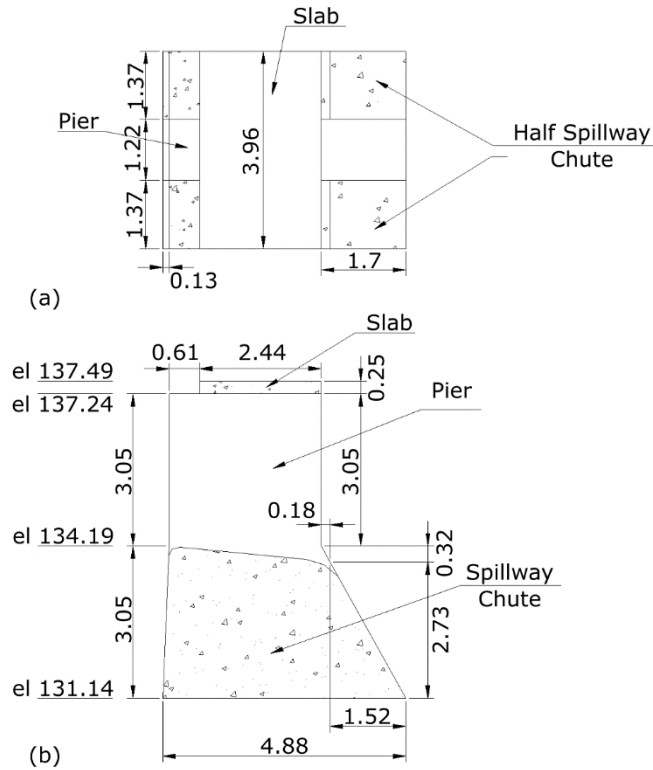


Figure 44 – Chute Garneau blueprints: (a) plan view and (b) elevation dimensions

Figure 2 shows a photo of the spillway during the flood. Despite considerable overtopping, the structure resisted the flood, and its hydroelectric powerplant was later rehabilitated. During the event, there was a notable accumulation of floating debris.

7.2. CFD Structural Modeling and Simulation

Considering the geometry of the spillway shown in Figure 44, a 3D symmetrical CFD model was developed to analyze the stability of this structure during the flood. The CFD model is limited to one section with a symmetry plane across one of the piers, as presented in Figure 45, with no normal flow along the lateral boundaries. Figure 46a,b shows the profile and the water volume fractions on a cross-section at the middle of the spillway chute and at the middle of the pier,

respectively. Figure 46c,d show the velocity contour plots at the middle of the spillway chute and at the middle of the pier, respectively, while Figure 46e,f show the pressure contour plots in the same sections. All these results correspond to an overtopping height of 2.16 m.

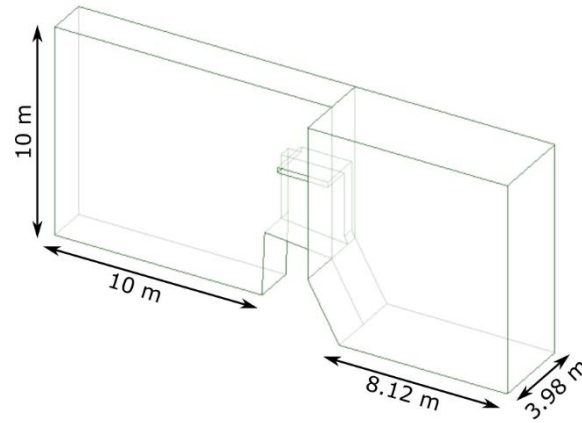


Figure 45 – Chute Garneau geometric model used on CFD simulations

From Figure 46c, it can be seen that the velocity of the flow between the piers and under the slab significantly increases due to a jet effect. This effect creates a small negative pressure on the spillway crest, as noted in Figure 46e. Full aeration was only obtained in the areas under the slab and downstream of the pier. The region downstream of the spillway chute was not fully aerated. The water volume fraction is approximately 0.75, indicating partial aeration. This is only possible because the domain was broadened to allow for aeration.

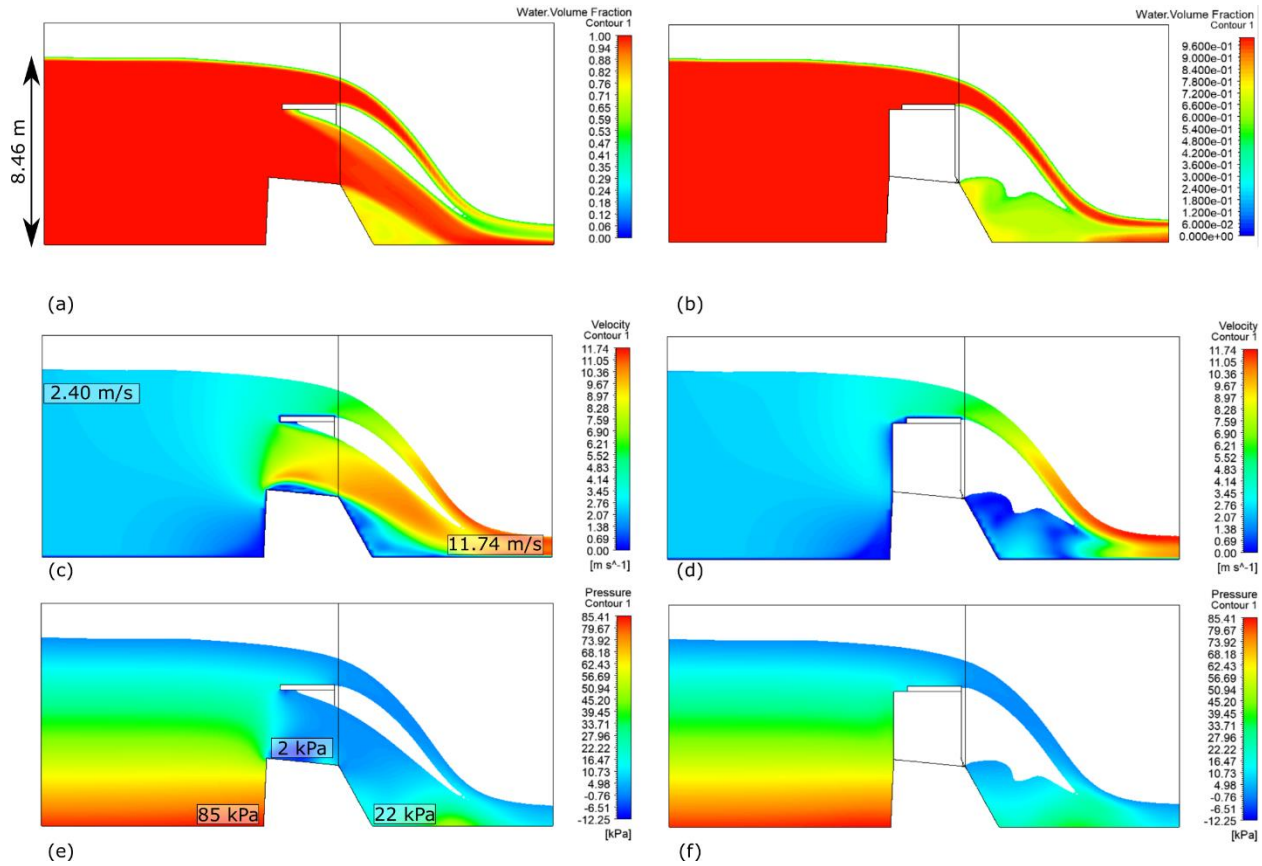


Figure 46 – Chute Garneau spillway CFD model for $H_0 = 2.16\text{ m}$: water volume fraction at (a) spillway section and (b) pier section, velocity contours at (c) spillway section and (d) pier section, pressure contours at (e) spillway section and (f) pier section

7.3. Parametric Analysis

The Chute Garneau spillway stability is evaluated under multiple scenarios, such as (i) with the gates completely opened, (ii) completely closed, and (iii) partially closed. Table 8 summarizes the stability assessment with opened gates such that they do not interfere with the flow. The CFD stability indicators are calculated using the forces and uplift pressure obtained using CFD. The stability indicators for $\alpha = 1.0$ and $\beta = 0.5$, and $\alpha = 2/3$ and $\beta = 1/3$ are obtained using the proposed estimation, except for the uplift pressure, which is taken from CFD. This is because the

flow condition differs significantly from the overtopping of a gravity dam with classical geometry, increasing the uplift pressure significantly.

Table 8 - Chute Garneau stability with opened gates

H_0 (m)	σ_t (kPa)	c (kPa)	Sliding Safety Factor			Resultant Position in %**		
			F_v^{CFD} - Reference	$F_v^{\alpha=2/3, \beta=1/3}$	$F_v^{\alpha=1.0, \beta=0.5}$	F_v^{CFD} - Reference	$F_v^{\alpha=2/3, \beta=1/3}$	$F_v^{\alpha=1.0, \beta=0.5}$
0*	0	0	2.78 (1.00)	2.74 (0.99)	2.91 (1.05)	57 (1.00)	57 (1.00)	56 (0.98)
		50	3.35 (1.00)	3.30 (0.99)	3.51 (1.05)			
1.10	33.7	0	1.34 (1.00)	1.45 (1.08)	1.64 (1.23)	83 (1.00)	78 (0.94)	72 (0.88)
		50	1.64 (1.00)	1.77 (1.08)	1.98 (1.21)			
1.45	48.1	0	1.15 (1.00)	1.31 (1.14)	1.51 (1.32)	82 (1.00)	83 (1.01)	76 (0.83)
		50	1.44 (1.00)	1.62 (1.13)	1.84 (1.28)			
1.80	56.9	0	1.13 (1.00)	1.19 (1.05)	1.38 (1.22)	95 (1.00)	87 (0.92)	80 (0.83)
		50	1.43 (1.00)	1.48 (1.03)	1.69 (1.18)			
2.16	68.8	0	0.96 (1.00)	1.09 (1.14)	1.29 (1.34)	105 (1.00)	93 (0.89)	83 (0.79)
		50	1.24 (1.00)	1.37 (1.10)	1.58 (1.28)			

Note: The values in parenthesis represent the ratio between stability indicators using simplified method and CFD, taken as reference.

* Normal operating level with no overtopping and total water height equals to 5.38 m.

** Expressed in percentage of base width from upstream.

The values of $\alpha = 1.0$ and $\beta = 0.5$ once again overestimate the sliding safety factors, this time, by as much as 34%. The proposed $\alpha = 2/3$ and $\beta = 1/3$ values also overestimate the sliding safety factors in some cases, but only by 14% when $H_0 = 2.16$ m. To demonstrate stability, a small amount of rock-concrete tensile strength (up to 70 kPa) must be considered to avoid cracking. Otherwise, the structure fails by overturning. Moreover, a small amount of cohesion (up to 50 kPa) is needed to achieve the minimum safety factor of 1.3 recommended by CDA (2013) in case of a flood. The spillway is expected to exhibit a very brittle failure mechanism because it relies on the tensile strength to keep the structure stable. If a small amount of tensile strength cannot be mobilized, the structure would suddenly crack, the uplift pressure will increase, and the structure would fail. Both the 70 kPa of rock-concrete tensile strength and 50 kPa of cohesion assumed in the model are within the lower bound limits presented by Lo and Grass (1994) and EPRI (1992),

showing that these assumed values are reasonable and likely to have been mobilized during the flood.

The closed gates scenario is reported in Table 9. The spillway opening is completely blocked by the gates, and water can only flow over the slab. This case is similar to the overtopping of a gravity dam. Thus, the uplift pressure is estimated using the full tailwater height. All forces are computed as in the opened gates scenario. For comparison, the sliding safety factors using a tailwater height of $0.6H_0$, as recommended by guidelines for the evaluation of the downstream force $F_{d/s}$, is also computed.

Table 9 - Chute Garneau stability with closed gates

			Sliding Safety Factor				
			$F_{d/s}^{CFD}$	$F_{d/s}^{1.0H_0}$		$F_{d/s}^{0.6H_0}$	
H_0 (m)	σ_t (kPa)	c (kPa)	F_v^{CFD} - Reference	$F_v^{\alpha=2/3, \beta=1/3}$	$F_v^{\alpha=1.0, \beta=0.5}$	$F_v^{\alpha=2/3, \beta=1/3}$	$F_v^{\alpha=1.0, \beta=0.5}$
0*	0	0		2.28			
		0	1.02 (1.00)	0.99 (0.97)	1.03 (1.00)	0.97 (0.95)	1.00 (0.98)
1.06	94.6	50	1.33 (1.00)	1.30 (0.98)	1.34 (1.01)	1.27 (0.95)	1.31 (0.98)
		110	1.70 (1.00)	1.67 (0.98)	1.71 (1.01)	1.63 (0.96)	1.67 (0.98)
		0	0.90 (1.00)	0.88 (0.98)	0.92 (1.02)	0.84 (0.93)	0.88 (0.98)
1.45	113.4	50	1.19 (1.00)	1.17 (0.98)	1.22 (1.02)	1.13 (0.95)	1.17 (0.98)
		110	1.55 (1.00)	1.53 (0.99)	1.59 (1.03)	1.47 (0.95)	1.52 (0.98)
		0	0.81 (1.00)	0.79 (0.98)	0.85 (1.04)	0.74 (0.91)	0.79 (0.98)
1.78	128.2	50	1.10 (1.00)	1.09 (0.99)	1.14 (1.04)	1.02 (0.93)	1.07 (0.97)
		110	1.44 (1.00)	1.44 (1.00)	1.50 (1.04)	1.35 (0.94)	1.41 (0.98)
		0	0.72 (1.00)	0.71 (0.99)	0.77 (1.07)	0.64 (0.89)	0.70 (0.97)
2.18	147.0	50	0.99 (1.00)	1.00 (1.01)	1.06 (1.07)	0.91 (0.92)	0.97 (0.98)
		110	1.32 (1.00)	1.34 (1.02)	1.41 (1.07)	1.23 (0.93)	1.30 (0.98)

Note: The values in parenthesis represent the ratio between stability indicators using simplified method and CFD, taken as reference.

Closed gates are the worst-case scenario for stability (ignoring the presence of floating debris) because the destabilizing horizontal upstream force is significantly increased, while the stabilizing downstream force decreases, and the vertical force on the crest stays about the same. The use of

$\alpha = 1.0$ and $\beta = 0.5$ lead to a small overestimation of the SSF (approximately 7% when $H_0 = 2.18$ m), while the proposed $\alpha = 2/3$ and $\beta = 1/3$ estimate the SSF accurately compared to the CFD simulations. With gates closed, the amount of tensile strength to avoid cracking and cohesion to reach the minimum safety factor are increased from 70 kPa to 150 kPa compared with the gates opened scenario. Likewise, the minimum cohesion necessary to ensure stability increased from 50 kPa to 110 kPa compared with the gates opened scenario. Nevertheless, the assumed tensile strength and cohesion values are within the lower bound limits presented by Lo and Grass (1994) and EPRI (1992). Moreover, the resultant force is always positioned outside of the section, and the only mechanism that prevents the spillway from overturning is the tensile strength allowed.

Three cases with a partially closed gate were also modelled. In these cases, the gate is lifted halfway up the spillway opening, partially blocking the flow over the spillway chute and preventing overtopping on the bridge, as shown in Figure 47. For a flow of $12 \text{ m}^3/\text{s}$, the total upstream headwater was 7.42 m, using $c = 50 \text{ kPa}$; the SSF was 1.51, and the maximum tensile stress was 81.6 kPa. These results can be compared with the opened gates case with $H_0 = 1.10$ m (the total upstream headwater is 7.40 m) and the closed gates case with $H_0 = 1.06$ (the total upstream headwater is 7.36 m). In the equivalent opened gate case, the SSF obtained was 1.64 and the maximum tensile stress required was 33.7 kPa. In the equivalent closed gates case, the SSF obtained was 1.33, and the maximum tensile stress was 94.6 kPa. This indicates that the partially closed gates case is more critical in terms of the overturning moments developed on the gate than in terms of the sliding forces. These and the other results for the partially closed gates case are shown in Table 10.

Table 10 - Chute Garneau stability with partially closed gates

H (m)	σ_t (kPa)	c (kPa)	SSF - F_v^{CFD}	Resultant Position in %** - F_v^{CFD}
5.58	0	0	2.52	60.63
		50	3.04	
6.4	24.4	0	1.72	76.47
		50	2.10	
7.42	81.6	0	1.17	101.84
		50	1.51	

** Expressed in percentage of base width from upstream.

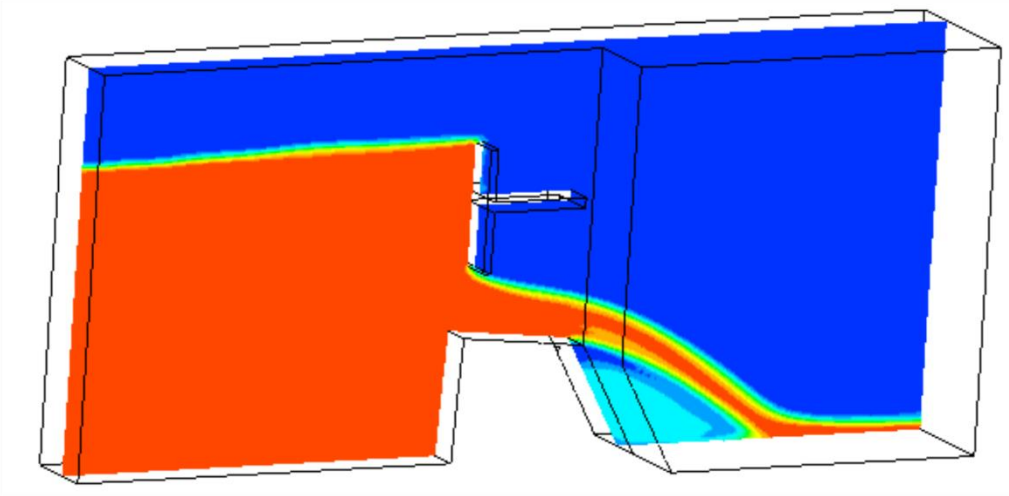


Figure 47 –Chute Garneau spillway CFD model with Partially closed gates for $H = 7.42 \text{ m}$

7.4. Floating Debris

An opened gates case with floating debris is now modelled. The debris is considered to become stuck in the gate's lifting structure and accumulates for a length of 6 m, thus spanning the entire spillway width. The presence of floating debris is considered by modelling an obstacle to the flow at the water surface level, as shown in Figure 48. Only the additional inertial and drag force are considered. The force due to the impact of the floating debris against the structure is not studied here. Beyond adding the inertial and drag forces to the structure, the presence of debris also changes the flow conditions, causing a modification in pressure fields.

A single case with floating debris is modelled, where the overtopping height is 2 m and there was 1 m of submerged debris. The total thrust caused by the debris was computed with CFD as 16.8 kN and applied at an elevation of 7.75 m. The SSF obtained with $c = 50 \text{ kPa}$ was 1.23, and the maximum tensile stress was 72.3 kPa. An equivalent open gates case with no debris and 2 m of overtopping height was modelled for comparison. The SSF obtained in this case was 1.30 and the maximum tensile stress was 63.2 kPa. Similar to the partially closed gates case, the presence of floating debris significantly increases the overturning moment, even with a small increase in the sliding force.

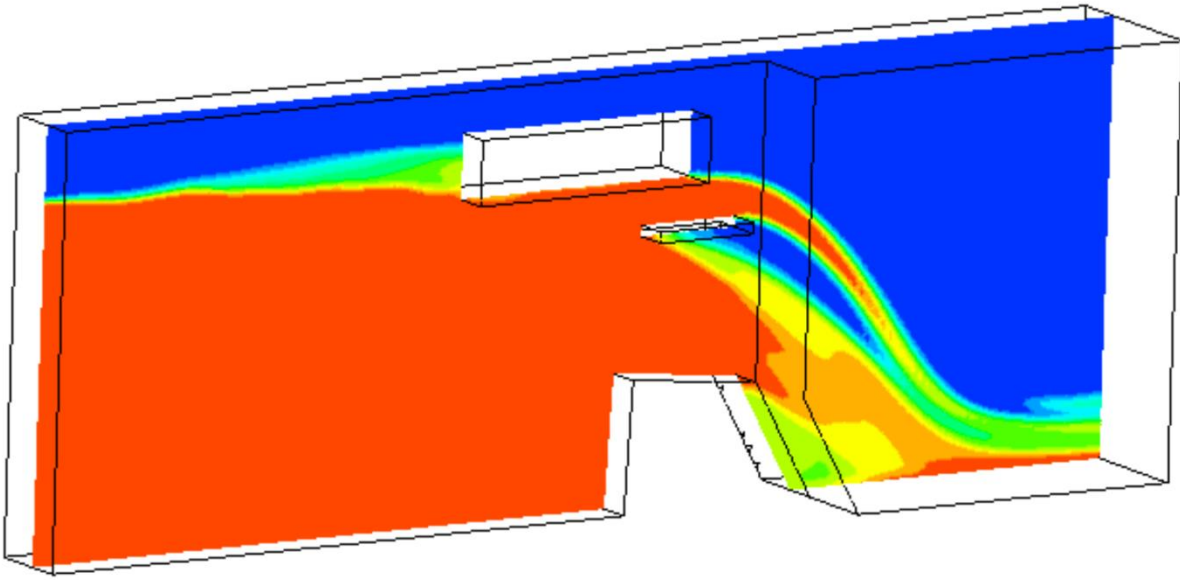


Figure 48 –Chute Garneau spillway CFD model with floating debris for $H_0 = 2\text{ m}$

8. CONCLUSIONS AND RECOMMENDATIONS

This work presented a CFD modelling methodology to compute the hydrodynamic pressure field for overtopped structures and assess their stability. An improved estimation method for the pressure on the crest of an overtopped dam is proposed. The stability of an overtopped dam is evaluated with the proposed method and compared with safety guidelines and CFD. Finally, a back analysis of the Chute Garneau spillway under the Saguenay flood conditions was performed to study the mechanisms that granted stability to the structure.

The modelling of the flow around a square cylinder was useful to learn how to properly model simple flows and validate Fluent ability to accurately the pressure fields. The water tap model showed that a mesh refinement along the interface between the phases is important to accurately compute the position of the interface. At the same time, the mesh refinement on other regions of the domain does not affect the computation of the position of the interface. Thus, the mesh adaptation strategy is very useful for this kind of problem.

The modelling of the standard ogee spillway showed that the CFD model is capable of accurately predicting the flow trajectory and hydrodynamic pressures. The use of the SST $k - \omega$ turbulence model showed good correlation with the empirical results provided by USACE (1970). Using a mesh with 10 cells per metre, the upper nappe profile is almost identical to that provided by USACE. The pressure field along the crest is very similar to those provided by USACE for all overtopping heights tested, especially for cases in which positive pressure is developed. This is important because most sections of the structures studied herein are under positive pressure.

The CFD rectangular broad-crested weir model used for validation was capable of replicating the experimental results from Hager and Schwalts (1994) with great accuracy. Both the 2D aeration strategy proposed by Hargreaves et al. (2007) and the 3D aeration strategy proposed herein yielded very similar, accurate results. Because it is more versatile and easier to apply in complex structures, the 3D strategy is recommended.

For gravity dams with rectangular crests, the evaluation of the weight of the overflowing nappe with upstream height H_0 showed that the pressure head values $\alpha = 1$ at the upstream edge and

$\beta = 0.5$ at the downstream edge often used to estimate the vertical force overestimate its magnitude by approximately 43%, on average. Using CFD modelling and simulation, we recommend the use of $\alpha = 2/3$ and $\beta = 1/3$ instead. The resulting pressure field predicts the vertical force magnitude with much better accuracy, underestimating it by only 5% on average. From this section of the study, it was also noted that the pressure field on the upstream wall of the dam is nearly hydrostatic. This is because the velocity upstream is very small and consequentially, the contribution from the kinetic energy is very small if compared to the contribution from the gravitational potential energy. Thus, it is reasonable to estimate the hydrodynamic pressure field on the upstream wall as being hydrostatic.

The stability of a 7.6 m-high gravity dam was analyzed using CFD and safety guidelines with and without the presence of tailwater. In both cases, the use of the proposed coefficients $\alpha = 2/3$ and $\beta = 1/3$ lead to an accurate estimate of the sliding safety factors (SSF) when compared to CFD results, while $\alpha = 1.0$ and $\beta = 0.5$ overestimate the SSF. Moreover, the recommendation to consider the vertical force on the crest as zero greatly underestimates the SSF, especially when considerable overtopping is involved.

For design purposes, we recommend that the uplift pressure is considered as indicated in the safety guidelines assuming the full tailwater height. The downstream force should also follow the safety guidelines and assume 60% of the tailwater height. We showed that this force can be significantly larger depending on the flow conditions. However, a more precise estimation of this force without using CFD is difficult to achieve, and its influence on the SSF is less than 10%. Thus, the additional effort and complexity to better estimate this force would only slightly increase the SSF.

The Chute Garneau spillway analysis indicated that for both opened and closed gates scenarios, the minimum SSF acceptance criteria were met when 150 kPa of tensile strength and 110 kPa of cohesion were considered. The tensile strength and cohesion adopted in the stability analysis are well within the range presented by Lo and Grass (1994) and the EPRI (1992), which present a lower bound of 310 kPa for tensile strength and 480 kPa for cohesion. This shows that although the guidelines do not recommend reliance on rock-concrete tensile strength to ensure stability, it may contribute significantly to stability during an extreme flood. This may make the difference between the structure failing or surviving the event. Both the partially closed gates and the floating

debris scenarios mainly affected the structure stability by increasing the overturning moment with a relatively small increase in horizontal forces with a longer lever arm. Thus, in both cases, the increase in tensile stress is more significant than the increase in the SSF.

From the results and the experience obtained from this project, the following recommendations for future projects are given:

- For improved accuracy and to analyze more complex systems, a cluster of computers should be used as a single workstation computer is not capable of running a model with more than a couple hundred thousands of cells.
- The underground flow of water through the soil can be considered by modelling the soil as a porous solid. By doing this, maybe the uplift pressure can be computed in a more reliable way so that it can be used on the stability calculations.
- The gates could be modelled as a solid and a coupled CFD-mechanic analysis could be performed to study the flow-induced vibration on the gates.
- The floating debris case should be further investigated by modelling the debris as a solid floating particle rather than an obstacle and by considering the impact force on the structure for more accurate results.

REFERENCES

- ABELA, C. M. Recommendations for Determining Debris Loads for Tainter Gates. **Practice Periodical on Structural Design and Construction**, v. 23, n. 2, p. 04018006, 2018.
- ALLEN, P. **Operation of spillway gates—how to avoid the problems and pitfalls**. 34th Annual Qld Water Industry Operations Workshop. **Proceedings...** Caloundra, Queensland, Australia: 2009
- ALVI, Irfan A. **Failure of Sella Zerbino Secondary Dam in Molare, Italy**. Association of State Dam Safety Officials, 2015.
- ANCOLD. **Guidelines on design criteria for concrete gravity dams**. Australian National Committee for Large Dams, Hobart, Tasmania, Australia, 1991.
- ANSYS. **ANSYS Fluent Theory Guide**. ANSYS, Inc, 2018.
- ARANTES, E. J. **Caracterização do escoamento sobre vertedouros em Degraus via CFD**. Ph.D. Thesis, Escola de Engenharia de São Carlos, Universidade de São Paulo, 2007.
- ARAKAKI JR., H. **Estudo dos esforços de correnteza marítima em risers com uso de CFD**. Master's Dissertation, Faculdade de Engenharia Mecânica e Instituto de Geociências, UNICAMP, 2016.
- AYDIN, M. C.; OZTURK, M. Verification and validation of a computational fluid dynamics (CFD) model for air entrainment at spillway aerators. **Canadian Journal of Civil Engineering**, v. 36, n. 5, p. 826–836, 2009.
- BATCHELOR, G. K. **An Introduction to Fluid Dynamics**. Cambridge: Cambridge University Press, 2000.
- BOSCH, G.; RODI, W. Simulation of Vortex Shedding Past a Square. **International journal for numerical methods in fluids**, v. 17, n. 3, p. 267–275, 1996.

BREUR, M. et al. Accurate computations of the laminar flow past a square cylinder. **International Journal of Heat and Fluid Flow**, v. 21, p. 186–196, 2000.

BROOKS, G. R.; LAWRENCE, D. E. Geomorphic Effects of Flooding Along Reaches of Selected Rivers in the Saguenay Region, Québec, July 1996. **Géographie physique et Quaternaire**, v. 54, n. 3, p. 281–299, 2000.

BURNHAM, J. **Modeling dams with computational fluid dynamics: Past success and new directions**. Association of State Dam Safety Officials Annual Conference. **Proceedings...** Washington, DC: 2011

CAPART, H. et al. The 1996 Lake Ha! Ha! breakout flood, Québec: Test data for geomorphic flood routing methods. **Journal of Hydraulic Research**, v. 45, Extra Issue, p. 97–109, 2007.

CARNEIRO, D. L. **Análise de Vibrações Induzidas por Vórtices em Estruturas Offshore Utilizando Modelos Numéricos Tridimensionais no Domínio do Tempo**. Master's Dissertation, COPPE, UFRJ, 2007.

CASTILLO, L. G.; CARRILLO, J. M. **Hydrodynamics characterisation in plunge pools. Simulation with CFD methodology and validation with experimental measurements**. 2nd European IAHR Congress. **Proceedings...** Munich, Germany: 2012

CASTILLO, L. G.; CARRILLO, J. M. **Analysis of the Scale Ratio in Nappe Flow Case by Means of CFD Numerical Simulation**. IAHR Congress. **Proceedings...** Beijing, China: 2013

CASTILLO, L. G.; CARRILLO, J. M.; SORDO-WARD, Á. Simulation of overflow nappe impingement jets. **Journal of Hydroinformatics**, v. 16, n. 4, p. 922–940, jul. 2014.

CBC. **What we know about the dam at risk of failing in western Quebec**. Available from: <<https://www.cbc.ca/news/canada/montreal/bell-falls-what-we-know-1.5112853>>. Accessed on: June 12, 2019

CDA. **Dam Safety Guidelines**. Canadian Dam Association, Edmonton, Alberta, Canada, 2013.

COSTA, L. M. F. **Investigação numérica de modelos de turbulência no escoamento do vento em pontes suspensas**. Master's Dissertation, Escola Politécnica, USP, 2018.

DHIMAN, A. K.; CHHABRA, R. P.; ESWARAN, V. Steady flow of power-law fluids across a square cylinder. **Chemical Engineering Research and Design**, v. 84, n. 4 A, p. 300–310, 2006.

DIAS, A. **Análise do Desempenho Hidráulico de uma Soleira Lateral Através de CFD**. Master's Dissertation, Escola Politécnica, USP, 2011.

DOUGLAS, K.; SPANNAGLE, M.; FELL, R. **Analysis of Concrete and Masonry Dam Incidents**. University of New South Wales, Sydney, 1998.

EBNER, L. et al. **Numerical Modeling of the Spillways for the Dam Raise at Isabella Dam**. B. Crookston & B. Tullis (Eds.), Hydraulic Structures and Water System Management. 6th IAHR International Symposium on Hydraulic Structures. **Proceedings...** Portland, OR: 2016

EPRI. **Uplift pressures, shear strengths, and tensile strengths for stability analysis of concrete gravity dams**. Electric Power Research Inst, Palo Alto, California, 1992.

FAVRE, É. **Évaluation de la Stabilité des Ouvrages Poids Soumis à la Submersion Basée sur la Dynamique Numérique des Fluides**. Master's Dissertation, Département des Génies Civil, Géologique, et des Mines, École Polytechnique de Montréal, 2018.

FAVRE, E., LÉGER, P. **Structural Stability Assessment of Gravity Dams and Spillways Subjected to Overtopping Using CFD**. CDA 2018 Annual Conference. **Proceedings...** Québec, QC, Canada: Oct 15-17, 2018.

FERC. **Engineering guidelines for evaluation of hydropower projects—Chapter III Gravity Dams**. Federal Energy Regulatory Commission, Office of Hydropower Licensing, Report No. FERC 0119-2, Washington DC, USA, 1991.

FERC. **Engineering guidelines for the evaluation of hydropower projects - Draft chapter III: Gravity Dams**. Federal Energy Regulatory Commission, Office of Energy Projects, Division of Dam Safety and Inspections, Washington D.C., USA, 2016.

FERREIRA, J. L. **Um Estudo de Ações Dinâmicas em Plataformas Offshore Utilizando Dinâmica dos Fluidos Computacional**. Undergraduate Monograph, Departamento de Engenharia Civil e Ambiental, Universidade de Brasília, 2012.

FILL, G. C. **Modelagem Hidrodinâmica 3D De Escoamentos Em Vertedouros**. Master's Dissertation, Departamento de Hidráulica e Saneamento, UFPR, 2011.

FRANKE, R.; RODI, W.; SCHÖNUNG, B. Numerical Calculation of Laminar Vortex- Shedding Flow Past Cylinders. **Journal of Wind Engineering and Industrial Aerodynamics**, v. 35, p. 237–257, 1990.

FREITAS, M. R.; PEDROSO, L. J. **Guia de Modelagem de Escoamento Bidimensional Utilizando o Software ANSYS Fluent**. Report n. RTP-MRF2-07/2018, Departamento de Engenharia Civil e Ambiental, Universidade de Brasília, 2018.

FREITAS, M. R.; PEDROSO, L. J. **Estudo de Convergência e Validação de Resultados para Escoamento Laminar Permanente em Torno de Seções Quadradas Usando o Fluent**. Report n. RTP-MRF3-08/2018, Departamento de Engenharia Civil e Ambiental, Universidade de Brasília, 2018.

FREITAS, M. R.; PEDROSO, L. J. **Estudo de Convergência e Validação de Resultados para Escoamento Laminar Transiente em Torno de Seções Quadradas Usando o Fluent**. Report n. RTP-MRF4-09/2018, Departamento de Engenharia Civil e Ambiental, Universidade de Brasília, 2018.

FRENCH MINISTRY OF AGRICULTURE. **Technique des barrages en aménagement rural**, Paris, France, 1977.

FUNG, K. B. et al. **Application of Remote Sensing to Environmental Monitoring: A Case Study of the 1996 Saguenay Flood in Québec**. Annual meeting of the Geological Association of Canada/Mineralogical Assoc. of Canada. **Proceedings...** Quebec: 1998

GACEK, J.D. **Numerical simulation of flow through a spillway and diversion structure**. M.Sc. thesis, Department of Civil Engineering and Applied Mechanics, McGill University, Montreal, Q.C., Canada, 2007.

GESSLER, D. **CFD Modeling of Spillway Performance**. World Water and Environmental Resources Congress. 2005

GODTLAND, K.; TESAKER, E. **Clogging of spillways by trash**. Proc. 18th ICOLD Congress, pp. 543–557 **Proceedings...** Durban, South Africa, 1994.

GRAHAM, W. J.; HILLDALE, R. C. **Spillway Gate Failure or Misoperation: Representative Case Histories**. U.S. Department of the Interior, Bureau of Reclamation, 2002.

GRIFFITH, R.A. et al. **Stability review of the Wanapum spillway using CFD analysis**. Canadian Dam Association, Bulletin, p. 16–26, 2007.

HAGER, W. H.; SCHWALT, M. Broad-Crested Weir. **Journal of Irrigation and Drainage Engineering**, v. 120, n. 1, p. 13–26, jan. 1994.

HARGREAVES, D. M.; MORVAN, H. P.; WRIGHT, N. G. Validation of the Volume of Fluid Method for Free Surface Calculation: The Broad-Crested Weir. **Engineering Applications of Computational Fluid Mechanics**, v. 1, n. 2, p. 136–146, 19 jan. 2007.

HALLAK, P. H. **Parâmetros Aeroelásticos para Pontes via Fluidodinâmica Computacional**. Master's Dissertation, COPPE, UFRJ, 2002.

HARTFORD, D. N. D. et al. **Operational safety of dams and reservoirs - Understanding the reliability of flow-control systems**. London, UK: ICE Publishing, 2016.

HAUN, S.; OLSEN, N. R. B.; FEURICH, R. Numerical Modeling of Flow Over Trapezoidal Broad-Crested Weir. **Engineering Applications of Computational Fluid Mechanics**, v. 5, n. 3, p. 397–405, 19 jan. 2011.

HIRT, C.; NICHOLS, B. Volume of fluid (VOF) method for the dynamics of free boundaries. **Journal of Computational Physics**, v. 39, n. 1, p. 201–225, jan. 1981.

HO, D., BOYES, K., DONOHOO, S. **Investigation of Spillway Behaviour under Increased Maximum Flood by Computational Fluid Dynamics Technique**. 14th Australasian Fluid Mechanics Conference. **Proceedings...** Adelaide University, Adelaide, Australia, December 10-14, 2001.

HO, D. K. H.; RIDDETTE, K. M. Application of computational fluid dynamics to evaluate hydraulic performance of spillways in australia. **Australian Journal of Civil Engineering**, v. 6, n. 1, p. 81–104, 22 jan. 2010.

ICOLD. **Dam failures statistical analysis, Bulletin 99**. International Commission on Large Dams, Paris, 1995.

ICOLD. **Tailings Dams Risk Of Dangerous Occurrences - Lessons Learnt From Practical Experiences Commission**. ICOLD. Paris, 2001.

ICOLD. **World Register of Dams - General Synthesis**. Available from: <http://www.icold-cigb.net/GB/world_register/general_synthesis.asp>. Accessed in 25 March 2018.

ICOLD. **World Register of Dams - Classification By Type**. Available from: <http://www.icold-cigb.net/article/GB/world_register/general_synthesis/classification-by-type>. Accessed in: 10 April 2019.

INSTITUTO DA ÁGUA. **Curso de Exploração e Segurança de Barragens**. Lisboa: Instituto da Água, 2001.

JAIMAN, R. K.; SEN, S.; GURUGUBELLI, P. S. A fully implicit combined field scheme for freely vibrating square cylinders with sharp and rounded corners. **Computers and Fluids**, v. 112, n. May, p. 1–18, 2015.

JAMESON, A. **Computational Fluid Dynamics: Past, Present and Future**. Stanford, Stanford University, 2012.

JOHNSON, M. C.; SAVAGE, B. M. Physical and numerical comparison of flow over ogee spillway in the presence of tailwater. **Journal of Hydraulic Engineering, ASCE**, v. 132, n. December, p. 1353–1357, 2006.

KANYABUJINJA, P. **CFD Modelling of Ogee Spillway Hydraulics and Comparison with Physical Model Tests**. M.Sc. thesis, Faculty of Engineering, Stellenbosch University, Stellenbosch, South Africa, 2015.

KERMANI, E. F.; BARANI, G. A. Numerical simulation of flow over spillway based on the CFD method. **Scientia Iranica A**, v. 21, p. 91–97, 2014.

KETTNER F. **Numerical modelling of flow over spillways**. M.Sc. thesis, Department of Hydraulic and Environmental Engineering, Norwegian University of Science and Technology, Trondheim, Norway, 2010.

KIM, D. G.; PARK, J. H. Analysis of flow structure over ogee-spillway in consideration of scale and roughness effects by using CFD model. **J. Civil Eng. KSCE**, v. 9, n. 2, p. 161–169, 2005.

KOSITGITTIWONG, D.; CHINNARASRI, C.; JULIEN, P. Y. Numerical simulation of flow velocity profiles along a stepped spillway. **Proceedings of the Institution of Mechanical Engineers, Part E: Journal of Process Mechanical Engineering**, v. 227, n. 4, p. 327–335, 22 nov. 2013.

KUMCU, S. Y. Investigation of flow over spillway modeling and comparison between experimental data and CFD analysis. **KSCE Journal of Civil Engineering**, v. 21, n. 3, p. 994–1003, 24 mar. 2017.

LAMURA, A. et al. Multi-Particle Collision Dynamics: Flow Around a Circular and a Square Cylinder. **Europhys. Lett**, v. 56, n. 3, p. 768, 2001.

LAPOINTE, M. F. et al. Response of the Ha ! Ha ! River to the flood of July 1996 in the Saguenay Region of Quebec : Large-scale avulsion in a glaciated valley. **Water Resources Research**, v. 34, n. 9, p. 2383–2392, 1998.

LAUNDER, B. E.; SPALDING, D. B. The numerical computation of turbulent flows. **Computer Methods in Applied Mechanics and Engineering**, v. 3, n. 2, p. 269–289, 1974.

LECLERC, M., LÉGER, P. **Computer aided analysis of concrete gravity dams, gated spillways and water intake structures - CADAM3D User Manual**, Version 2.4, Polytechnique Montreal, Canada, 2017.

LECLERC, M.; LÉGER, P.; TINAWI, R. **CADAM - User Manual**. Montreal, 2001.

LECLERC, M.; LÉGER, P.; TINAWI, R. Computer aided stability analysis of gravity dams - CADAM. **Advances in Engineering Software**, v. 34, n. 7, p. 403–420, 2003.

LÉGER, P., TINAWI, R., LARIVIÈRE, R. The behaviour of Gravity Dams and Spillways in Extreme Floods: Canadian Experience. **Journal Hydropower and Dams**, v. 5, n. 3, p. 73-77, 1998.

LÉGER, P. et al. **Performance of Gated Spillways During the 1996 Saguenay Flood (Québec, Canada) and Evolution of Related Design Criteria**. Commission Internationale des Grands Barrages, Vingtième Congrès Des Grands Barrages. **Proceedings...** Beijing, 2000.

LÉGER, P. **Dam Compendium - Hydrological Safety and Dam, Spillways Stability During Flood (Chapter 6)**. Pre-Release version. Polytechnique Montreal. 2019

LEWIN, J. **Hydraulic gates and valves: in free surface flow and submerged outlets**. Thomas Telford, 2001.

LO, K. Y.; GRASS, J. D. **Recent experience with safety assessment of concrete dams on rock foundations**. Dam Safety, Canadian Dam Association Annual Conference. **Proceedings...** Winnipeg, Manitoba: 1994

LOPES, P. P. S. DE P. **A CFD Investigation on the Flow around a Low Aspect Ratio Vertical Cylinder: Modeling Free Surface and Turbulent Effects**. Master's Dissertation, Escola Politécnica, USP, 2019.

MARGEIRSSON, B. **Computational Modeling of Flow over a Spillway in Vatnsfellsstífla Dam in Iceland**. M.Sc. thesis, Department of Applied Mechanics, Chalmers University of technology, Gothenburg, Sweden, 2007.

MELO, C. A. E. **Estudo de tensões induzidas por sismos em barragens de concreto gravidade**. Undergraduate Monograph, Departamento de Engenharia Civil e Ambiental, Universidade de Brasília, 2006.

MELO, C. **Estudo do acoplamento comporta-reservatório sob ações sísmicas**. Master's Dissertation, Departamento de Engenharia Civil e Ambiental, Universidade de Brasília, 2009.

MELO, C. A. E.; LÉGER, P.; PEDROSO, L. J. **Seismic Safety of Gated Spillways: Modeling Hydrodynamic Pressure on Gates**. 9th US National and 10 th Canadian Conference on Earthquake Engineering: Reaching Beyond Borders. **Proceedings...** Toronto: 2010

MELO, C. A. E.; PEDROSO, L. J.; LÉGER, P. **Um Estudo de Comportas Hidráulicas sob Ações Sísmicas Considerando os Efeitos do Acoplamento Estrutura-Reservatório**. XXXIV IBERO LATIN AMERICAN CONGRESS ON COMPUTATIONAL METHODS IN ENGINEERING (CILAMCE 2013). **Proceedings...** Pirinópolis: 2013

MENDES, N.B. **Um Estudo de Propagação de Ondas e Aplicação do Sismo na Análise Dinâmica Acoplada a Barragem em Arco-Reservatório-Fundação**. Ph.D. Thesis, Departamento de Engenharia Civil e Ambiental, Universidade de Brasília, 2018.

MENTER, F. R. **Zonal two equation k- ω turbulence models for aerodynamic flows**. 24th Fluid Dynamics Conference. **Proceedings...** Orlando, Florida: 1993

MILBRANDT, J. A.; YAU, M. K. A Mesoscale Modeling Study of the 1996 Saguenay Flood. **Monthly Weather Review**, v. 129, n. 6, p. 1419–1440, 2001.

MORAIS, V. H. P. DE. **Modelagem numérica e experimental aplicada a um vertedouro de superfície composto por um perfil creager e um dissipador do tipo roller-bucket**. Master's Dissertation, Faculdade de Engenharia Civil, Arquitetura e Urbanismo, UNICAMP, 2015.

NAGARAJAN, B.; YAU, M. K.; FILLION, L. A Numerical Study of the 1996 Saguenay Flood Cyclone: Effect of Assimilation of Precipitation Data on Quantitative Precipitation Forecasts. **Monthly Weather Review**, v. 134, n. 5, p. 1371–1388, 2006.

NGUYEN, P. **Analyse comparative entre la France et le Québec en matière de législation relative à la Sécurité des barrages et les pratiques sur la Gestion des crues**. Congrès CFBR-SHF: Dimensionnement et Fonctionnement des Évacuateurs de crues. **Proceedings...** Paris, January 20-21, 2009.

NOVAK, P et al. **Hydraulic Structures**. 4. ed. Abingdon: Taylor & Francis, 2007.

OLIVEIRA, F. F. DE. **Análise de Tensões e Estabilidade Global de Barragens de Gravidade de Concreto**. Master's Dissertation, Departamento de Engenharia Civil e Ambiental, Universidade de Brasília, 2002.

OLSEN, N. R. B.; KJELLESVIG, H. M. Three-dimensional numerical flow modelling for estimation of spillway capacity. **Journal of Hydraulic Research**, v. 36, n. 5, p. 775–784, 1998.

PALAVICINI, F. **Stabilité Structurale des Barrages et des Évacuateurs en Béton Submergés lors des Crues**. Master's Dissertation, Département des Génies Civil, Géologique, et des Mines, École Polytechnique de Montréal, 1998.

PATARROYO, J. et al. Hydraulic Design of the Stepped Overflow Spillway of the Muskrat Falls Hydroelectric Development. **Canadian Dam Association Bulletin**, v. 27, n. 1, p. 13-25, 2015.

PAXSON, G. et al. **The hydraulic design toolbox: Theory and modeling for the lake Townsend spillway replacement project**. Association of Dam Safety Officials - Dam Safety 2008,. **Proceedings...** Indian Wells, CA: 2008

PEDROSO, L. J. **Barragens de Concreto : Aspectos Gerais e Fundamentos do Cálculo de Tensões e da Estabilidade Baseado no Método de Gravidade**. Brasília, Universidade de Brasília, 2002.

PEDROSO, L. J. **Rudimentos de CFD Baseado No Programa ANSYS**. Brasília, Universidade de Brasília, 2017.

PEDROSO, L. J.; TINAWI, R.; LÉGER, P. **On the Prospects of Computational Fluid Dynamics in Concrete Dam Engineering**. 8th Conference on Computational Fluid Dynamics (CFD2K). **Proceedings...** Montreal: 2000

PETACCIA, G. et al. The collapse of the Sella Zerbino gravity dam. **Engineering Geology**, v. 211, n. July, p. 39–49, ago. 2016.

RAD, I. N. Application of Numerical Methods in Design of Hydraulic Structures. **Communications on Advanced Computational Science with Applications**, v. 2016, n. 1, p. 1–15, 2016.

RIBEIRO, P. M. V. **Uma Metodologia Analítica para a Avaliação do Campo de Tensões em Barragens Gravidade de Concreto Durante Terremotos**. Master's Dissertation, Departamento de Engenharia Civil e Ambiental, Universidade de Brasília, 2006.

RIBEIRO, P. M. V. **Solução Analítica Para Cavidades Acústicas Bidimensionais com Aplicação ao Estudo de Problemas de Interação Dinâmica Barragem-Reservatório**. Ph.D. Thesis, Departamento de Engenharia Civil e Ambiental, Universidade de Brasília, 2010.

SABZI, A. E.; AFROUS, A. Examining the effect of cavitation on crest spillway using Ansys-fluent software. **Journal of Scientific Research and Development**, v. 2, n. 5, p. 303–308, 2015.

SANTOS, T. C. **Um Estudo de Ações Dinâmicas do Vento em Edifícios Altos**. Undergraduate Monograph, Departamento de Engenharia Civil e Ambiental, Universidade de Brasília, 2017.

SAVAGE, B., JOHNSON, C. Flow Over Ogee Spillway: Physical and Numerical Model Case Study. **Journal of Hydraulic Engineering**. v. 127, n. 8, p-640-649, 2001.

SHARMA, A.; ESWARAN, V. Heat and fluid flow across a square cylinder in the two-dimensional laminar flow regime. **Numerical Heat Transfer; Part A: Applications**, v. 45, n. 3, p. 247–269, 2004.

SHIMIZU, Y., TANIDA, Y. Fluid Forces Acting on Cylinders of Rectangular Cross- Section. **Trans. Jpn. Soc. Mech. Eng. B**, v. 44, pp. 2699–2706, 1978.

SILVA, A. C. DA. **Análise Numérica do escoamento em Torno de Um Cilindro**. Undergraduate Monograph. Department of Civil and Environmental Engineering. Universidade de Brasília, 2018.

SILVA, R. C.; PEDROSO, L. J. **Estudo do Comportamento de Barragens Gravidade de Concreto sob Ação do Galgamento : Análise de Tensões e Estabilidade**. XXVII Seminário Nacional de Grandes Barragens-CBDB. **Proceedings...** Belém: 2007

SILVEIRA, I.V. **Estudo da Influência da Crosta Local no Comportamento Sísmico do Sistema Barragem Gravidade-Reservatório-Fundação**. Master's dissertation, Departamento de Engenharia Civil e Ambiental, Universidade de Brasília, 2018.

SOHANKAR, A.; NORBERG, C.; DAVIDSON, L. Simulation of three-dimensional flow around a square cylinder at moderate Reynolds numbers. **Physics of Fluids**, v. 11, n. 2, p. 288–306, 1999.

SOUZA, T. DA S. **Geração de Vórtices de von Kármán com Modelagem em CFD**. Master's Dissertation, Escola Politécnica, USP, 2016.

SWEENEY B.P. **Converged stepped spillway models in OpenFOAM**. M.Sc. Report, Department of Computing and Information Sciences, Kansas State University, Manhattan, Kansas, USA, 2014.

SWISS COMMITTEE ON DAMS (SCD). **Floating debris at reservoir dam spillways**. 2017. Available from: <http://www.swissdams.ch/en/publications/publications-csb/2017_Floating_debris.pdf>.

USACE. **Hydraulic Design of Spillways**. US Army Corps of Engineers. Report EM 1110-2-1603, Washington, D.C, 1970.

USACE. **Engineering and design: Gravity dam design**. US Army Corps of Engineers. Report EM 1110-2-2000, Washington, D.C, 1995.

USBR. **Design of small dams**. United States Bureau of Reclamation. Denver, Colorado, 1987.

VOSOUGHIFAR, H. R. et al. Evaluation of Fluid Flow over Stepped Spillways Using the Finite Volume Method as a Novel Approach. **Strojniški vestnik – Journal of Mechanical Engineering**, v. 59, n. 5, p. 301–310, 15 maio 2013.

WENDT, J. F. et al. **Computational Fluid Dynamics: An Introduction**. Third ed. Berlin: Springer, 2009.

WILCOX, D. C. Reassessment of the scale-determining equation for advanced turbulence models. **AIAA Journal**, v. 26, n. 11, p. 1299–1310, 1988.

WILLEY, J. et al. **Complementary Use of Physical and Numerical Modelling Techniques in Spillway Design Refinement**. Vingt-Quatrième Congrès Des Grands Barrages. **Proceedings...** Kyoto, Japan: 2012

Appendix A - User Guide for Modeling Multiphasic Open Channel Flow on Fluent Using VOF Model

The first step to model any system on ANSYS is to add the appropriate analysis system to the project schematic. In this case, we will add a Fluent analysis system and rename it to Broad Weir – 3D as shown in Figure 49.

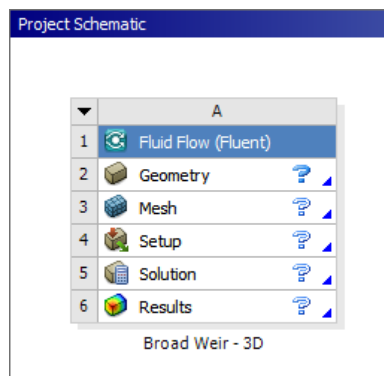


Figure 49 – Empty fluent analysis system

1.1) Geometry

Then, the first step of pre-processing is to define the geometry. There are multiple ways to do that, but for this guide we use SpaceClaim, the built in ANSYS CAD software. Clicking twice on Geometry opens SpaceClaim where we can draw the geometry of the domain. Figure 50 shows the main tools for defining the geometry of the problem. On the left side, we have the sketching tools to draw points, lines, rectangles, circles, etc. On the center we have the editing tools to modify the sketch. The Fill tool takes a sketch and generates an area limited by the sketch boundaries, the Pull toll can be used to extrude an area to make a 3D model or to change the dimensions of elements of the geometry and the Move tool can be used to move the entirety or parts of the geometry. On the right side we have the intersection tools that can be used to split the model into different regions

or different parts. This can be used to define interactions between parts and to define different kinds of mesh in different regions.

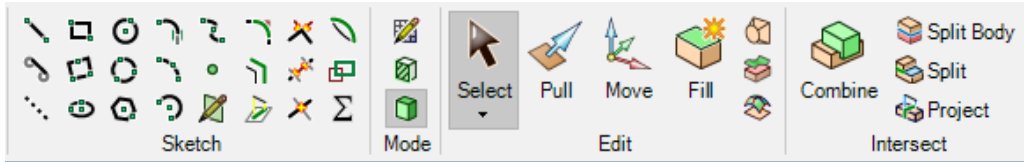


Figure 50 – Main design tools of SpaceClaim

Figure 51 shows the geometry sketch drawn to study the broad weir problem and Figure 52 shows the 3D model generated from that sketch. To create the 3D model, first we filled the area inside the sketch with the Fill toll and then we extruded the area by 10 m in the z direction.

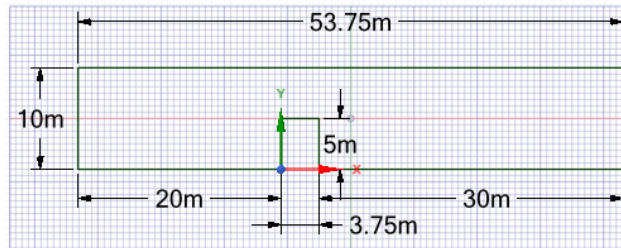


Figure 51 – Geometry sketch

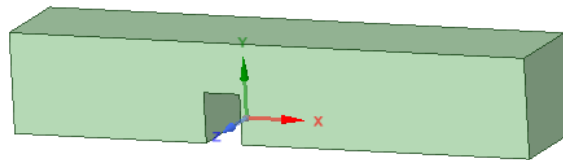


Figure 52 – Extrude 3D model

After creating the 3D model by extrusion, we can then partition the model using the Split tool to define multiple regions. We also extrude the downstream section of the channel one extra meter

on each side to allow aeration to the flow. Figure 53 shows the finalized 3D model used in this simulation.

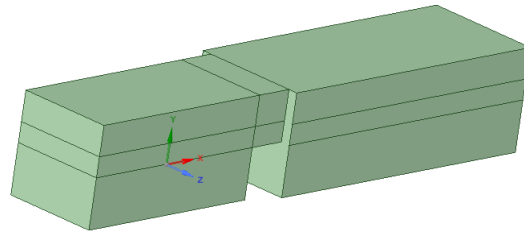


Figure 53 – Partitioned 3D model

1.2) Mesh

After defining the geometry, we can double click on the Mesh icon on the analysis system to open the ANSYS meshing software. The most important tools for manipulating the model are the selection tools, shown in Figure 54, and the wireframe tool, shown in Figure 55. The selection tools, from left to right are to selecting label or imported objects, to show the coordinates of a certain point, to define the type of selection such as single select or box select, to select a vertex, to select an edge, to select a face, to select a body, to select a node, to select an element face and to select an element. Using the correct selection tool is essential to properly manipulate the software. The wireframe tool can be used to toggle between showing the 3D model as a solid object or a wireframe diagram, the first option being better for selecting faces and the second for selecting edges.



Figure 54 –Selection tools

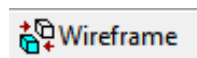


Figure 55 – Wireframe tool

The actual meshing tools can be accessed by clicking on Mesh with the right button of the mouse and hovering over Insert, as shown in Figure 56. There are multiple rules for the meshing process that can be set like, Method, Sizing and Face Meshing, which are the ones that are used for this problem.

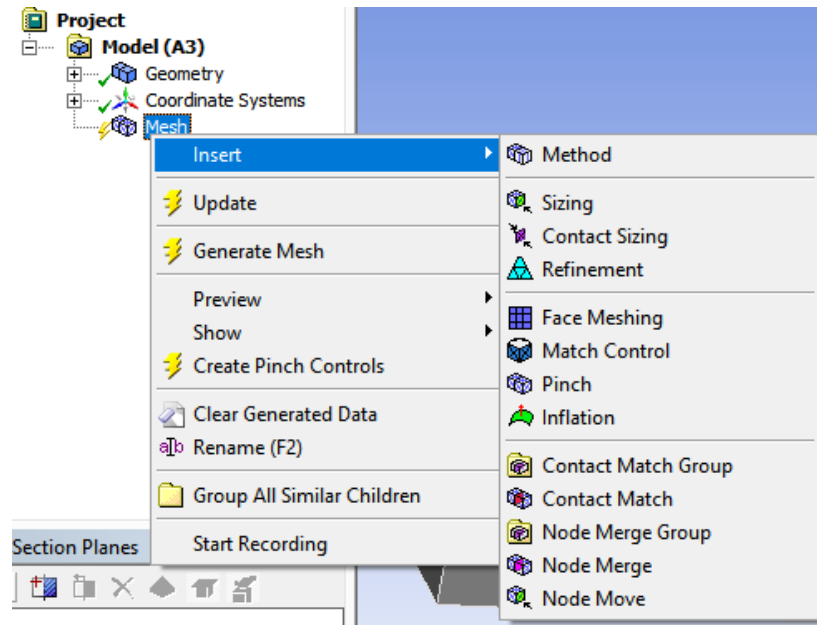


Figure 56 – Meshing tools

First, we insert edge sizing rules for all the edges of the model so that we can control the size of the elements in each direction. To do so, we first select all the edges that we want to apply the same rule using the edge selection tool. Then we can define the sizing by specifying the actual element size, the number of divisions, a sphere influence or a factor of the global size. In this case we used mostly the number of divisions. We also changed the behavior for every edge to Hard, which enforces that the elements sizes will be exactly as specified. We can also define a bias to make the element density higher on one end of the edge. Figure 57 shows an example of edge sizing with a bias towards the weir. The bias factor was set to 20, which means that the largest element is 20 times larger than the smallest element. We also reversed the bias of 4 edges to make them face the right direction. Figure 58 shows the edge sizing rules that were used for each edge.

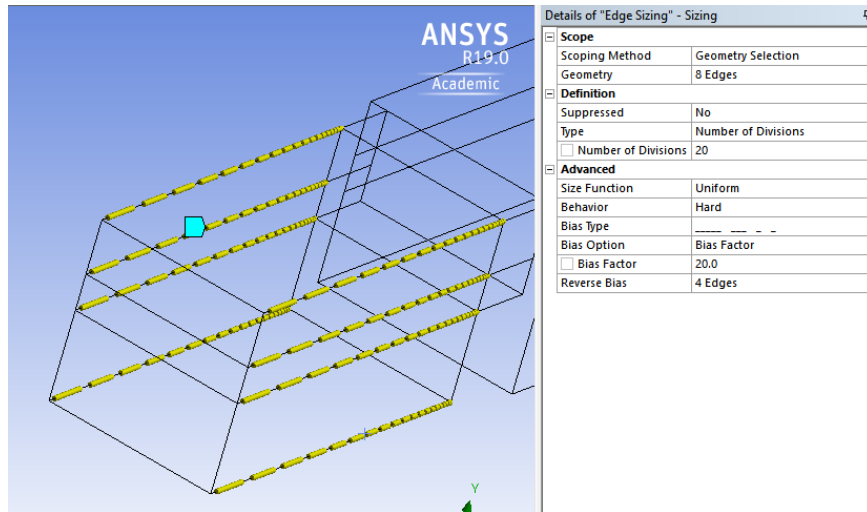


Figure 57 – Edge sizing with bias

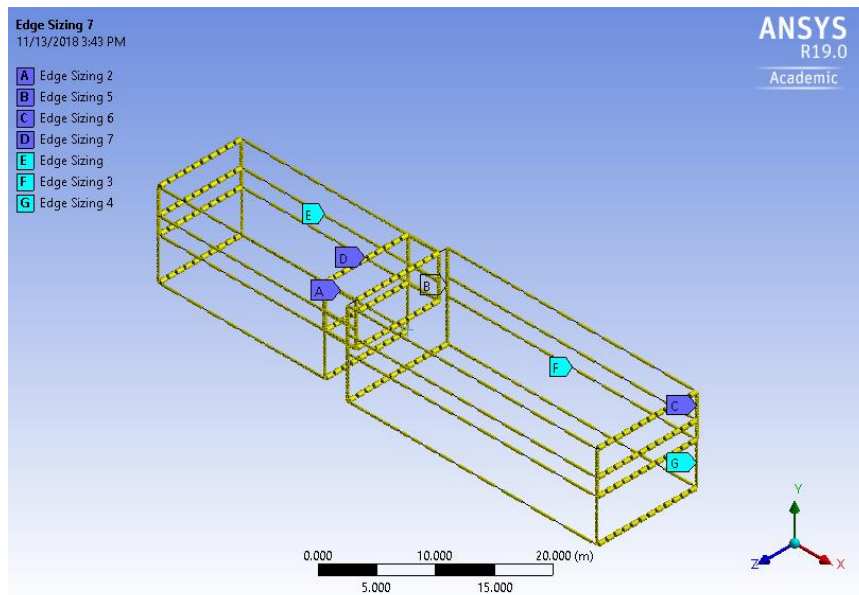


Figure 58 – Edge sizing for all edges

After setting the edge sizing rules, we defined a Face Meshing selecting all the faces so that the edge sizing rules propagate to the rest of the body. We also define a MultiZone method using hexahedrons. Together, those rules ensure that ANSYS generate a structured mesh. The settings for the face meshing and the MultiZone method are shown in Figure 59 and Figure 60.

Details of "Face Meshing" - Mapped Face Meshing	
Scope	
Scoping Method	Geometry Selection
Geometry	30 Faces
Definition	
Suppressed	No
Mapped Mesh	Yes
Constrain Boundary	No
Advanced	
Specified Sides	No Selection
Specified Corners	No Selection
Specified Ends	No Selection

Figure 59 – Face meshing settings

Details of "MultiZone" - Method	
Scope	
Scoping Method	Geometry Selection
Geometry	1 Body
Definition	
Suppressed	No
Method	MultiZone
Mapped Mesh Type	Hexa
Surface Mesh Method	Program Controlled
Free Mesh Type	Not Allowed
Element Order	Use Global Setting
Src/Trg Selection	Automatic
Source Scoping Method	Program Controlled
Source	Program Controlled
Sweep Size Behavior	Sweep Element Size
<input type="checkbox"/> Sweep Element Size	Default
Advanced	
Preserve Boundaries	Protected
Mesh Based Defeaturing	Off
Minimum Edge Length	1.0 m
Write ICEM CFD Files	No

Figure 60 – MultiZone method settings

Before generating the mesh we have to create named selections to define the different boundaries of the domain. To do that, we select one or multiple faces, click with the right button of the mouse and select Create Named Selection. After doing this, a pop-up will appear asking for the name of the named selection. This named selections will be used in Fluent to define the specific boundary conditions. Figure 61 shows how to create a named selection and Figure 62 shows all the named selections that were created in this model. Note that unnamed boundaries will be treated as walls by Fluent.

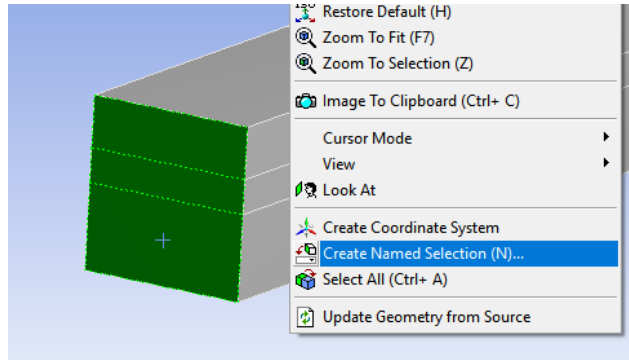


Figure 61 – Named selection creation

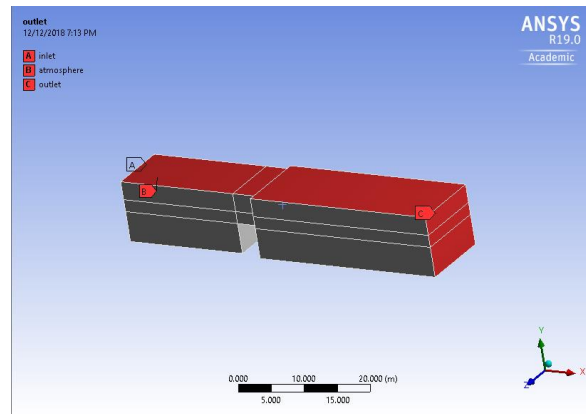


Figure 62 – All named selections

Finally, with all the meshing rules set and the named selection created we can generate the mesh by clicking on Mesh with the right button of the mouse and selection Generate Mesh. As shown in Figure 63, the mesh generated is structured, made of hexahedrons only, has multiple zones with different elements density and is biased towards the weir.

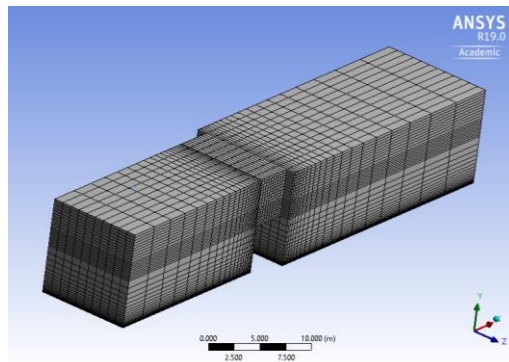


Figure 63 – Broad weir model mesh

1.3) Fluent Solver

After finishing the mesh and naming the boundaries we can open the Fluent solver by double clicking on Setup on the Project Schematic. Doing this will open the pop-up shown on Figure 64 where we can define some of the technical properties of the solver like the number of CPUs and GPUs to be used by the solver. As a general rule of thumb for this pop-up, it's recommended to always activate Double Precision, use the Parallel option and set the number of Processes equal to the number of physical cores on the computer CPU or one less than the number of physical cores. From previous testing, we noted that hyperthreading (using virtual cores) is not helpful for CFD applications and actually affects performance negatively. We also noted that the use of GPU acceleration didn't help a lot for our test cases.

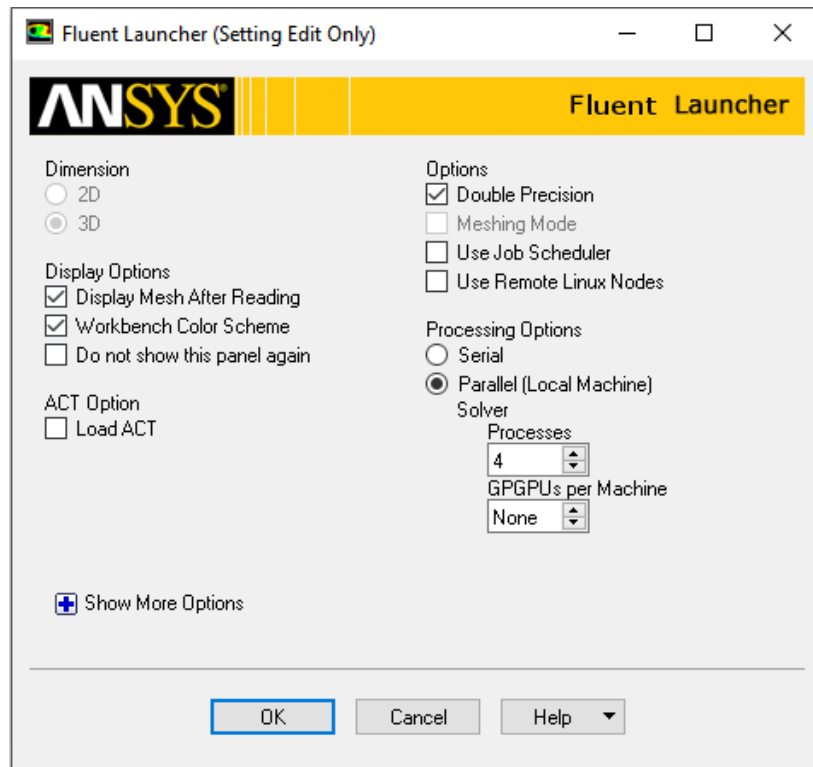


Figure 64 – Fluent launcher initialization

After setting up Fluent and clicking on OK on the pop-up show on Figure 64, Fluent main window shows up. On the left side of this window we can see all the menus used for the setup, solution and options for post-processing of the problem. First, in the General menu, we have to set Time to Transient and Gravitational Acceleration to -9.81 m/s^2 on the Y axis, as shown on Figure 65.

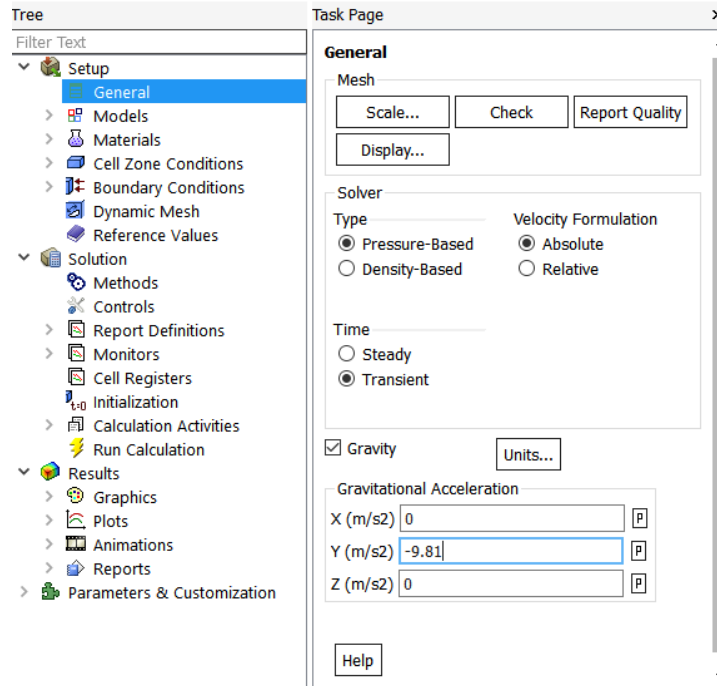


Figure 65 –General settings

Next, we proceed to the Models (shown in Figure 66) menu where we select the Volume of Fluid Model on the Multiphase option, activating the Open-Channel Flow and Implicit Body Force options and selecting Implicit Formulation, as shown on Figure 67.

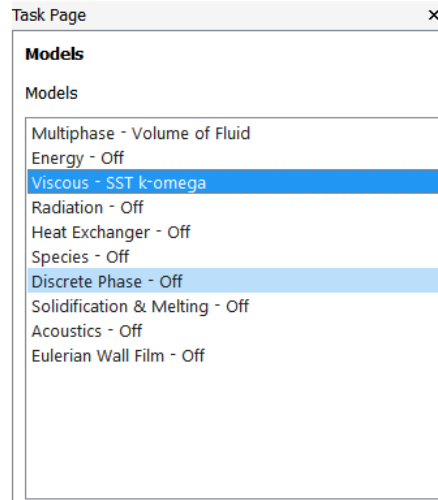


Figure 66 –Models menu

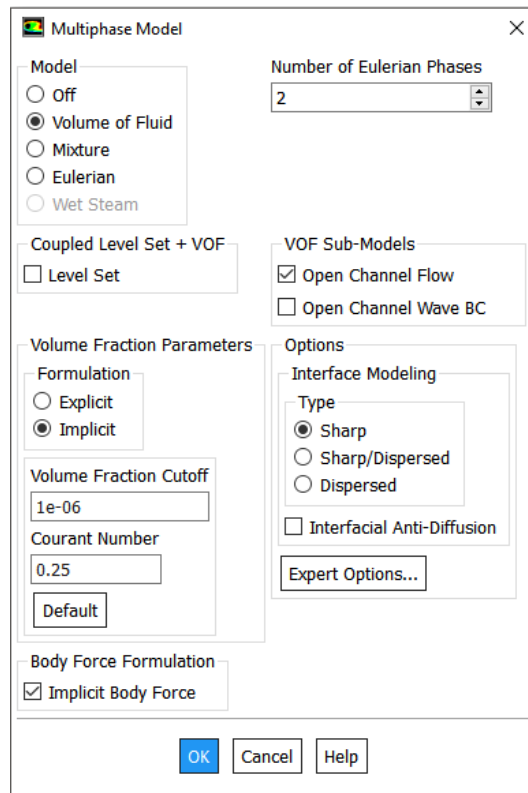


Figure 67 –Multiphase model

Still on the Models menu we change the Viscous model from Laminar to k-omega and select the SST model, as shown in Figure 68.

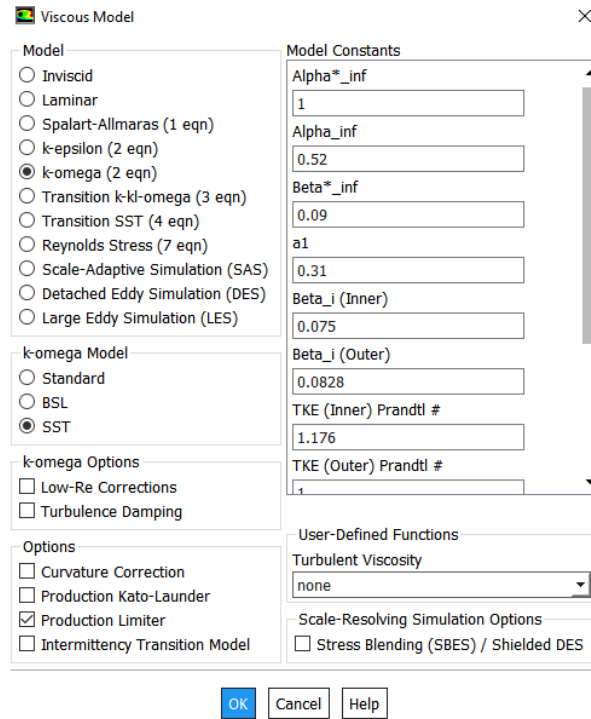


Figure 68 –Viscous model

Then we proceed to the materials menu. By default, Fluent has only air added to the fluid materials list, so we have to add water to the list. To do so, we click on Creat/Edit on the Materials menu, and then the pop-up named Creat/Edit Materials appear. From there we can click on Fluent Database, which brings the Fluent Database Materials window. There you can select any material from the database, in this case, water-liquid, and click on Copy to add it to the materials list. Figure 69 shows both pop-ups and Figure 70 shows the materials menu as it may be after adding water to the list.

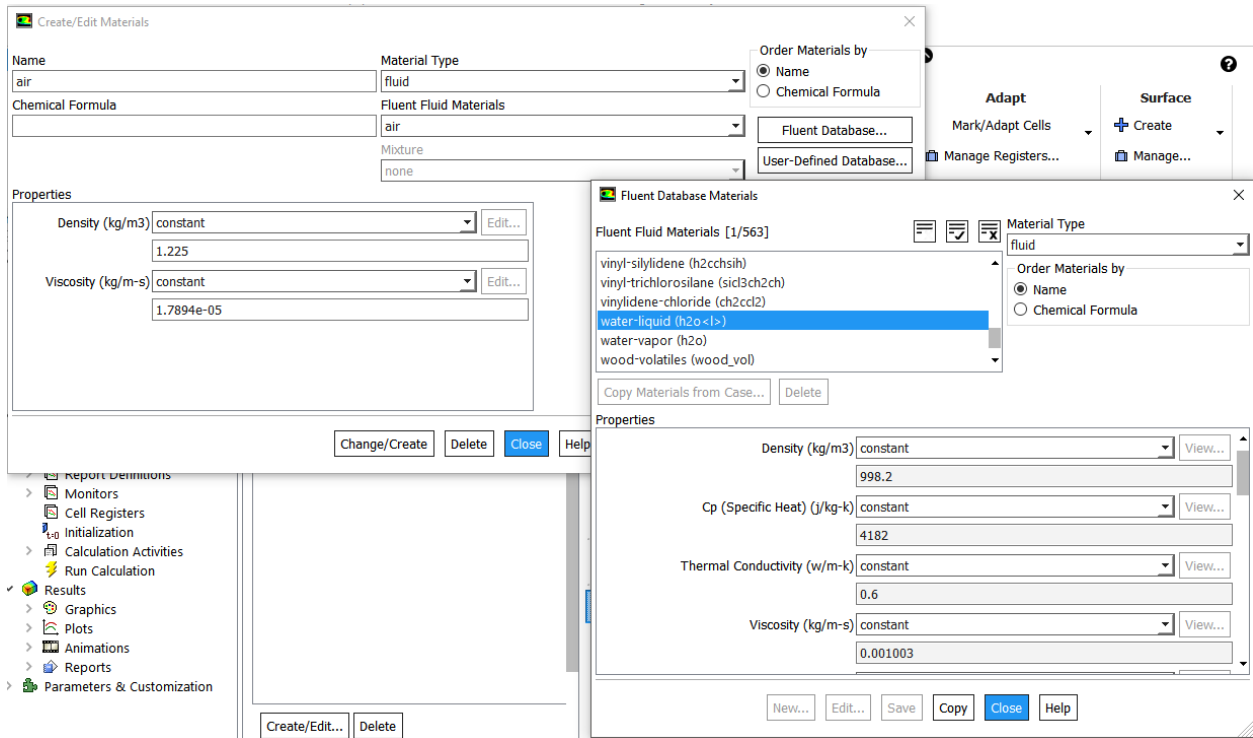


Figure 69 –Adding water to materials

Materials

Materials

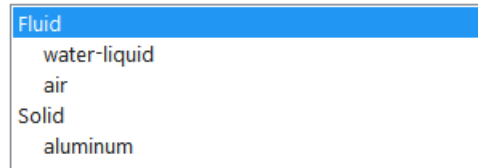


Figure 70 –Materials menu

With both materials added we have to go back to the Models menu and under the Multiphase option there will be now a Phase submenu. By double clicking this submenu the Phases window shows up with two phases added. There we have to rename the phases and choose the correct material for each one. In this case we chose to use air as the primary phase and water as the secondary. The pop-ups to do so are shown in Figure 71.

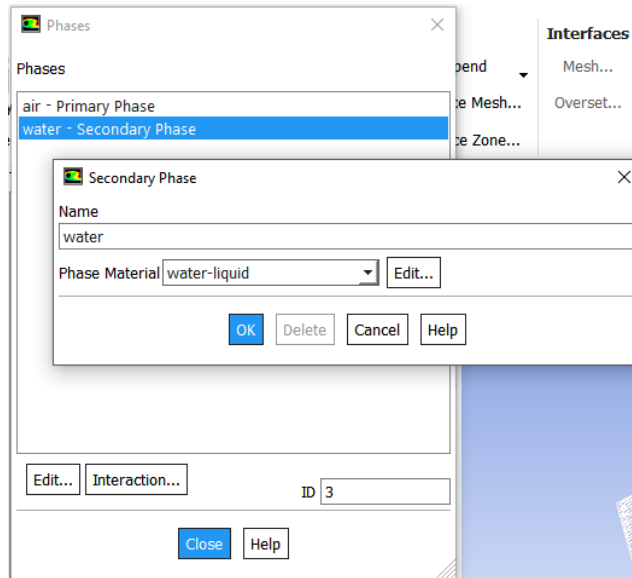


Figure 71 –Phases Definition

We also have to define the interaction between the two phases, which is via surface tension. To do so we click on Interaction on the Phases window, go to the Surface Tension tab, enable Surface Tension Force Modeling, change the drop down menu option from none to constant and type 0.072 on the line edit field bellow, which is the surface tension coefficient between water and air in N/m. Figure 72 shows how the Phase Interaction window should look when properly set up.

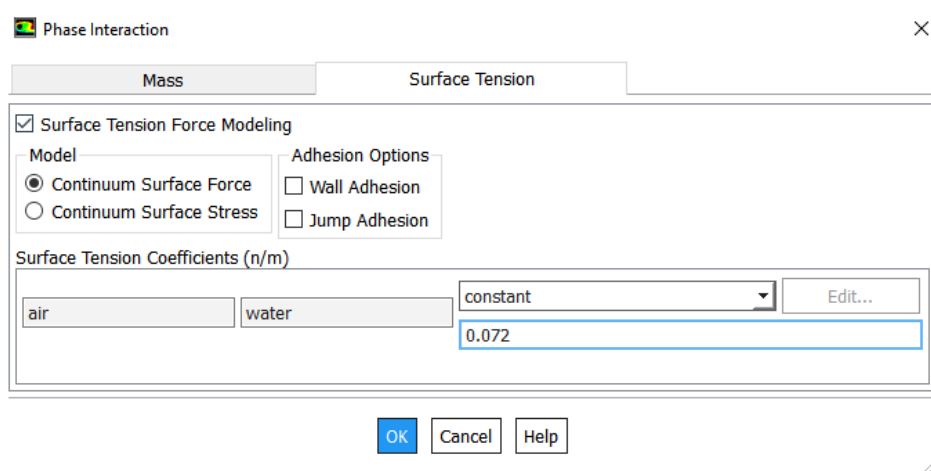


Figure 72 –Phase Interaction

Next we proceed to the Boundary Conditions menu. On this menu, the first thing that has to be set are the operating conditions. To do so we click on the Operating Conditions button on the bottom of the menu and a pop-up shows up. There we can define the reference pressure and point for the problem, which in this case was set to 0 Pa at the point (0, 10, 5), which is right in the center of the atmospheric boundary over the crest. We can also set gravity and operating density on this menu as shown in Figure 73.

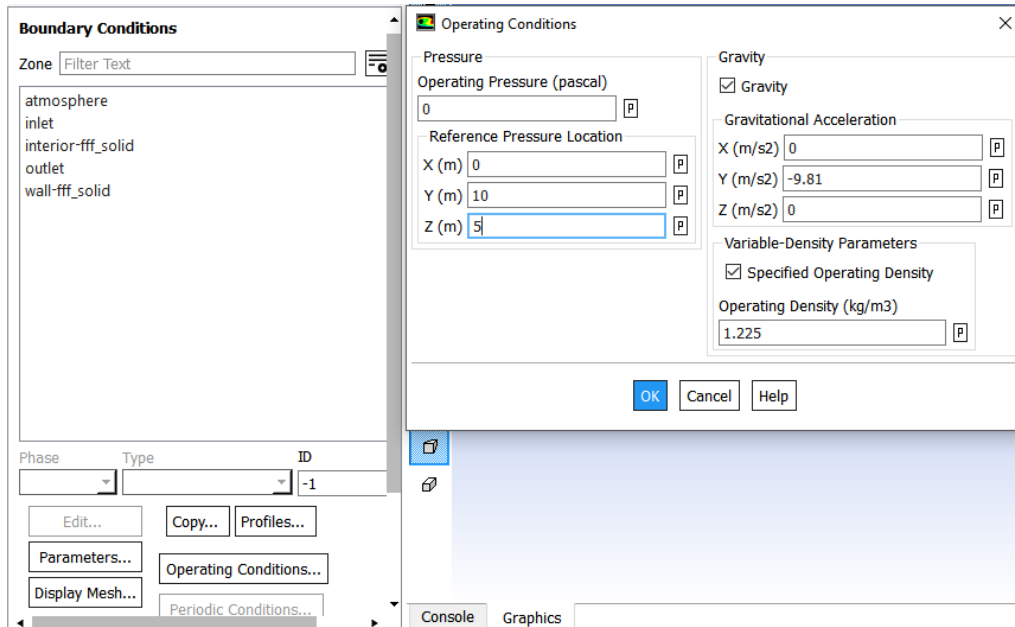


Figure 73 –Boundary conditions menu and operating conditions window

The first boundary condition we specify is the inlet. First, we have to change the boundary condition from velocity-inlet to mass-flow-inlet as shown in Figure 74. Then a window will pop-up to configure this boundary condition. There we go to the Multiphase tab, enable the Open Channel option and change the free surface level to 5 m, which is the level of the crest (as shown in Figure 75). After that, if we go back to the Momentum tab we can see that there is no pressure specification option anymore. This happens because the Open Channel option makes so that Fluent calculates the pressure on the boundary based on the water head. We don't have to change anything on the Momentum tab, so we just click on OK.

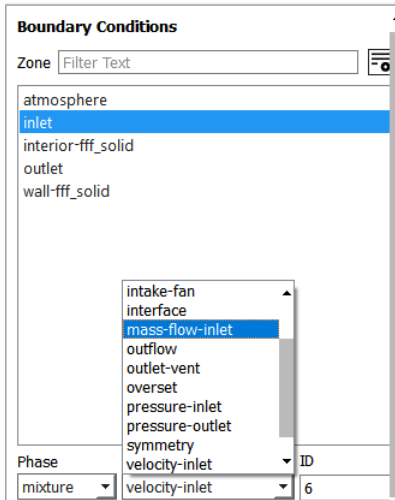


Figure 74 –Changing inlet to mass-flow

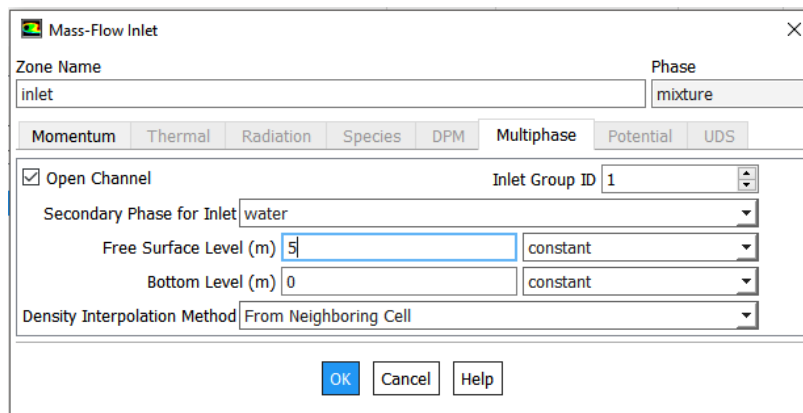


Figure 75 –Mass-Flow Inlet – Multiphase tab

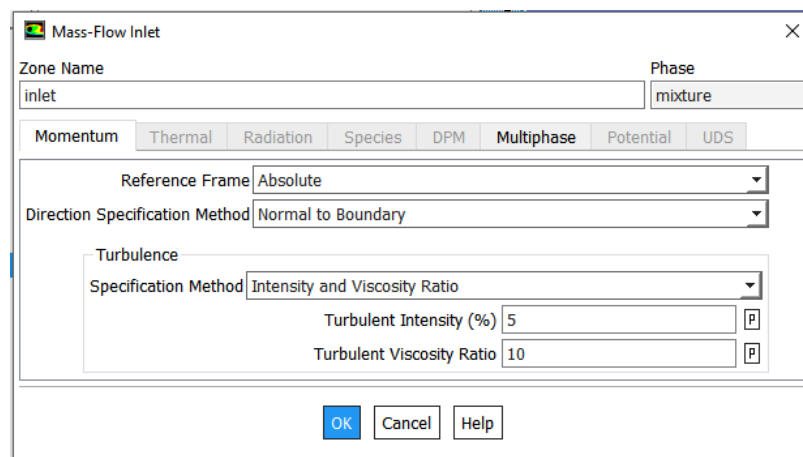


Figure 76 –Mass-Flow Inlet – Momentum tab

Still on the inlet, we have to define the mass flow rate for both phases (air and water). To do so, we double click on the options air and water on the sub menu inlet under Boundary Conditions, as shown in Figure 77. Double clicking on each of those will open their respective pop-ups where we can enter the mass flow rate come in from the inlet for each phase.

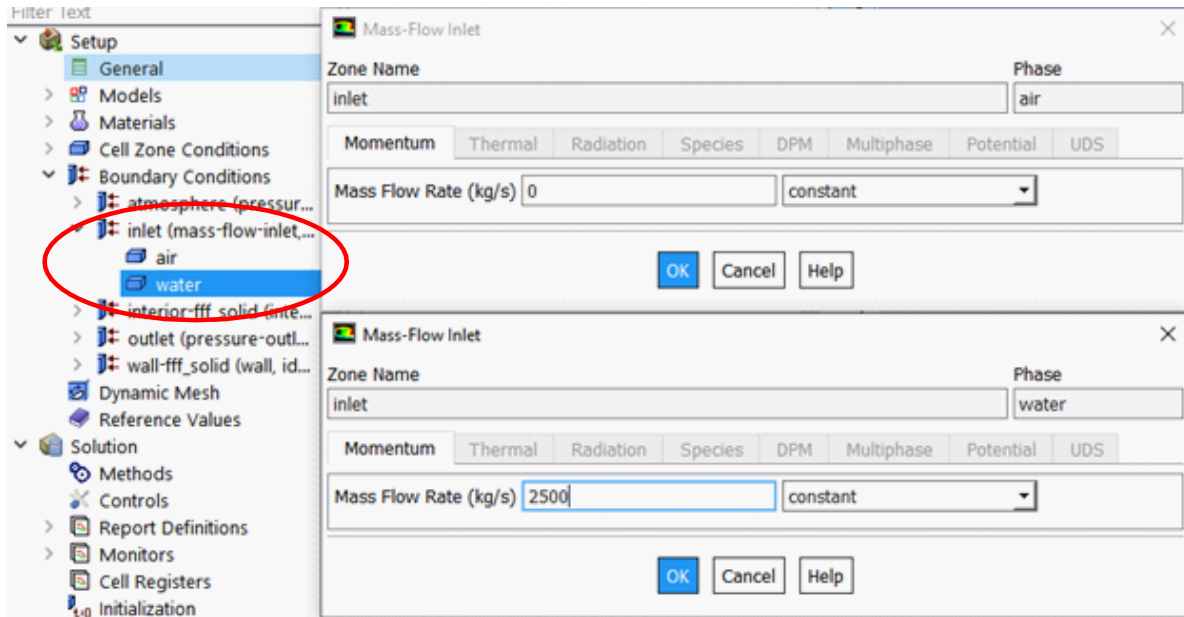


Figure 77 –Mass-Flow Inlet – Defining the mass flow rates

Next, we change the atmosphere boundary from wall to pressure-outlet, just like we did for the inlet boundary. On the multiphase tab we will enable the Open Channel option again and select Gauge Pressure on the Pressure Specification Method, as shown in Figure 78. Then, on the Momentum tab we leave the gauge pressure at 0 Pa. If we wanted atmospheric pressure we should input the atmospheric pressure value in Pascal on that field.

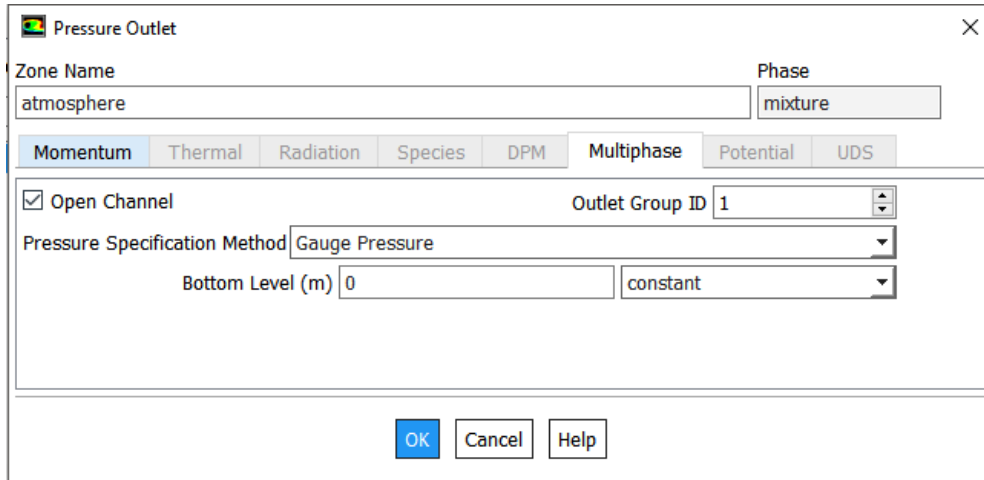


Figure 78 –Atmosphere outlet – Multiphase tab

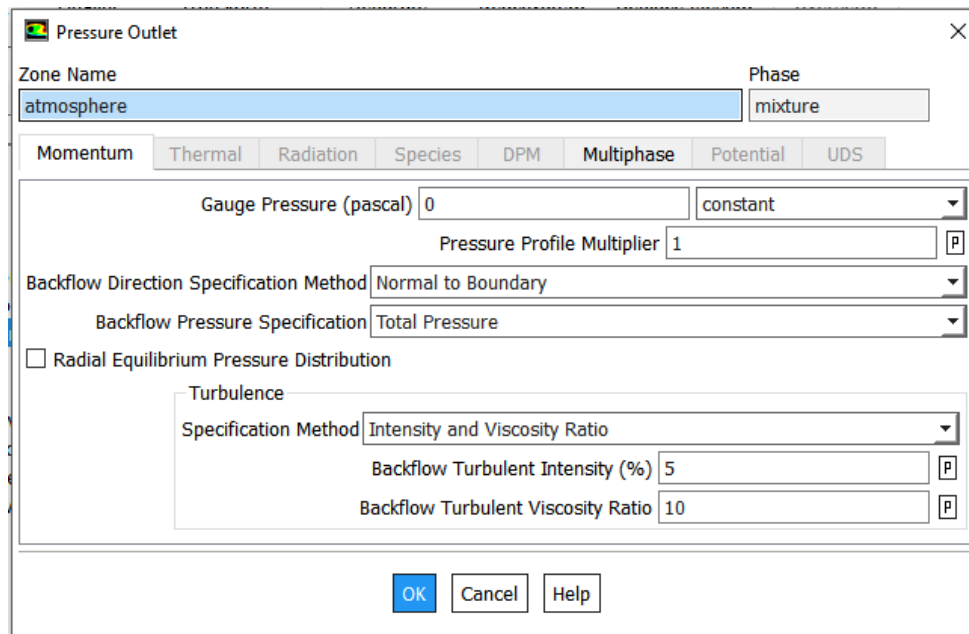


Figure 79 –Atmosphere outlet – Momentum tab

The outlet boundary should already be set to pressure-outlet so we just double click on that boundary name to edit its settings. On the multiphase tab we activate the Open Channel option again, then change the Outlet Group ID to 2 so that Fluent treats the atmosphere and the outlet boundaries differently. Then, we change the pressure specification method to From Neighboring Cell so that Fluent calculates the pressure on the boundary based on the pressure on the cells neighboring the boundary. Again, the momentum tab can be left with the default configurations.

The wall boundaries are set to be stationary no-slip walls by default, which is the configuration that we need, so we don't change anything. The interior boundary also requires no settings. Also, on the inlet, outlet and atmosphere boundaries, the turbulence intensity can be changed according to the problem.

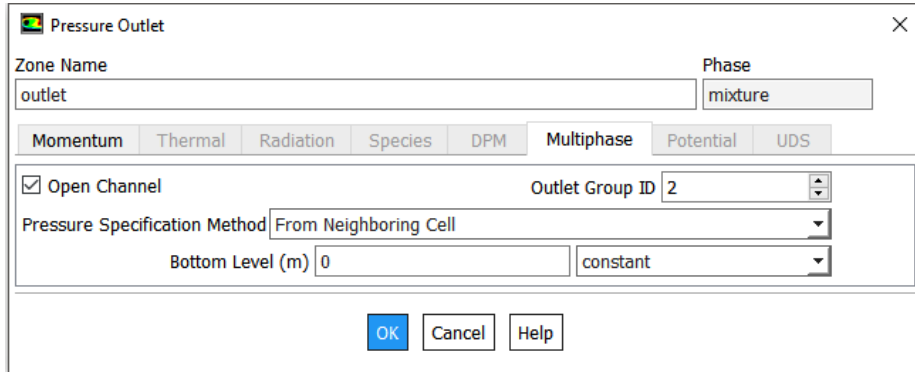


Figure 80 –Outlet – Multiphase tab

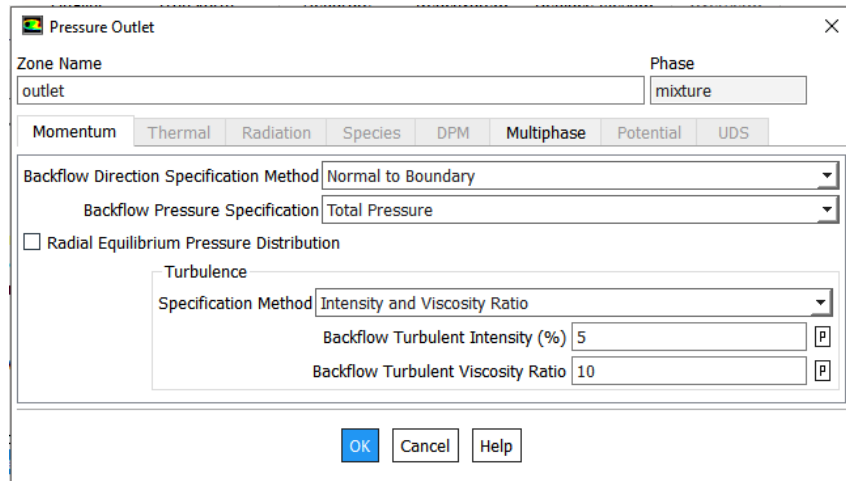


Figure 81 –Outlet – Momentum tab

With all boundary conditions set, we can select the solution methods that will be used by the solver. The selection of the appropriate method varies from case to case, but for traditional volume of fluid cases the methods shown in Figure 82 tend to work well.

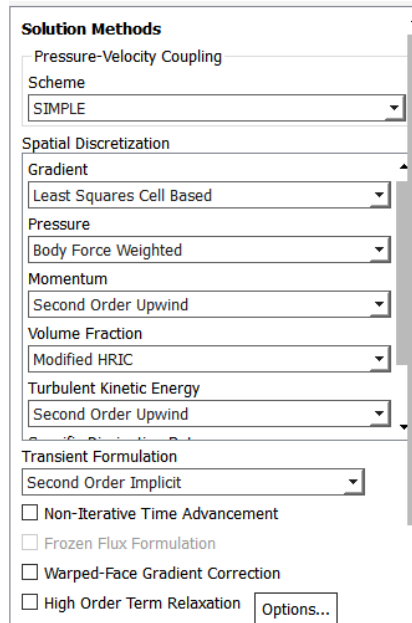


Figure 82 –Solution Methods

Next we have to initialize the solution. For that, we use the Hybrid Initialization method with the Open Channel Initialization option. We set Compute from to inlet and Open Channel Initialization Method to Flat than click on Initialize, as seen on Figure 83. This will initialize the solution with a flat surface of water. To visualize this we can go to the Results menu > Graphics and double click on Contours. This will open a pop-up to create a new contour plot. Then we can select Phases, Volume Fraction and water, as seen on Figure 84 to create and display the volume fraction plot.

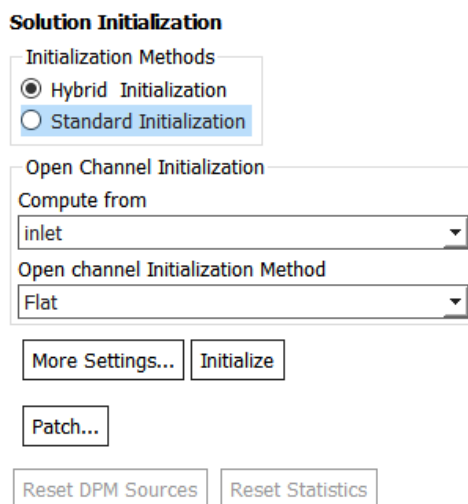


Figure 83 –Initialization menu

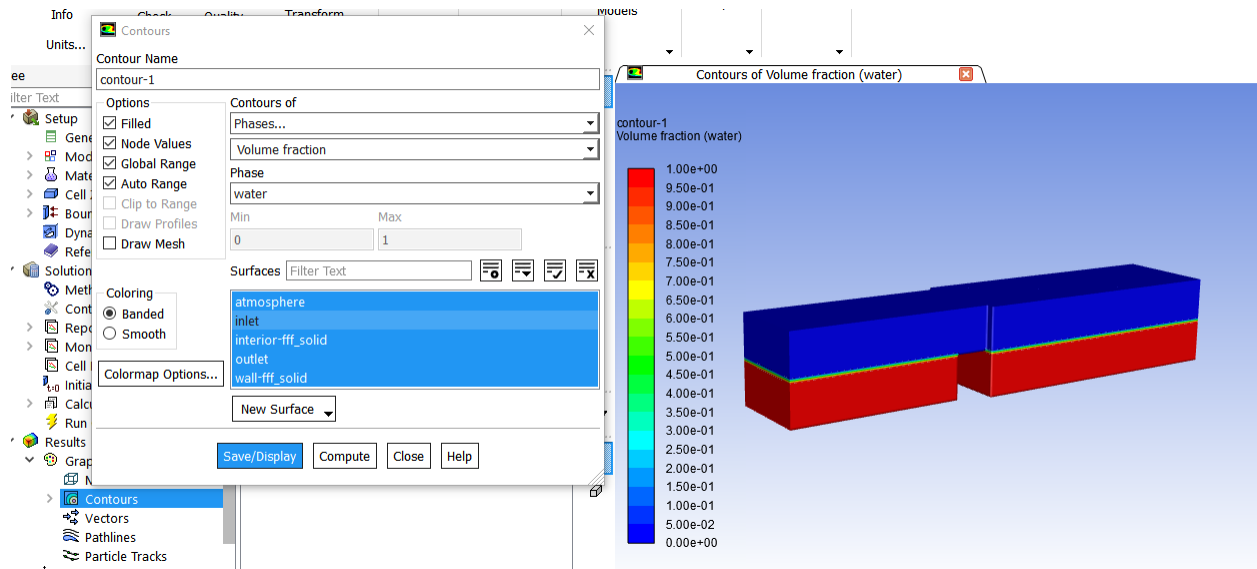


Figure 84 –Phase fraction contour plot

However, the flat initialization added water to both sides of the dam and we want it to have water only on the upstream side. That means that we need to patch the downstream side to set the volume fraction on that side to be just air. To do so, we go to the menus on the upper bar of the Fluent window and select Adapt > Mark/Adapt Cells > Region. A new window will show up where you can input the corners of a rectangular region to select all the cells that you want to mark. To select all cells on the downstream side we input the values shown on Figure 86 and click on Mark.

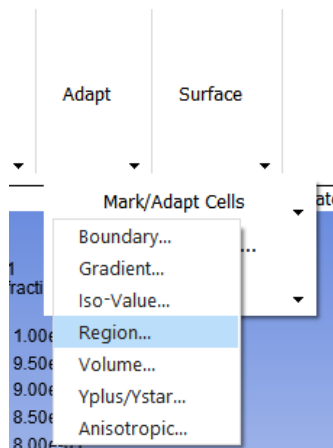


Figure 85 –Region adaptation option

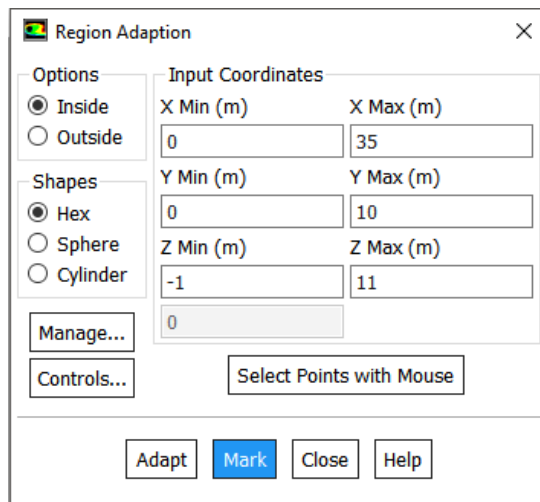


Figure 86 –Region adaptation window

After doing that we go back to the Initialization menu and click on Patch. A window like the one on Figure 87 will show up. There we have to select water to the Phase, Volume Fraction in Variable and the region hexaedron-r0, which is the region we just marked. The value field is set to 0 and then we click on Patch. This will make so that the volume fraction of water in all the cells marked on that region will be set to zero. We can verify that it worked by displaying the volume fraction plot again, as shown on Figure 88. To do so we can just right click on the contour plot we created in the graphics menu and select display.

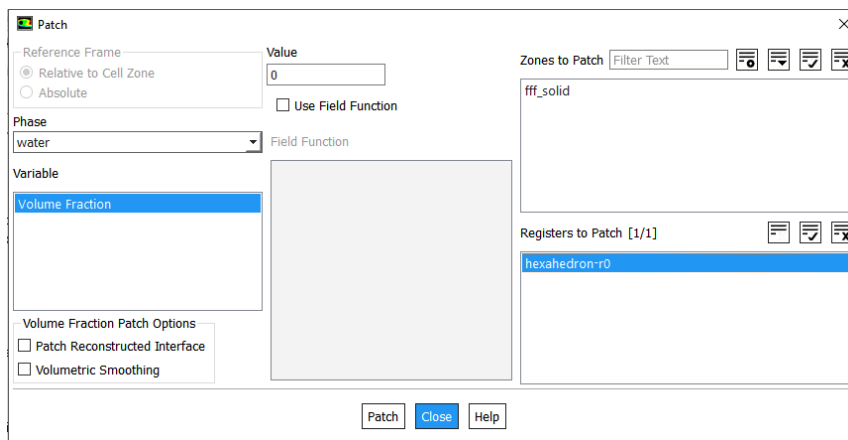


Figure 87 –Patch window

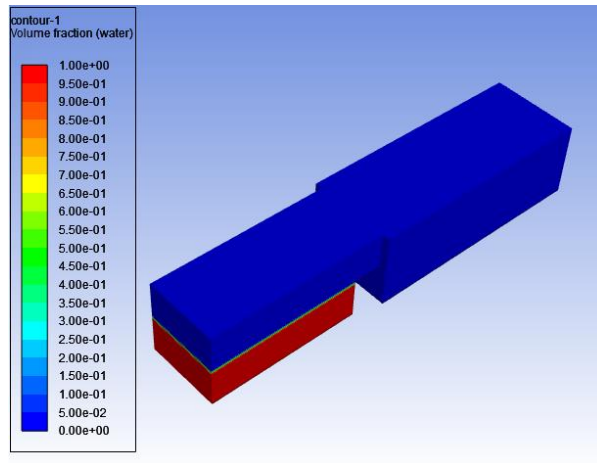


Figure 88 –Water volume fraction after patching

The last thing we have to do before running the problem is to go to the Run Calculation menu and set the stepping configurations. There we can set the number of time steps and time step sizes as well as the maximum number of iterations allowed per time step. It's also possible to set a variable time step by changing the Time Stepping Method to Variable. By doing this, Fluent will calculate the appropriate time step according to the flow Courant number. When all configurations are set we can just click on Run to start the simulation.

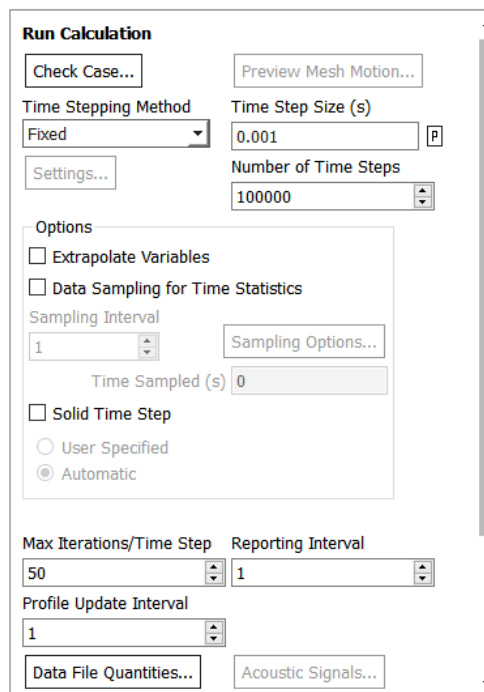


Figure 89 –Run calculation menu

However, before running the calculation there are a couple of other settings that should be changed. First, on the Calculation Activities menu there are some options to save or export the results in some different ways. The autosave option saves all the results of the simulation in a .dat file every given number of time steps. This option is very important because it allows the user to reload the simulation from a saved time step if any sort of problem happens during the simulation time. It also allows the user to load multiple time steps into the post processing software CFD-Post and analyze the results on different time steps or create animations. Another way to create animations is the Solution Animation option, which creates and displays any set plot during the simulation every given number of time steps. This can be used to monitor the solution and make sure that the volume fractions are behaving as expected, for example. However, the disadvantage of enabling these options is that they will add a significant computational time to the problem since the software has to stop the solution to save the results and create the animations, resuming the solution after those tasks are done.

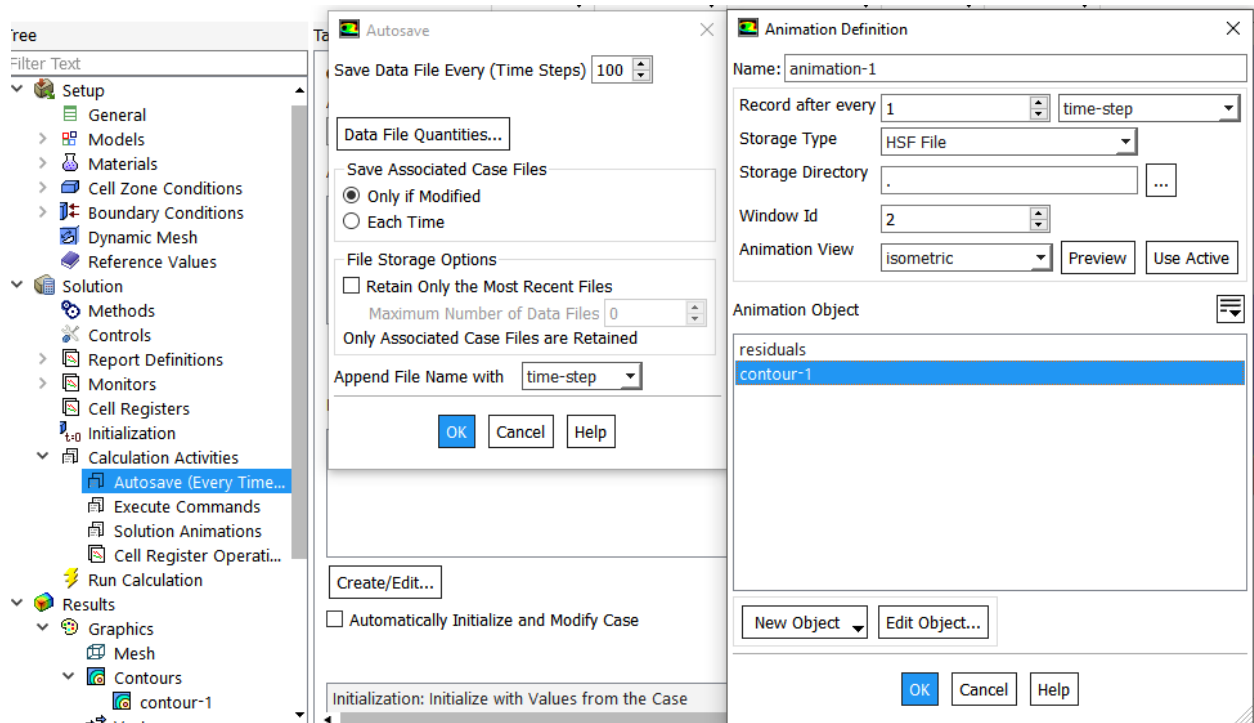


Figure 90 –Calculation activities

On the Monitors > Residual menu we can set the convergence criteria for all the equations that are solved on runtime. Figure 91 shows the window where we can set the criteria for those equations. Setting a smaller number means that the residue will be smaller and the precision of the response higher. Among other settings, there we can also enable or disable the options to print to console and plot the residues. If you are confident that the solution will not diverge and/or you are using a different way to monitor the solution, disabling those options is recommended as it can save a significant amount of computational time.

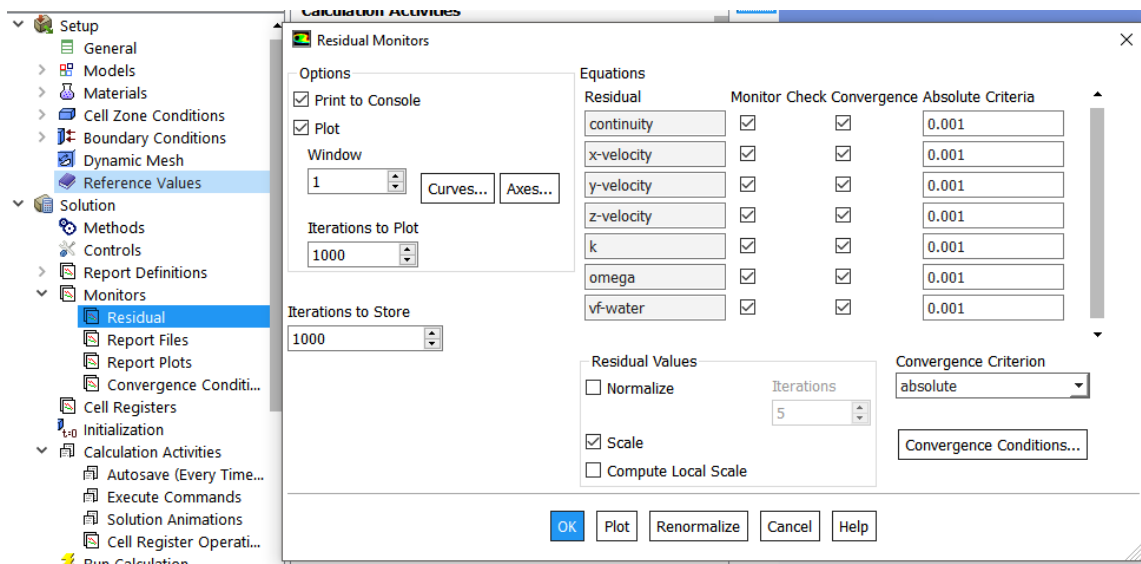


Figure 91 –Residual monitors window

Finally, another good way to monitor the convergence of an open channel flow problem is to check if the mass flow of water coming from the inlet is the same that is arriving at the outlet. To do that, we can right click on Report Definitions and go to New > Flux Report > Mass Flow Rate, as shown on Figure 92. This will open a window like the one on Figure 93. There we can set the name of the report, select the phase that will be monitored and choose which boundaries are going to be monitored. If we select just the inlet or just the outlet it will report the exact mass that is going through the boundary. Positive values means that mass is entering the domain and negative values means that it is leaving the domain. If we select both the inlet and the outlet it will sum the two values and report the difference between what it is entering from the inlet and what is leaving from

the outlet. Ideally that difference should be zero when the flow reaches steady state. We can also enable the options to create a plot that will be plotted during runtime and to save a text file with all the results of the mass flow rate per time step.

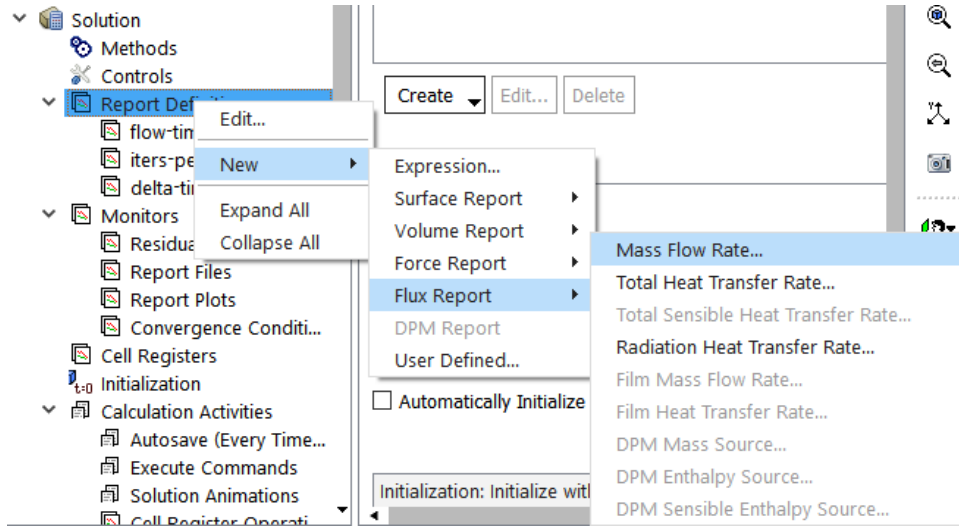


Figure 92 –Setting flow report

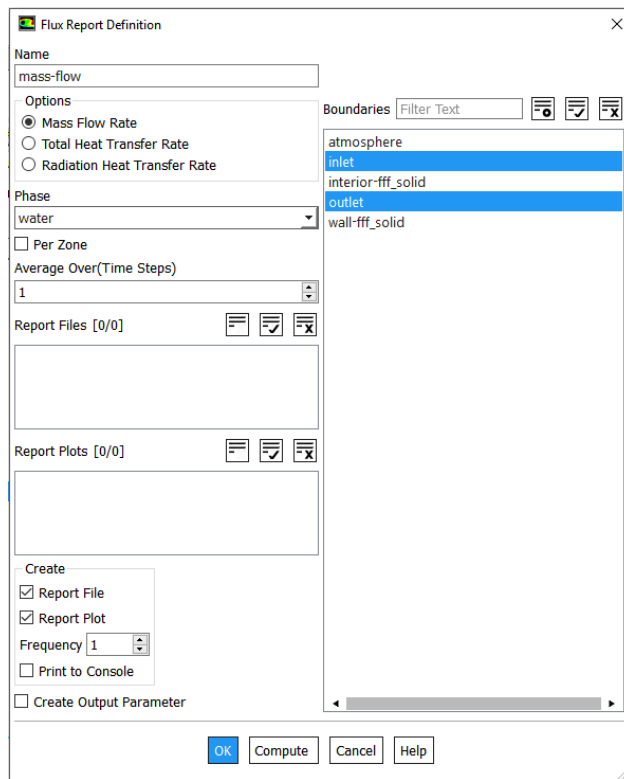


Figure 93 –Flux report definition window

Appendix B - Mesh Adaptation On Fluent

One of the tools present in Fluent that can help improve mesh related problems is the Mesh Adaptation tool. On the menu Adapt > Mark/Adapt Cells, Fluent presents many ways to mark cells for adaptation such as marking regions, boundaries, gradients, iso-values and more. For this case we used the iso-value option to select and mark for adaptation all cells that contain a water volume fraction between 0.01 and 0.99, as shown on the figure below.

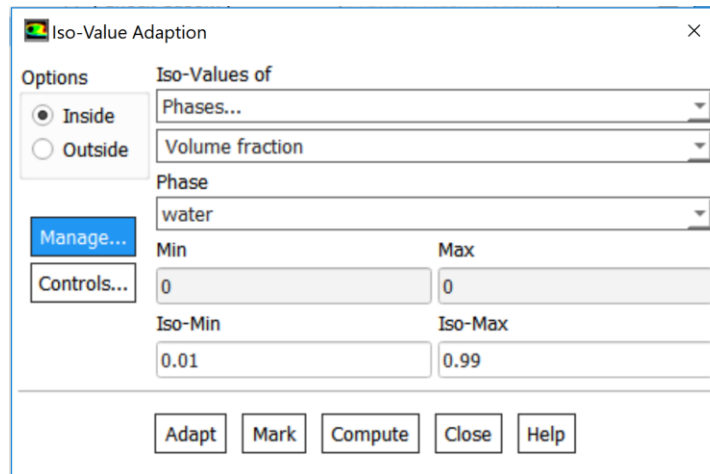


Figure 94 –Iso-Value adaptation window

We marked those cells and by clicking on Manage... another pop-up shows up that allows to display the cells that were marked before confirming the adaptation as shown on the figure below. After confirming the adaptation, Fluent will refine each marked cell by one level. That means that a square cell will be divided in four squares of the same size.

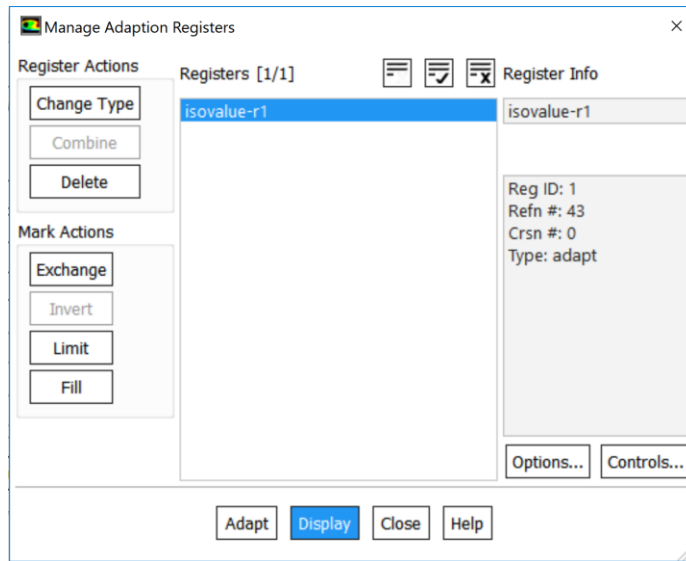


Figure 95 –Manage adaptation Registers window

To test the adaptation process, we used the coarsest mesh again, ran a simulation once, marked the cells with volume fraction between 0.01 and 0.99, adapted those cells and repeated the process 5 times. At each adaptation iteration, the volume fraction was clearly being more well defined than in the previous iteration. The following figures show (from left to right) the mesh, volume fractions contour plot and marked cells for adaptation in each of the 5 iterations.

Appendix C – Computer Specifications

The flow around a square cylinder simulations were performed on a notebook featuring a dual core Intel i5-7200U CPU, a NVIDIA GeForce 920MX GPU and 8 GB of RAM. All the other CFD simulations were performed on a mobile workstation featuring a 6-core Intel i7-8850H CPU, an NVIDIA Quadro P2000 GPU and 32 GB of RAM